MICROCOPY RESOLUTION TEST CHART

NATIONAL BUREAU OF STANDARDS-1963-A

RED (12)

A136321

UNIVERSITY COLLEGE LONDON
DEPARTMENT OF
ELECTRONIC AND ELECTRICAL ENGINEERING

REFLECTION ACOUSTIC MICROSCOPY

FOR MICRO—NDE

February, 1983

Mehrdad Nikoonahad

83 12 23 030

REFLECTION ACOUSTIC MICROSCOPY

FOR MICRO-NDE

February, 1983

Mehrdad Nikoonahad

AD

REFLECTION ACOUSTIC MICROSCOPY FOR MICRO—NDE

Final Technical Report

by

Mehrdad Nikoonahad

February, 1983

United States Army

EUROPEAN RESEARCH OFFICE OF THE U.S. ARMY

London   England

CONTRACT NUMBER ....DAERO-79-G-0011...

University College London

Approved for Public Release; distribution unlimited

3

R&D 2618-MS

REPORT DOCUMENTATION PAGE		READ INSTRUCTIONS BEFORE COMPLETING FORM
1. REPORT NUMBER	2. GOVT ACCESSION NO.	3. RECIPIENT'S CATALOG NUMBER
4. TITLE (and Subtitle) Reflection Acoustic Microscopy for Micro-NDE		5. TYPE OF REPORT & PERIOD COVERED Final Technical Report Jan 79 - Mar 82
		6. PERFORMING ORG. REPORT NUMBER
7. AUTHOR(s) Mehrdad Nikoonahad		8. CONTRACT OR GRANT NUMBER(s) DAERO-79-G-0011
9. PERFORMING ORGANIZATION NAME AND ADDRESS University College London Dept. of Electronic & Electrical Engineering Torrington Place, London WC1E		10. PROGRAM ELEMENT, PROJECT, TASK AREA & WORK UNIT NUMBERS 6.11.02A 1T16 1102BH57-04
11. CONTROLLING OFFICE NAME AND ADDRESS USARDSG-UK Box 65, FPO New York 09510		12. REPORT DATE February 1983
		13. NUMBER OF PAGES 160
14. MONITORING AGENCY NAME & ADDRESS(If different from Controlling Office)		15. SECURITY CLASS. (of this report) Unclassified
		15a. DECLASSIFICATION/DOWNGRADING SCHEDULE

16. DISTRIBUTION STATEMENT (of this Report)

Approved for public release; distribution unlimited

17. DISTRIBUTION STATEMENT (of the abstract entered in Block 20, if different from Report)

18. SUPPLEMENTARY NOTES

19. KEY WORDS (Continue on reverse side if necessary and identify by block number)
Nondestructive Evaluation
Acoustic Microscopy
Subsurface Imaging
Diffraction in Lossy Media
Pulse Compression Acoustic Microscopy

20. ABSTRACT (Continue on reverse side if necessary and identify by block number)

The reflection acoustic microscope has evolved to a stage where it can be regarded as a powerful laboratory tool for an important class of problems in non destructive examination. The report is concerned with an extension of the capability of the acoustic microscope for such applications. Acoustic microscopy involves imaging in highly attenuating media. There has for long been a controversy on whether the losses enhance or degrade the resolution of the microscope. The author has developed a novel analytical technique - an

DD FORM 1473 EDITION OF 1 NOV 65 IS OBSOLETE
1 JAN 73
S/N 0102-LF-014-6601

4

extension of Fourier optics - for analysing this problem. Results obtained show that with losses: (i) The resolution deteriorates; (ii) The sidelobe levels at the focal plane are reduced and (iii) The depth of focus of the lens is reduced.

A reflection microscope working at 1 GHz has been constructed which has a number of novel features. Using this and other microscopes, working frequencies below 100 MHz, a range of NDE problems has been examined. A design procedure for reduced aperture lenses used for subsurface imaging is presented and it is shown that with such lenses it is possible to obtain good focussing performance over a wide depth range - typically few millimeters at 50 MHz.

A major problem in subsurface imaging derives from the large reflection obtained from the surface, and the small amount of energy which is available for imaging the "object". Both these difficulties can be greatly alleviated in a new system, based on the use of broadband chirped ultrasonic pulses. Large improvements in subsurface imaging using this system have been demonstrated.

The new techniques have been applied to a range of problems. Amongst these has been the investigation of metal: metal diffusion bonds, which have been visualised for the first time.

TABLE OF CONTENTS

CHAPTER 4

SUBSURFACE NDE WITH REDUCED APERTURE LENSES

LIST OF FIGURES

13.

14.

15.

LIST OF TABLES

CHAPTER 1

INTRODUCTION

Optical microscopy is concerned with the interaction of light waves
with an object. The contrast in an optical micrograph, therefore,
reveals the variation of the optical properties of the specimen;
that is, the spatial variation of its refractive index and optical
absorption. It is clear that, in utilising a form of radiation
fundamentally unlike that of light, one will probe different aspects
of an object. Electron beams, X-rays, thermal waves and ultrasonic
waves all reveal aspects of an object that differ simply because the
nature of the interaction is characteristic of that radiation. Electron
microscopy has already been with us for half a century; X-ray and
thermal wave microscopy have recently become a reality. The transform-
ation of one form of energy into another, effected by the object, can
also be utilised and, thereby, new forms of imaging can be realised,
such as photo-acoustic, photothermal and electron-acoustic microscopy,
(Ash, 1980).

Many forms of acoustic microscopic imaging have been explored during
the last forty years. But, the major advance - the main theme of this
thesis - was the invention of the scanning acoustic microscope by
Professor Calvin Quate and his, then, student Ross Lemons of Stanford
University, (Lemons and Quate, 1974a). A schematic diagram of a
scanning acoustic microscope (SAM), operating in reflection mode is
illustrated in Figure 1.1.

18.

MECHANICAL
XY-SCAN

OBJECT

TRANSMITTER

LENS

RECEIVER

SCAN
GENERATOR

DISPLAY
SYSTEM
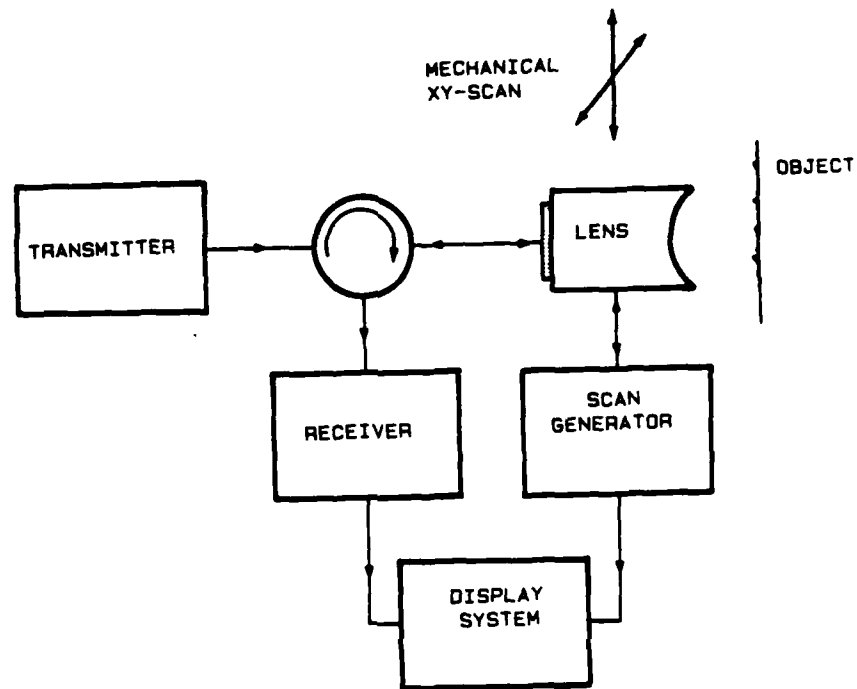
Figure 1.1:   A reflection SAM - the basic system.

In this system, the object is immersed in a liquid, (such as water),

and placed at the focal plane of the acoustic lens. A piezoelectric

transducer converts the transmitted RF electromagnetic pulses to

acoustic pulses which are brought to a focus at the focal plane of the

lens. Pulses reflected from the object are modulated in phase and

amplitude. The lens collects these echoes and the transducer converts

them back to electrical pulses which, after detection, provide a

video signal. This signal is the input to the display system and is

19.

used to intensity modulate an electron beam on a display monitor.
The lens is subsequently scanned over the entire field of view, in
a raster manner, in synchronism with the electron beam on the display.
The image is thus built up point by point.

The acoustic lens consists of a spherical cavity, ground and polished
in a solid buffer rod, as shown in Figure 1.2.

The essence of such a lens relies on a single, highly refractive
surface, (Lemons and Quate, 1974a). The high velocity ratio between
the solid and the liquid causes the rays to converge to a focus very
near to the centre of the spherical cavity; spherical aberration is
thereby minimised - leading to a nearly diffraction limited focus.

The lateral resolution of the microscope is set by the diameter of the
spot size at focus, which from the Abbe theory is approximately given
by $v/(2f \sin \theta)$, where v is the sound velocity in the liquid coupler,
f is the operating frequency and θ is the half angular aperture. It is
seen that the resolution increases with the frequency. On the other
hand, at high frequencies, the losses, for all room temperature liquids,
are high; for classical liquids, the attenuation coefficient increases
with f^2. Therefore, whilst increasing the frequency enhances the
resolution, owing to high losses, the signal to noise of the system is
reduced - leading to a reduction in the detection sensitivity. Since
the spot diameter is directly proportional to the sound velocity in the
couplant, one seeks a low-velocity, low-loss liquid, for use near
room temperature. It transpires that water is one of the best, (Attal
and Quate, 1976).

20.
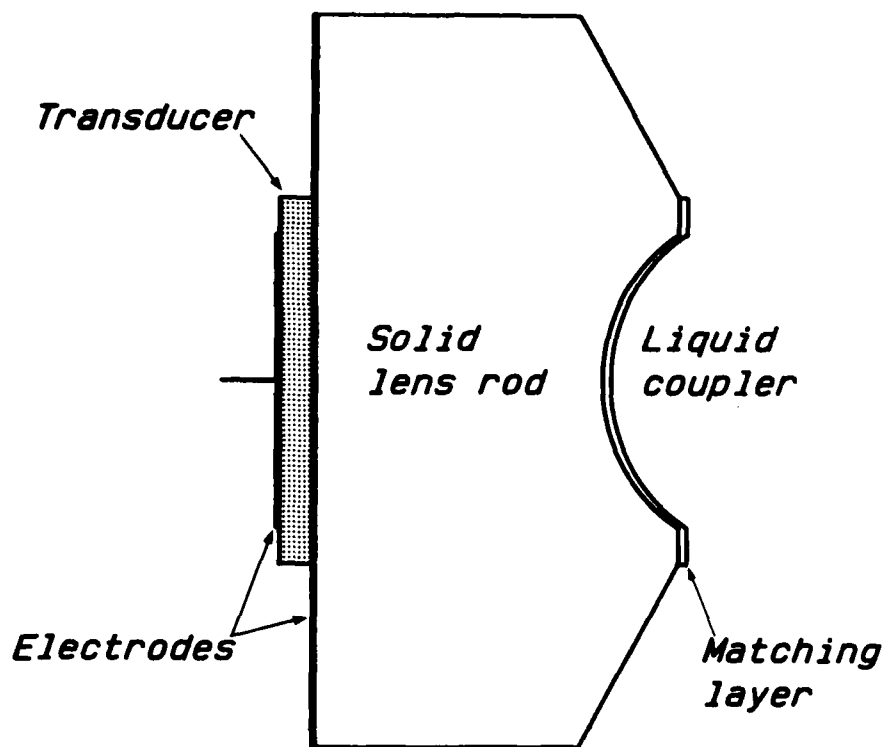
Figure 1.2:   The schematic diagram of a typical acoustic lens.

In most fluids, sound waves travel slower by a factor of 10^5 than light waves. Therefore, working at 1 GHz, and using water as the coupling medium, the resolution is of the order of 1μm. At an operating frequency of 3 GHz, a resolution better than 0.5μm has been achieved, (Jipson and Quate, 1978).

Another form of acoustic microscopy which, in fact, predates the Quate microscope, is based on a somewhat different principle. It is the scanning laser acoustic microscope (SLAM), in which an unfocussed beam of acoustic energy is directed at the body of the sample under examination, Figure 1.3.

21.
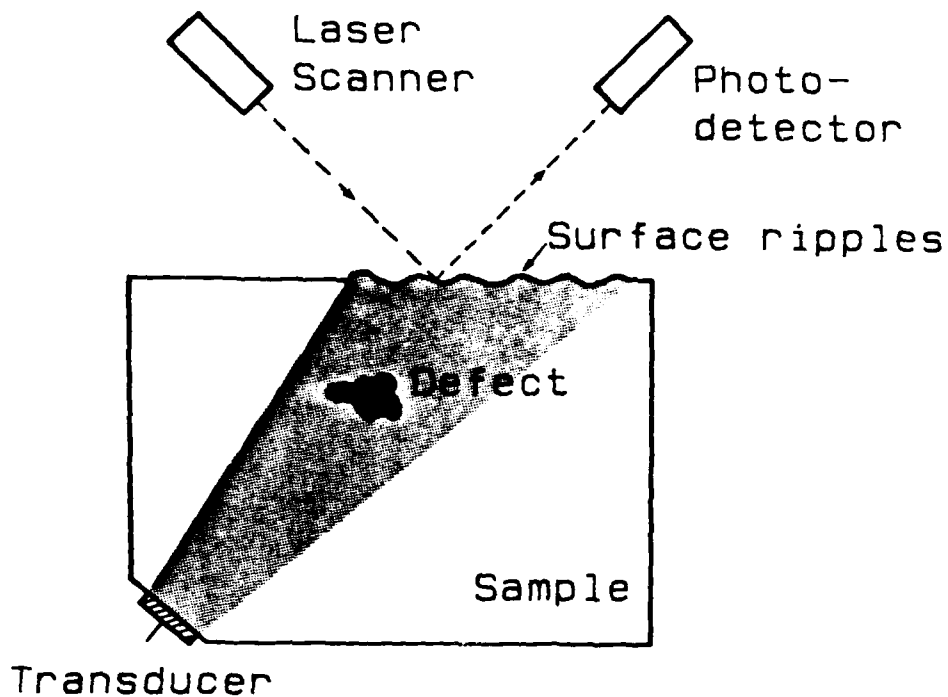
Figure 1.3:   The basic operation of the SLAM.

Any acoustic inhomogeneity in the path of the acoustic beam causes the

scattering and interference of the acoustic radiation. This manifests

itself as ripples on the surface of the sample and is recorded by the

use of a rapidly scanned focussed laser beam, (Kessler and Yuhas, 1978).

The final image produced by a SLAM is essentially an ultrasonic shadow-

graph of the subject. It has significant merits with regard to certain

problems in material inspection, (Madeyski and Kessler, 1976);

Kupperman et al, 1980), notably the ability to image objects very fast.

In a SAM, the contrast arises from the interaction of the sound beam
with the elastic properties of the material; variations in stiffness,
density and viscosity contribute to image formation. These elastic
characteristics of solids are often of key significance - the primary
reason for the utilisation of the acoustic microscope in material
testing. In most cases, specimens need very little, if any, pre-
paration. In a reflection SAM, only a single lens is used, serving
as both transmitter and receiver. Reflection microscopes are, there-
fore, particularly attractive for NDE because, in principle, there is
no restriction on the thickness of the sample. In most cases, this
allows the examination of complete, even massive, samples. Although
to date the use of acoustic microscopy has been largely confined to
the laboratory, there are now good prospects for applications in
production inspection.

Applications of reflection acoustic microscopy range from imaging voids,
inclusions and microcracks at a substantial depth below the surface of
optically opaque solids, to the NDE of diffusion bonds, solder joints
and semiconductor:metal bonds. Surface characterisations of solids,
viewing microelectronic components and the detection of surface, or
near surface, defects are amongst the applications of high frequency
reflection microscopy. A reflection system can also play the role of
a high resolution probe for measuring the acoustic surface parameters
on a *quantitative* basis.

23.

In a number of NDE applications, transmission acoustic microscopy
has also provided fruitful results, (Tsai et al, 1977; Tsai et al,
1979; Sinclair and Ash, 1980). The techniques of acoustic micro-
scopy have also been exploited, with great success, for the character-
isation of biological samples and, particularly, tissue, (Bennett and
Ash, 1981; Bennett et al, 1982; Sinclair and Smith, 1982).

This thesis is concerned with the Quate-type reflection scanning
acoustic microscopy and its particular applications in NDE. A more
detailed review of this subject can be found elsewhere, (Nikoonahad,
1983). In this Chapter, some of the principle applications of a
reflection SAM are outlined.

1.1. Surface Imaging.

Microelectronic components, metal composites, corrosion and fatigue
cracks are worthy of scrutiny by acoustic microscopy, which offers new
insights. The contrast is often greater than that for corresponding
optical micrographs. Recently, there has also been interest in imaging
ceramics and solid dielectrics using the acoustic microscope. The
reflection microscope has also been used successfully for imaging poly-
mer and paper materials.

In surface metallurgy, characterisation of grain structure in poly-
crystalline metals, locating and imaging surface and near surface defects,
(Quate, 1980; Briggs et al, 1982), reflection microscopy has proved
fruitful. The reflection microscope facilitates the study of the adhesion

of metal thin films - a disbonded region (a small air gap) - leads to 100% reflection of the acoustic radiation. On a high resolution basis, adhesion of metallic thin films to nonmetallic substrates has been reported, (Bray et al, 1980). One specific application of this is in the context of chromium masks.

The first experiment, for imaging an integrated circuit, was carried out at 600 MHz, (Lemons and Quate, 1974b). A recent article by Bennett (1982) reviews the many existing applications of the acoustic microscope for integrated circuit technology. In this field, the main applications can be divided into two different categories: (i) device inspection and (ii) material characterisation. Delamination of thin passivating films is of interest; acoustic microscopy has provided results that could not have been obtained with the optical or the electron microscope, (Hollis and Hammer, 1980). In silicon on sapphire (SOS) devices, the adhesion of the silicon layer to the sapphire substrate plays an important role in the electrical properties of the device. Acoustic microscopy has been used to characterise such devices, (Miller, 1982).

Reflection acoustic microscopy has recently been applied to the study of polymers. Acoustic micrographs of polypropylene spherulites, grown between glass slides, show irregular growth of radial fibrils, (Wilson and Tucker, 1979). A filled polymer is a typical structural material used for a number of industrial applications, and promising results have recently been obtained from silica filled polypropylene, (Johnson, 1982).

25.

1.2.   Material Characterisation:V(z).

Reflection acoustic microscopy also provides the means for quantitative
surface characterisation. It was first experimentally observed that the
contrast of a micrograph periodically changed with the axial distance
between the lens and the object   (Wilson et al, 1977; Atalar
et al, 1977;   Weglein and Wilson, 1978). Since then, this technique
has come to be known as acoustic material signature (AMS). It is also
known as the V(z) technique, representing the variation of the output
voltage of the transducer, V, with distance, z. The theory of V(z)
curves was first devised by H.K. Wickramasinghe, (1978). A paraxial
approximation which gives a helpful insight has been published by
Atalar (1978). It is also possible to apply simple ray theories,
(Parman and Bertoni, 1979; Quate, 1980), which show that the effect
is essentially due to the generation of Rayleigh waves.

Here, the detailed mathematical derivation of V(z) curves is not the
concern, but, following a brief description of the basic physics which
gives rise to this effect, the applications will be examined. Also,
it should be added, that although V(z) is the heart of material chara-
cterisation with a standard reflection SAM, other techniques of
acoustic microscopy, based on principles radically different from V(z),
have also led to promising results, (Smith et al, 1980; Smith et al,
1981).

The angular spectrum emitted from a typical acoustic lens extends to $\pm 60^{\circ}$ from the axis of the lens. The rays incident on the surface at the Rayleigh angle produce a surface acoustic wave travelling on the surface of the specimen. Because the surface is immersed in a liquid - usually water - having a low propagation velocity, the Rayleigh wave continuously leaks back into the water, being collected by the lens as shown in Figure 1.4. It is clear that the Rayleigh path on the surface is a function of lens:object distance. By changing this distance, the total path length, and therefore the phase of the Rayleigh wave, also changes. On the other hand, the only phase shift for the on-axis component is due to different paths in the liquid. When these two components reach the lens they interfere, giving rise to a series of maxima and minima, in the output voltage of the transducer.

The Rayleigh phase shift and, therefore, the periodicity of these maxima and minima is a function of the Rayleigh velocity, so that the $V(z)$ curve is a characteristic of the material. In order to measure the $V(z)$ curve, the scans are stopped and the output voltage of the microscope is read as a function of the defocussing distance. Since the first experimental observations and the subsequent formulation, a number of applications have emerged.

The simplest application of the AMS technique is the calculation of the Rayleigh velocity by measuring the periodicity of the curves.

27.
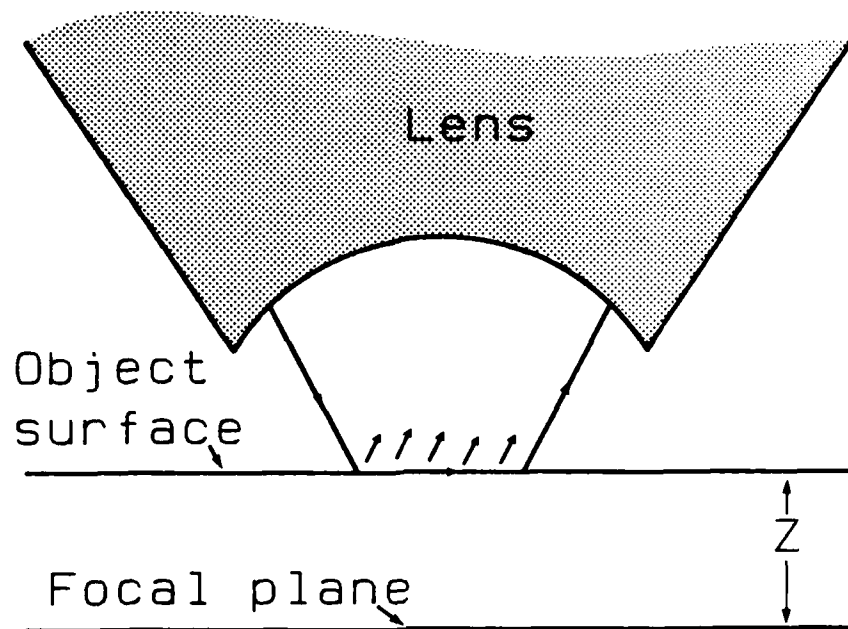
Figure 1.4:   Generation and leakage of surface waves.

One of the NDE applications of this technique is the study of the structural rigidity of metals and alloys, (Weglein, 1980a). For a thin film deposited on a substrate, the surface wave velocity is a function of the film thickness. The AMS technique has been used to record the V(z) curves for gold films on silicon, and the thickness of the films has been successfully measured in this way, (Weglein, 1980b). The technique is of considerable value for two basic reasons: Firstly, the measurement is carried out with high lateral resolution - the film thickness variation can be measured point by point. Secondly, generating the surface waves by the acoustic lens does not require the

28.

specimen to be piezoelectric. This technique is of value for the examination of thin films used in microelectronics, as well as for thicker, plated layers widely used for protection. Nondestructive measurement of gold film on industrial diamonds has been carried out using this technique, (Weglein, 1982b).

Anistropy gives rise to a different surface wave velocity which depends on the lateral directions. A spherical lens launches surface waves radially in all directions; the surface wave velocity which gives rise to the V(z) dips is, therefore, velocity averaged over all directions. However, one can devise a cylindrical lens which generates the surface waves in one direction only, (Kushibiki et al, 1981a). With this scheme, V(z) curves at different angles give different periodicities and, therefore, the complete velocity surface can be determined. It is important to appreciate, however, that the price paid for the use of this technique is a reduction in resolution.

The presence of porosity and grain structure in a material causes scattering and the attenuation of an ultrasonic wave in that material. By measuring the attenuation coefficient, one can work back to derive some information on, for example, the density or grain size in a given material, (Tittmann and Ahlberg, 1982). Recently, there has been great interest in using the V(z) techniques for measuring the *surface* attenuation coefficient, (Weglein, 1982a; Yamanaka, 1982; Smith and Wickramasinghe, 1982). The basic philosophy is that, as the Rayleigh path length is increased, the surface attenuation increases correspond-

ingly, with an attendant reduction in the peak to peak amplitude in the V(z) curves, which is, therefore, a measure of the attenuation.

1.3.   Subsurface NDE.

Reflection acoustic microscopy has been applied successfully to imaging microstructures below the surface of optically opaque solids. The reason for this successful application of the technique is simply that ultrasonic radiation in the MHz frequency range, and even in the GHz frequency range, can propagate in solids without any substantial attenuation. The frequency of operation at the higher end is limited by the attenuation characteristics of the material of course. When the wavelength becomes comparable to the grain size, the grain boundary scattering loss is the dominant factor in the attenuation coefficient.

When it is attempted to form an ultrasonic focus below the surface of a solid, several problems are immediately encountered: Firstly, the high velocity discontinuity between the couplant and the object causes a large spherical abberation, thereby degrading the formation of the subsurface focus. Secondly, high reflection loss at this interface tends to mask the relatively smaller reflection from the plane of interest, which arrives only shortly after the surface echo. This makes the separation and detection of the image echo difficult.

With a water coupling medium, the two way reflection loss at the object interface can be as high as 25 dB, depending on the impedance of the object. Liquid metals have been used successfully for sub-surface imaging, (Jipson, 1979b; Attal, 1980). The relevant properties of liquid metals are compared to those of water in Table 1.1.

Liquid	Temperature (^{o}C)	Velocity (Kms^{-1})	Density (g cm^{-1})	Attenuation (at 1 GHz,dB/mm)
Mercury	23.8	1.45	13.6	50.3
Gallium	~30.0	2.87	6.1	13.7
Water	20.0	1.50	1.0	217.2

Table 1.1.   Acoustic properties of mercury, gallium and water. (Mostly after Attal and Quate, 1976)

It is seen that by employing a liquid metal couplant, the higher density results in a larger impedance. The interface impedance discontinuity is then reduced and the object becomes more "transparent". Also, from Table 1.1, it is seen that the attenuation in liquid metals is less than that in water; this feature makes the couplant path loss smaller, so that lenses with a relatively large radius can be used.

The use of liquid metals greatly reduces the interface reflection loss. However, as far as the spherical aberration is concerned,

31.

gallium performs better, but mercury, for which the velocity is very close to that of water, does not. If one is prepared to image with *shear* rather than longitudinal waves, there is one mode of liquid metal imaging where the spherical aberration can be minimised greatly. The reason is that the shear velocity in most solids is close to the longitudinal velocity in gallium. The shear waves generated at the interface (via mode conversion), can be brought to a nearly diffraction-limited focus within the solid. This technique has successfully been demonstrated at 1 GHz, (Jipson, 1979b).

1.4   Thesis Structure.

The current theory of image formation either neglects losses, or incorporates losses as a perturbation. The practical situation in acoustic microscopy is that the losses can be exceedingly large. An even more dramatic example is provided by the propagation of thermal waves in solids, where the real and imaginary parts of the propagation constant are approximately equal. It is desirable, therefore, to obtain a rigorous formulation which can give a definitive answer to such questions as, for example, the change of resolution and, in the sidelobe levels, as a function of loss - Chapter 2.

The basic concept for research has been the utilisation of reflection acoustic microscopy for different aspects of NDE. For surface and near surface examination, a reflection SAM working at 1 GHz was constructed. Chapter 3 is devoted to the design of this microscope,

32.

and includes a discussion on the RF electronics, scanning mechanics and electronics, as well as position sensing. Results obtained from the examination of a number of objects are presented in the same Chapter.

Although liquid metals have been successful for subsurface imaging, their usage is not without problems. They can readily form an amalgam with metals such as gold, tin, lead and indium, which feature in some objects of interest. Furthermore, liquid metals do not easily wet most solids. The surface of the object has to be clean and free from any electrical charges. In some cases, ion-bombardment prior to immersion has been recommended. Also, surface absorption of gases makes wetting difficult, (Attal, 1979). The standard technique for surface outgassing is baking. Ion bombardment and baking can be undesirable for some NDE applications. It must be concluded that liquid metal techniques are suitable for specific applications, rather than for NDE of a *wide range of objects*. It should be added that the mode conversion technique is restricted to a class of objects for which the shear velocity is a reasonable match to the longitudinal velocity of the liquid metal. Therefore, there are grounds for maintaining water as the couplant and correcting the interface aberration by adapting the lens geometry.

In Chapter 4, the design of reduced aperture lenses for subsurface imaging is discussed. It is shown how, by means of such lenses, one can image through a range of solids. For subsurface NDE, it is

essential to remove the surface reflection by suitable time gating.
This implies that broadband pulses must be employed, so that the
surface echo and the "object" echo do not interfere. Chapter 4
also deals with the simulation of a number of broadband transducer
structures, suitable for acoustic microscopy. Subsurface micrographs
obtained at 40 MHz are presented in this Chapter.

The closer the image plane to the surface of the object, the
narrower the width of the pulses, for time gated operation. The
amount of energy carried by a pulse is directly proportional to its
width; naturally, narrow pulses do not carry much energy. Lack of
sufficient average power in the system gives rise to a reduced
detection sensitivity which is particularly undesirable for low
contrast objects. To maintain high range resolution with high
detection sensitivity, one can resort to the use of long coded
pulses. We have constructed a pulse compression microscope working
at 60 MHz, Chapter 5, and have obtained improved subsurface micro-
graphs. A theoretical model of the pulse compression microscope
is also presented in Chapter 5. With this model, the effect of
dispersive attenuation in the liquid cell on the performance of the
pulse compression microscope has been investigated.

Chapter 6 is devoted to the imaging and characterisation of metallic
diffusion bonds with the pulse compression microscope. In Chapter 7,
conclusions of the thesis are presented, together with suggestions
for continuation of this research.

CHAPTER 2

ULTRASONIC FOCUSSING IN ABSORPTIVE FLUIDS

2.1.   Introduction.

In acoustic microscopy, one is concerned with the focussing of
ultrasound through absorptive fluid couplers. The resolution of
the microscope increases linearly with frequency; on the other
hand, for most classical fluids, the absorption coefficient is
proportional to the square of the frequency, (Kinsler and Frey, 1962).
This imposes an inherent limitation on the maximum operable frequency
in acoustic microscopy.

In this Chapter, a rigorous formulation for calculating the field
distribution at different planes in an attenuating medium is presented,
with the prime objective of studying the effect of a finite attenuation
coefficient on the focussing performance of a lens. This analysis is
based on the techniques of Fourier transform and a solution for the
elementary waves, into which the field is expanded, is obtained. The
field distribution for typical lenses, in the vicinity of the focal
plane, has been calculated, with different path losses in the propag-
ating medium.

The Fourier optics approach to the analysis of focussing and diffrac-
tion structures, leads to a complete formulation and, in addition,
provides a clear physical insight into the nature of the phenomena.

35.

It is, however, in its normal form, confined to *lossless* systems.
The reason for this restriction is simply stated: In Fourier optics
one seeks to derive *a field* distribution in a plane BB', given a
source distribution in a parallel plane AA', Figure 2.1.
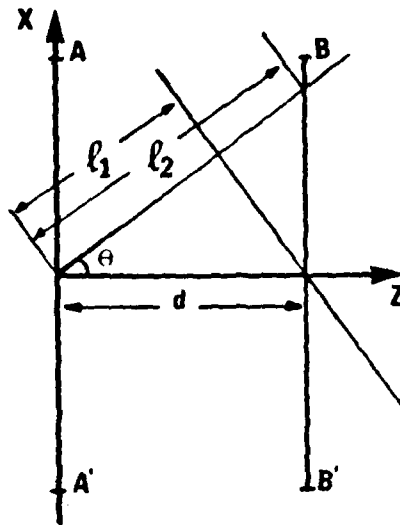
Figure 2.1:   The lengths involved in the propagation of the angular
spectrum from plane AA' to BB'.

The basic method is *to expand the* field in AA' into a set of plane
waves, recombining them at BB' after including the propagation
phase changes.   The expansion and subsequent recombination are
effected by taking the appropriate Fourier transforms.   The existence
of these transforms implies that the amplitude of the individual
constituent plane waves is constant on the planes such as AA' and BB'.
It is clear that, for plane *waves in a lossy* medium, the planes of
constant amplitude will be the equiphase planes normal to the

propagation vector. The amplitude distribution on a plane such as

AA' will vary exponentially with distance, increasing without limit

in one direction.

In most cases, this problem is not of any great importance. One can

adopt the approach so widely used in analysing losses in guided wave

structures - to solve the lossless case, and then to include losses as

a perturbation. Physical intuition would strongly suggest that,

provided the losses are not too great, and provided that the angular

spectrum of the waves is not too large, this approach will give

results which are a good approximation to the truth. In propagating

a typical plane wave, one would simply include an attenuation factor

$exp(-\alpha\ell)$, where ℓ is the appropriate propagation length from plane

AA' to BB'. However, even here there is an issue which is not readily

resolved by purely intuitive arguments: By reference to Figure 2.1,

should one choose $\ell_1 = d.\cos\theta$, or $\ell_2 = d/\cos\theta$? The former, which has

been used by Wickramasinghe (1979) would suggest that higher spatial

frequencies are relatively enhanced in propagating from AA' to BB'; the

latter, which has been used by Al ais and Hennion, (1979), would

suggest that they are preferentially attenuated. Clearly, it is an

issue which is of interest only if $exp(+\alpha\ell)$ is large, and if the range

of θ is also large. Such situations are found in ultrasonic imaging,

and particularly in high resolution acoustic microscopy, where the

attenuations involved may be over 30 dB, and the angular range in

excess of $\pm50^{\circ}$. An even more dramatic instance arises in analysis of

thermal wave imaging, where the real and imaginary components of the

propagation vector are comparable, (Rosencwaig, 1980).

The aim of this Chapter is to present an analytical approach in which the losses are taken into account *ab initio*, and which can be used to compute focussing and diffraction fields in a manner which is inherently as simple as that of classical Fourier optics. At the same time, a picture of the basic waves which take the place of plane waves in the lossless case will be developed. These waves provide a satisfactory understanding of the physical reality.

2.2.   Theoretical Formulation.

2.2.1   Basic Formulation

It will be assumed that the propagation phenomena are adequately conveyed by a scalar model, and that the ultrasonic field, U, is described by the Helmholtz equation:

$$\nabla^2 U + k^2 U = 0 \qquad\qquad (2.1)$$

It is further assumed that the loss mechanism is such that it can be represented by a complex propagation constant,

$$k \equiv \beta - j\alpha \qquad\qquad (2.2)$$

For simplicity, the analysis and subsequent computations have been restricted to the two-dimensional case with variations confined to the (x,z) plane. The extension to three dimensions is straightforward. For the two-dimensional case, Equation (2.1) can be written in the form,

38.

$$\frac{\partial^2 U}{\partial x^2} + \frac{\partial^2 U}{\partial z^2} + k^2 U = 0 \qquad (2.3)$$

The Fourier transform of $U(x,z)$ is defined by,

$$T(f,z) = \int_{-\infty}^{+\infty} U(x,z)e^{+j2\pi fx} dx \qquad (2.4)$$

where f is the real transform variable. We can Fourier transform Equation (2.3) directly,

$$\frac{\partial^2 T}{\partial z^2} + (k^2 - 4\pi^2 f^2)T = 0 \qquad (2.5)$$

which has the solution

$$T(f,z) = T(f,0)e^{-jk_z z} \qquad (2.6)$$

where $k_z = k^2 - k_x^2$
and $k_x^2 \equiv 4\pi^2 f^2$ $\qquad (2.7)$

Superficially, Equation (2.6) looks like the standard formulation in terms of a plane wave spectrum. It is, however, important to appreciate that $T(f,z)$ is not a homogeneous plane wave; it will be seen later that it is a truncated inhomogeneous plane wave, extending over a part of the (x,z) plane only.

39.

The inverse of Equation (2.4) can now be applied to the T(f,z) found
in Equation (2.6), with the final result that,

$$U(x,z) = \int_{-\infty}^{+\infty} T(f,z) e^{-j2\pi fx} df \qquad (2.8)$$

Equations (2.4) through (2.8) suffice to compute U(x,z) from U(x,0);
it is the basis of the results presented in the next section.

2.2.2. Nature of the Elementary Waves

It has been seen that the Fourier optics approach appears to remain
rigorously correct in the loss present case — but that the elementary
waves into which the field is expanded are the T(f,z), instead of
the usual plane waves. In this section, their nature will be explored,
and the ways in which they differ from plane waves will be indicated.
In the lossless case, one can resolve the wave vector k into compon-
ents,

$$\left. \begin{array}{l} k_z = k\cos\theta \\ k_x = k\cos\theta \end{array} \right\} \qquad (2.9)$$

This formulation is retained for the lossy case, but now Equation (2.9)
is regarded as a *definition* of the complex quantity θ,

$$\theta \equiv \theta' + j\theta'' \qquad (2.10)$$

From Equations (2.7), (2.9) and (2.10) can then be written

$$k_x \equiv 2\pi f = (\beta - j\alpha) \sin (\theta' + j\theta'') \qquad (2.11)$$

f has been defined as a real variable, so that the imaginary part of the right hand side of Equation (2.11) must be zero. Expanding the sine function, we find,

$$\tanh \theta'' = \frac{\alpha}{\beta} \tan \theta' \quad \text{for } |\theta'| \leq \tan^{-1}\left(\beta/\alpha\right) \qquad (2.12)$$

and $k_x = \beta \sin\theta' \cosh\theta'' + \alpha\cos\theta' \sinh\theta''$ \qquad (2.13)

Similarly, from Equation (2.9), we find,

$$k_z = \beta\cos\theta' \cosh\theta'' - \alpha\sin\theta' \sinh\theta'' \qquad (2.14)$$
$$- j(\alpha\cos\theta' \cosh\theta'' + \beta\sin\theta' \sinh\theta'')$$

From Equation (2.8) it can be seen that the elementary contribution to the spectrum is dU(x,z)

$$dU(x,z) = T(f,0) e^{-jk_x x} e^{-jk_z z} \qquad (2.15)$$

The equi.-   ,e front of this wave can be found by putting,

$$k_x x + \text{Re}(k_z z) = 0 \qquad (2.16)$$

It is clear therefore that the elementary waves retain planar wave fronts. Using Equation (2.12), it is readily shown that this implies

$$- \left(\frac{x}{z}\right) = \frac{\beta^2 \cot\theta' - \alpha^2 \tan\theta'}{(\alpha^2 + \beta^2)} \equiv \cot\phi \qquad (2.17)$$

where ϕ is the angle between the normal to the wave front and the z axis - i.e. the equivalent of θ in Figure 2.1. It is, therefore, illuminating to write Equation (2.17) in the form,

$$\cot\phi = F.\cot\theta' \qquad (2.18)$$

where

$$F = \left(1 - \left(\frac{\alpha}{\beta}\right)^2 \tan^2\theta'\right)\left(1 + \left(\frac{\alpha}{\beta}\right)^2\right)^{-1} \qquad (2.19)$$

The factor F is then a measure of the extent by which the direction of propagation of the elementary waves deviate from the direction of the corresponding plane wave, when losses are neglected.

For $(\alpha/\beta)^2 \ll 1$, Equation (2.19) can be approximated:

$$F \simeq 1 - \left(\frac{\alpha}{\beta}\right)^2 \sec^2\theta' \qquad (2.20)$$

Although Equation (2.20) assumes "low losses", it is worth noting that it is a good approximation to cases which one normally regards as a very high loss situation (- such as a loss of 1 dB per wavelength).

It is of particular interest to obtain an expression for the actual angular deviation $\delta = (\phi - \theta')$ arising from the presence of losses. Assuming this deviation is relatively small, we find from Equations (2.18) and (2.20),

$$\delta \equiv \phi - \theta \simeq \left(\frac{\alpha}{\beta}\right)^2 \tan\phi \simeq \left(\frac{\alpha}{\beta}\right)^2 \tan\theta' \qquad (2.21)$$

$$\frac{\delta}{\phi} \ll 1$$

It has already been seen that the wavefronts of the elementary wave remain plane. However, the amplitude of the field varies along the phase front. If distance along the phase front is denoted by z', such that

$$z = z' \sin\phi \qquad (2.22)$$

the amplitude decay along a phase front is given by,

$$dU(z') = dU(0) \, e^{-Re(jk_z z' \sin\phi)} \qquad (2.23)$$

which, from Equation (2.14), is reduced to

$$dU(z') = dU(0) \, e^{-z' \sin\phi (\alpha\cos\theta' \cosh\theta'' + \beta\sin\theta' \sinh\theta'')} \qquad (2.24)$$

It is seen that the amplitude decays exponentially along the phase front. It is important to appreciate that the waves are defined only

for z > 0, and hence z' > 0. There is, therefore, no problem with

unlimited growth in the minus z' direction. The constant amplitude

fronts of the waves are the planes z = constant. The waves can be

regarded as physically wholly valid; they satisfy the wave equation;

a source could be devised which would launch a single such wave.

In some respects, one can ascribe a greater degree of physical

reality to these waves than to the plane waves used in the analysis of

loss-less systems, by the fact that the energy of a finite amplitude

elementary wave is also finite.

Figure 2.2 (a) through (d) show some examples of the elementary waves,

and indicate the changes as the relative loss, as measured by $(\alpha/\beta)^2$

is progressively increased. It is seen that the waves are decaying

in the z-direction, and hence also along the phase fronts, but have

a constant amplitude in the x-direction. The direction of propagation

of the waves is perturbed by the loss factor.

This deviation is shown in Figure 2.3 and the result is compared

with the approximate analytical solution of Equation (2.21). The

approximation is seen to be reasonably valid for values of the loss

factor, $(\alpha/\beta)^2$, less than 0.1, which covers most of the situations

encountered in practice.
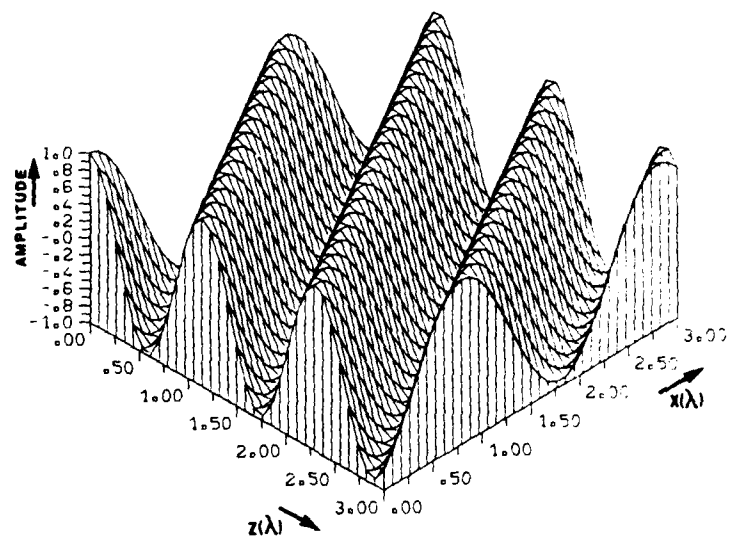
(a)
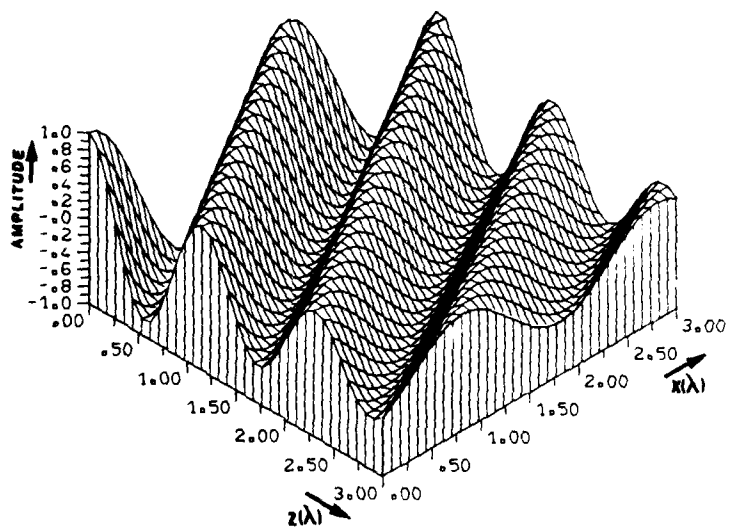
(b)

Figure 2.2: One component of angular spectrum ($\phi = 30^{\circ}$) for different values of $(\alpha/\beta)^2$: (a) 0; (b) 0.002.
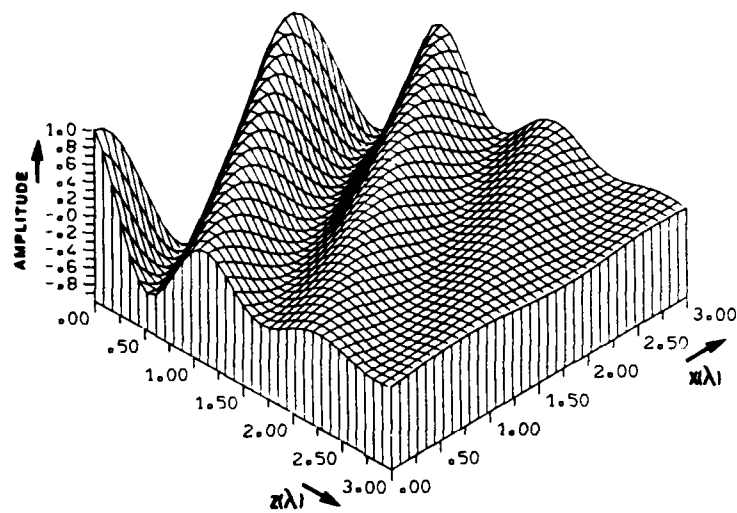
(c)
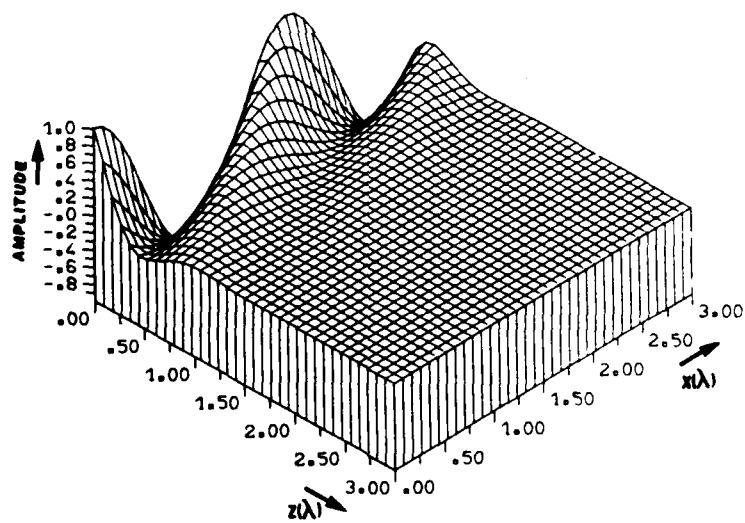
(d)

Figure 2.2: One component of angular spectrum ($\phi = 30^{\circ}$) for different values of $(\alpha/\beta)^2$: (c) 0.02; (d) 0.2.
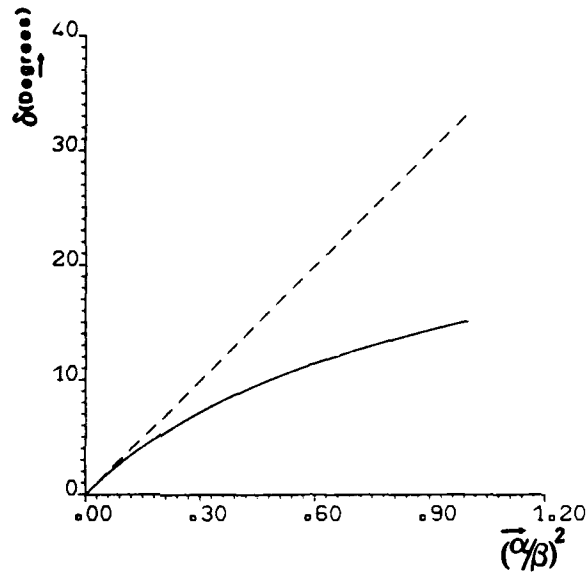
Figure 2.3:   The angular deviation δ as a function of $(\alpha/\beta)^2$; dashed line, for analytical approximate case;   solid line for analytical exact case.

2.2.3.   Low Loss Approximation for the Elementary Waves

Very simple results can be obtained for the low loss case $\alpha/\beta \ll 1$. Under these conditions, Equation (2.18) shows that,

$$
\left.
\begin{array}{l}
\theta' \simeq \phi \\[1ex]
\text{Also,} \quad \cosh\theta'' \simeq 1 \\[1ex]
\sinh\theta'' \simeq \tanh\theta'' = \left(\dfrac{\alpha}{\beta}\right)\tan\theta'
\end{array}
\right\}
\qquad (2.25)
$$

47.

Applying these approximations to Equations (2.13) and (2.14), we find, to the first order in (α/β),

$$k_x \simeq \beta\sin\theta'$$
$$k_z \simeq \beta(\cos\theta' - j\left(\frac{\alpha}{\beta}\right)\sec\theta') \qquad\qquad (2.26)$$

The elementary waves of Equation (2.15) then take the form,

$$dU(x,z) = T(f,0)e^{-j\beta(x\sin\theta' + z\cos\theta')}e^{-(\alpha z/\cos\theta')} \qquad (2.27)$$

With reference to Figure 2.1, the decay term can then be written in the form, $\exp(-\alpha\ell_2)$.

It can be concluded, therefore, that this is the correct form for the attenuation term - in agreement with that used by Alais et al (1979). The controversy as to whether high spatial frequencies decay faster or slower than low spatial frequency components is, therefore, resolved. Further, it is concluded that one would expect a loss of resolution when focussing a beam in an attenuating medium - a conclusion which is confirmed by the rigorous computations presented in the next section.

It remains to discover up to what values of parameter α/β, the results derived from the approximations of Equation (2.25) remain valid. If the attenuation is described by a term $\exp\left[-\alpha(\phi).z\right]$, we can compute $\alpha(\phi)/\alpha(0)$, as a function of ϕ. The results are shown in Figure 2.4 for three values of α/β. It can be seen that for values of α/β, as
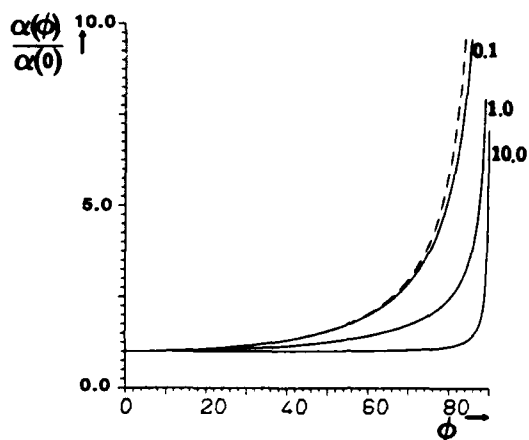
Figure 2.4:   Variation of $\alpha(\phi)/\alpha(0)$ with ϕ for different values of
α/β: Dashed line for analytical approximate case.

large as 0.1, the approximation remains reasonably satisfactory over
the whole range of ϕ.   It is unlikely, at least in acoustic micro-
scopy, that one will encounter much larger losses.

2.3   Focussing in Highly Absorptive Media.

The aim was to establish the primary effect of losses on the action
of a lens in an absorptive medium.   Using the formulation established,
and representing the lens by an aperture illuminated by a uniform
amplitude, parabolic phase waves, the field distribution can be
obtained in the focussing region.   Two typical cases are illustrated
in Figure 2.5.   For each case, we have also presented the distribution
in the paraxial focal plane, Figure 2.6.   The most striking effect is,

cf course, the direct effect of the attenuation whereby the height at the focus is, for large attenuations, substantially less than that of the sidelobes of the distribution, further "upstream". Clearly, if one is looking at water-like objects, there will be a marked effect on the depth of field. In examining solid surfaces by the V(z) technique, (Weglein and Wilson 1978; Atalar, 1978), one would also expect a marked change as a result of the coupling medium attenuation. It is also noted that the width of the main lobe changes very little, whilst there is a marked reduction in the sidelobe levels. The model used is that of a thin lens. This, it is believed, is adequate to grasp the main features of focussing in lossy liquid media. However, if one is concerned with subsurface imaging in a solid, the situation can be entirely different. The path length of the peripheral rays in the liquid can be substantially shorter than for axial rays. This results in a marked apodisation which, in extreme cases, corresponds to focussing by means of a thin annular lens. Such situations can be grasped using a Fresnel-Kirchoff approach, (Islam et al, 1982).

2.4. Discussion and Conclusion.

An approach has been presented which extends the methods of Fourier optics to the case of propagation in highly absorptive media. The elementary waves from which the solution is constructed are truncated inhomogeneous plane waves.
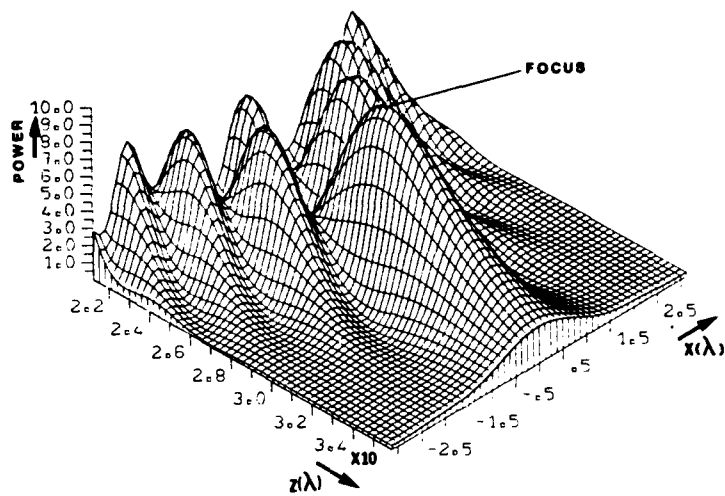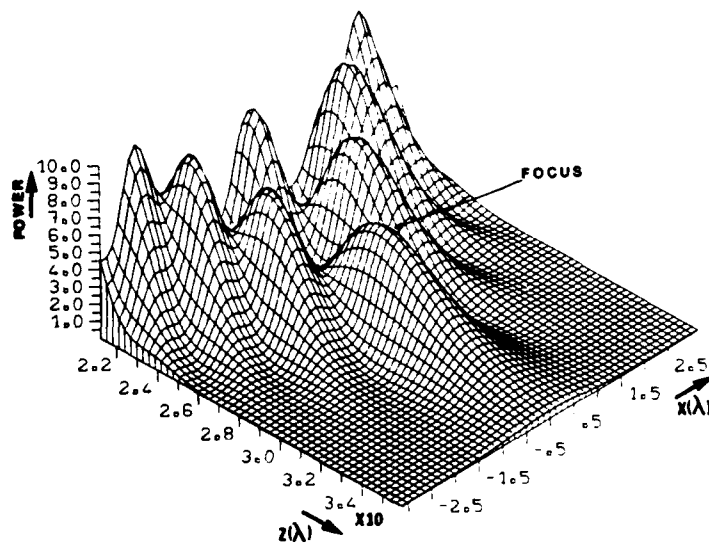
Figure 2.5: The field distribution in the vicinity of focal plane of a thin lens, (radius 30λ, aperture 52λ, velocity ratio 7.3; (a) α= 0.3 dB/λ and (b)α = 1.0 dB/λ. λ is the wavelength in the focussing medium.

51.
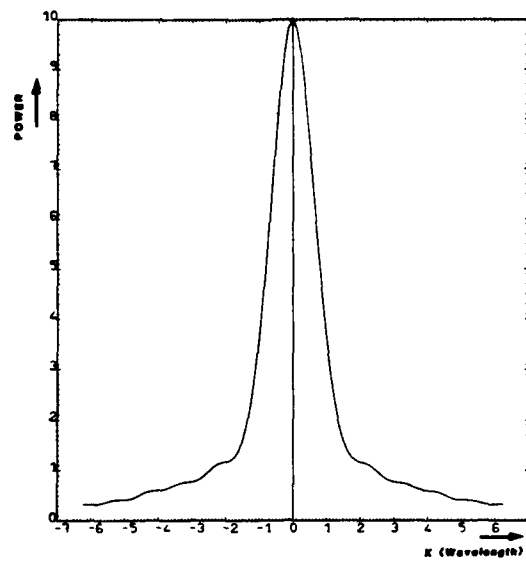
(a)
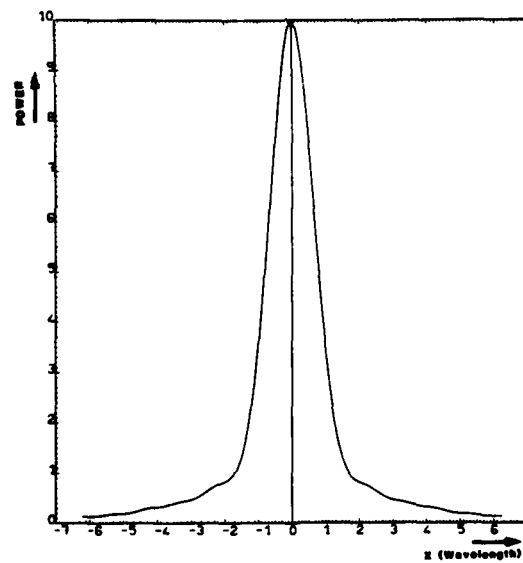
(b)

Figure 2.6:   The field distribution at the paraxial focal plane of
lens described in Figure 2.5;   (a) $\alpha = 0.3$ dB/λ and
(b) $\alpha = 1.0$ dB/λ

52.

By examining the limiting case, it has been shown that the correct
way of taking losses into account in a perturbation approximation,
leads to the conclusion that high spatial frequencies are preferentially
attenuated with respect to low spatial frequencies. As a result, the
main lobe of the field distribution in the focal plane of a lens will
be broadened by the presence of losses. However, for losses encountered
in high resolution acoustic microscopy, this effect is insignificant.
The reduction in sidelobe level is, however, much more marked.

CHAPTER 3

REFLECTION ACOUSTIC MICROSCOPY AT 1 GHz

3.1   Introduction

In this Chapter, the design of the high frequency reflection SAM

is described. Since the first results obtained in December, 1979,

various sets of scanning and RF electronics have been tried. The

mechanical construction of the system has also been modified a

number of times. It would take much space and would be exhaustive

to go through this evolutionary process. Therefore, in this

introduction, only an outline of the progress is given and the

latest design of the microscope is presented in the body of the

Chapter.

In the first acoustic microscope, demonstrated by Lemons and

Quate (1974a), a loudspeaker was used to scan the object in X and

a slide mechanism provided the Y scan. Wickramasinghe (1976)

modified the loudspeaker assembly to a voice-coil leafspring scanner

and used this structure for both X and Y scans. This scanner consists

of the voice-coil of a loudspeaker attached to a pair of leafsprings

which hold the lens, Figure 3.1.
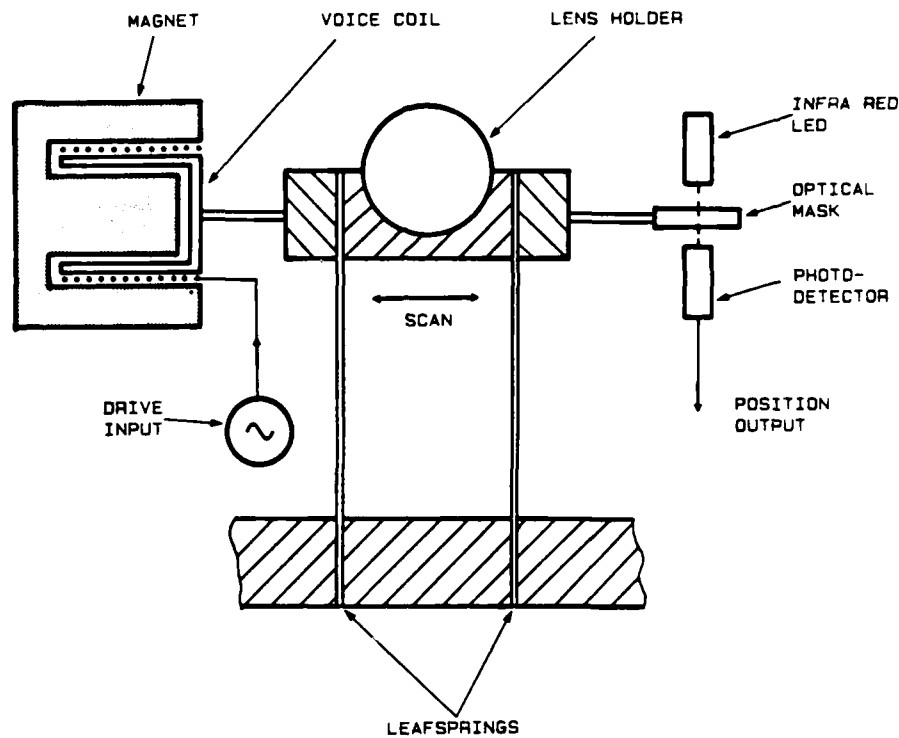
Figure 3.1.   The schematic diagram of a voice-coil leafspring
scanner with infra-red position encoder.

As the focussed beam is scanned over the object, two position sensors
read the X and Y positions, and provide the information required by
the display system. The position sensor illustrated in Figure 3.1
is an infra-red one. An optical mask, through which the transmitt-
ance varies linearly with position, is mounted on the lens holder,
(Jipson, 1979a). As the lens scans, the voltage detected by the
phototransistor is a direct measure of the position.

The design of Figure 3.1 was originally adapted for both of the scanners, and a microscope was constructed. One of the major advantages of a double leafspring scanner is the short achievable frame time. However, the main problem with such a scheme was that, since the object was attached to one pair of leafsprings and scanned, its alignment with respect to the other scan plane was difficult. Failure to align the object, normal to the lens axis, leads to spurious fringes on the final image, arising from resulting phase variations. Further, since in this research the fast frame rates were not of concern, it was decided to remove one of the leafspring scanners – namely the slow scan, and to resort to a motor driven micro-positioner.

The acoustic attenuation, at 1 GHz in the water at room temperature, is 200 dB/mm; raising the temperature to 50°C, the attenuation is reduced to 104 dB/mm, (Attal and Quate, 1976). A heater consisting of a coil wrapped onto the water bath was incorporated on the tilt plate. The 1 GHz reflection instrument, constructed by the author, is illustrated in Figure 3.2. The voice coil, leafsprings, lens holder, water bath and focus micrometer can clearly be identified.

In parallel with applying this microscope to a range of NDE problems, instrumental developments to the system itself have been borne in mind throughout the research programme.
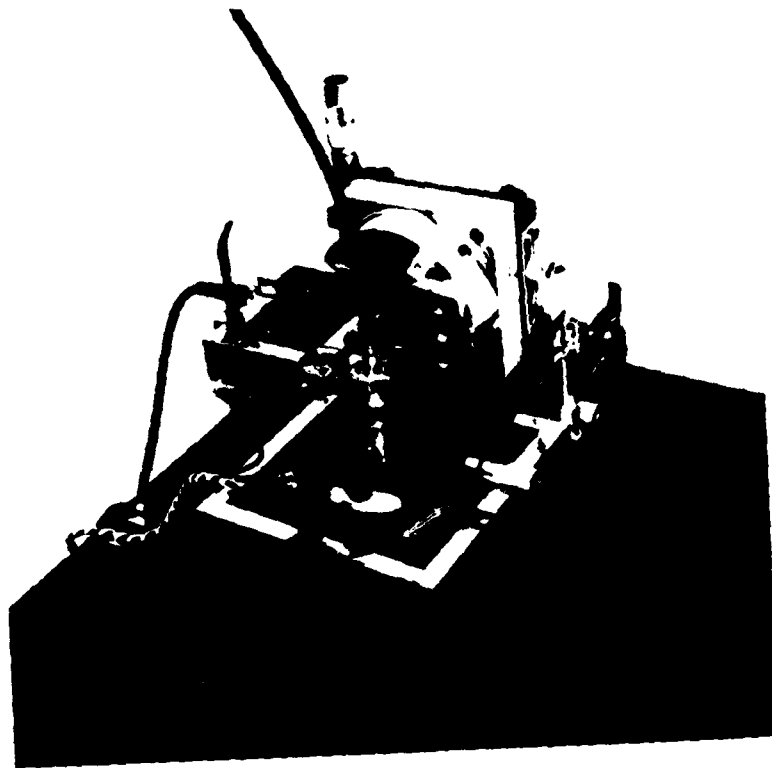
Figure 3.2:   The constructed 1 GHz reflection system.

3.2.   The transducer:lens design.

The design of high frequency acoustic lenses has already been dealt
with,(Jipson, 1979a). As pointed out in the Introduction to the
thesis, the high velocity ratio across the spherical cavity brings
the energy down to a nearly diffraction limited focus at the focal
plane. Here, the discussion is limited to a qualitative review
for basic transducer: lens design.

At the back of the lens rod, a sputtered ZnO transducer is formed between two CrAu electrodes. This transducer structure is almost universal for high frequency lenses, (i.e. above 300 MHz). At low frequencies, a plate transducer, (e.g. lithium niobate) is bonded to the buffer rod. The transducer converts the applied electromagnetic pulse to an acoustic pulse which travels along the rod in the form of a quasi-plane wave. The spherical lens produces the appropriate phase curvature on the wavefronts to bring the energy to focus at the focal plane. In the receiver mode, the lens recollimates the reflected acoustic energy and the transducer converts it back to an electromagnetic signal.

The frequency of operation is the determining factor for the choice of the material for the lens rod. However, in general, the material must have two qualities: (i) it must have high velocity - for low spherical aberration and (ii) it must have low acoustic absorption. For most polycrystalline solids, the main source of attenuation is attributed to grain boundary scattering. This process can also cause a reduction in the contrast of the micrographs. Therefore, ordinary metals are suitable only for very low frequency applications (below, say, 20 MHz). Although amorphous materials - such as fused quartz - are certainly the best candidates for medium frequency range (below 500 MHz), they may be used for frequencies of up to 1 GHz. At high frequencies, single crystal insulators are essential. For such materials, grain boundary scattering loss is not present. Also, thermoelastic losses are small and the only loss mechanism is the interaction of the coherent phonons with thermally generated phonons -

the Akhieser mechanism, (Auld, 1973) - with a negligible significance.

Of the many single crystal dielectrics, sapphire is particularly good because it has a high velocity, (11 Km/s), low attenuation, (less than 0.5 dB/cm at 1 GHz). Moreover, when being polished, it is relatively easy to obtain a good surface finish. Although the high velocity ratio at the lens:couplant interface makes it possible to achieve a diffraction limited focus, it is also, unfortunately, in a majority of cases, associated with a large impedance discontinuity at this interface, which results in a large reflection loss, (such as 9 dB for sapphire:water interface for a plane wave at normal incidence). The loss can be greatly reduced by the inclusion of a quarter wavelength matching layer. Sputtered glass can have an impedance needed to act as an impedance transformer, (Weglein, 1976; Kushibiki et al, 1981).

Owing to high water losses at high frequencies, one tends to use lenses with smaller radii of curvature - to minimise the path losses. For high frequencies, lenses with radii of curvature of much less than 1μm are employed. For a 1 GHz lens, a radius of curvature of about 100mm is typical. For even higher frequencies, still smaller lenses are used; recently, an acoustic lens having a radius of 10μm was successfully fabricated, (Faridian, 1982).

The length of the crystal rod is an important design parameter;
it must satisfy two requirements: Firstly, it must be such as to
provide a temporal separation between the echoes from the surface
of the lens and the object echo. Normally, the lens geometry is
chosen so that the information pulse falls in a time-window between
two successive echoes from the lens:water interface. To obtain a
good focus, the lens should be illuminated as uniformly as possible.
Secondly, therefore, the rod length should be chosen so as to provide
a uniform illumination on the back of the lens, (Jipson, 1979a).
The details of the effect of various lens parameters, such as glass
matching layer thickness and the liquid attenuation on the performance
of an acoustic lens can be found in literature, (Wickramasinghe, 1979;
Nikoonahad and Ash, 1982).

3.3.   RF electronics.

The operation of a reflection microscope is somewhat similar to a
pulsed radar system. The RF electronic system is illustrated in
Figure 3.3.

At the transmitter, a signal generator serves as the source (Marconi
6055B). A GaAs FET power amplifier (Avantek APG2052M), employed
after the signal generator, is capable of producing up to 27 dBm
of CW power. Typically, 20 dBm power is adequate for taking good
quality images. This signal is pulsed by means of two cascaded

60.
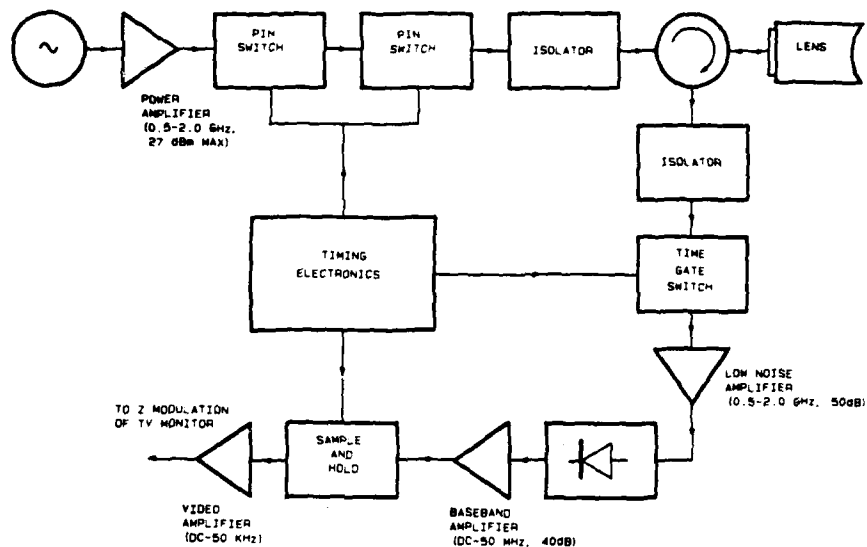
Figure 3.3.:   RF electronic set-up for the 1 GHz system.

microwave PIN switches (HP33144A). For a given dynamic range, the
minimum acceptable on:off ratio through the switches is dictated
by the loss through the lens system. At 50°C, the total measured
two way loss in the lens system was 61 dB at 950 MHz. This includes
the transducer insertion loss, diffraction and propagation loss in
the lens, reflection loss at the lens:water interface and path loss
in the water cell. The on:off ratio obtained with two PIN switches
was more than 100 dB which was more than adequate.

The transducer bandwidth sets the minimum pulsewidth and the length of the lens rod sets the maximum pulsewidth. The repetition frequency of the pulses is set by the magnitude of the successive echoes from the surface of the lens. This in turn depends on how well the lens is matched from both ends; at the lens side, the quality of the glass matching layer is critical; at the transducer side, the conversion efficiency of the transducer is the determining factor. Typically, 100 ns pulses are used with a PRF of 200 KHz (duty cycle of 2%).

The pulses are transmitted through an isolator (RYT200122) and then a circulator (RYT300034), to the transducer. On the detection side, a time gate supresses the echoes from the surface of the lens and other unwanted signals. The object signal is subsequently *amplified* by a *low noise amplifier* (Avantek AWT2035M) and detected with a standard microwave crystal detector (HP423A). Following baseband amplifications, the sample-and-hold circuit produces the video signal which is used to intensity modulate the intensity of the electron beam of the display.

3.4.   Scanning and position sensing.

One of the problems associated with the voice-coil scanner was that the small tolerance available in the magnetic gap made the alignment of the coil, within the gap, difficult. Failing to align the coil in the gap can easily lead to rubbing against the magnetic pole. The

62.

problem associated with the infra red position sensor was noise;
ambient optical noise and the photodetector noise. A new leafspring
scanner and velocity encoder were designed and constructed, Figure
3.4.
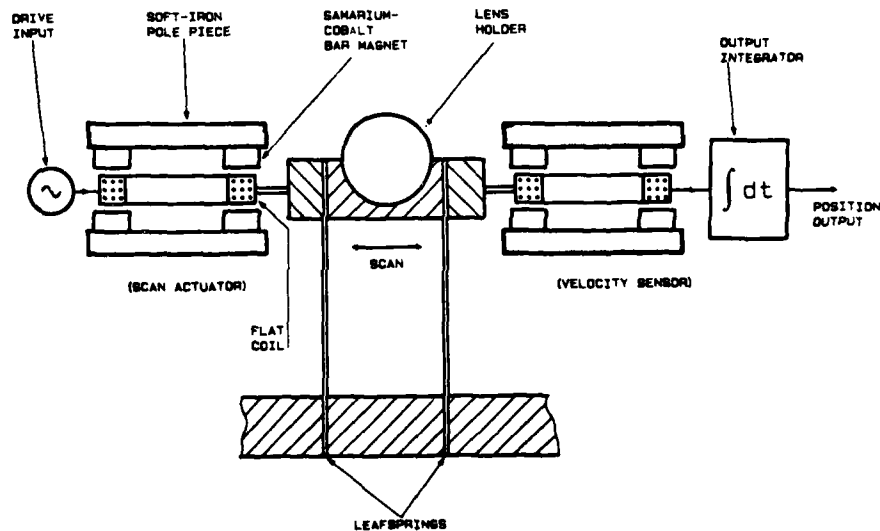
Figure 3.4:   A complete scanner:position sensor assembly with
               two flat coils for both scanning and velocity
               sensing.

Principally, the operation of this system is similar to that of the
voice-coil scanner system. Two *flat* coils act as scan actuator and
velocity encoder. For each case, the magnetic gap is realised by
means of four samarium-cobalt magnet bars and soft iron pole pieces.

Flat coil scanners have already been used for cryogenic acoustic microscopy, (Rugar, 1981). One significant advantage of a flat coil scanner is a relatively large gap, which facilitates the alignment of the coil. The positional signal - which is used for the X-scan of the display - is obtained by integrating the detected velocity signal.

The scan electronics, for the X-scan, consists of a phase-locked loop with which the scan frequency is locked to the electricity supply. Scanning at 50 Hz, and subharmonics of 50 Hz, is possible.

Y-scan is carried out by a motor driven translation stage. To avoid the transmission of high frequency vibration from the motor to the stage, a flexible coupling is included between the motor shaft and the stage micrometer. Y position sensing is carried out by means of a high resolution multi-turn potentiometer.

3.5.   Image formation.

Due to mechanical scanning, fast video, commensurate with TV rates cannot be achieved. The X and Y signals from the position sensors and the video output of the microscope cannot, therefore, be directly connected to a TV monitor. The simplest way to display the information is to use a display tube. A number of results have been obtained in this way. A problem here is the limiting available dynamic range. It is easy to saturate a display tube and, normally,

pictures obtained with this system are poor in the number of grey
levels.

One alternative is to use a digital frame store. Here the information
is digitised and stored in an electronic memory, during a frame scan
at the microscope video rate. The information in the memory is then
continuously written to the television set at the standard TV rate.
A number of results have also been obtained with the digital frame
store constructed at University College London, (Burton and Pino,
1982).

3.6.   Microscope performance.

Table 3.1 summarises the performance of the 1 GHz microscope
constructed:

Frequency:	1 GHz
Lens material:	Al_2O_3
Lens radius:	100μm
Focal length:	115μm
Lens aperture:	150μm
Length of the lens rod:	2.0mm
Surface resolution:	~1μm
Lens insertion loss:	61 dB (at 950 MHz, at 50°C)
Pulse width:	100 ns
PRF:	200 KHz

Dynamic range:	60 dB (at 50°C)
Line scan:	50 Hz
Frame time:	5 - 50 s
Field of view:	100μm - 700μm square
Video frequency:	10 - 70 KHz

Table 3.1:   The performance of the 1 GHz reflection acoustic
              microscope.

3.7.   Applications and results.

The microscope has been used for surface NDE of a wide range of
objects. Microelectronic components, including microwave devices,
metallurgical samples and a range of ceramics and dielectrics have
been imaged with this reflection system.

3.7.1.   Microelectronics

The structure of most integrated circuits consists of up to six
layers. The adhesion of the layers, as well as the existence of
microcracks, inclusions and voids in any layer, play an important
role in the final reliability of the device. A primary application
of a reflection system is to image defects in the metallisation
tracks. A part of an integrated circuit, imaged at 950 MHz, is
illustrated in Figure 3.5. In this micrograph, a surface defect,
indicated by the arrow, is clearly visible.
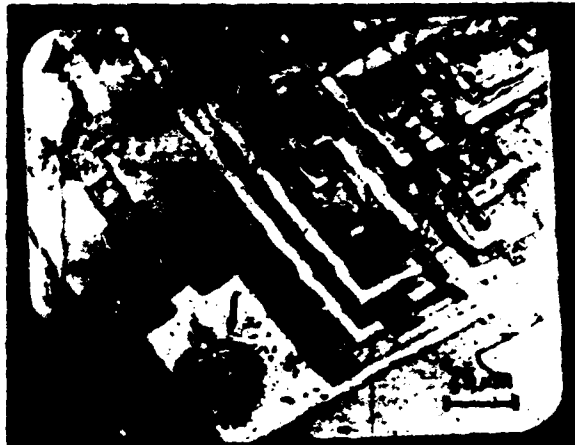
Figure 3.5:   Surface micrograph of an integrated circuit

imaged at 950 MHz. The arrow indicates a defect

on one of the pads. The ripples are artifacts

of the scanner.

Two micrographs obtained from the control logic of a 64 K RAM chip
are illustrated in Figures 3.6 (a) and 3.6 (b).

Visually, the micrographs are as good as optical micrographs.
However, because of the penetration of the acoustic radiation below
the surface, micrographs of this kind, in general, show more contrast
than optical and SEM micrographs, conveying information about near
surface planes.
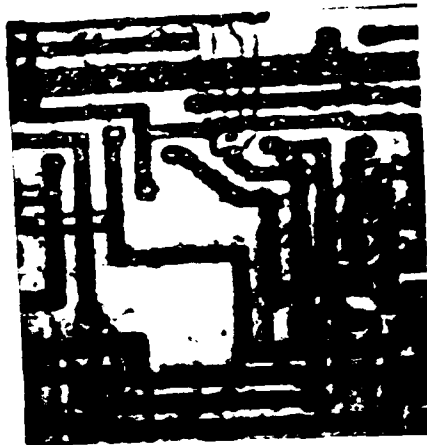
(a)
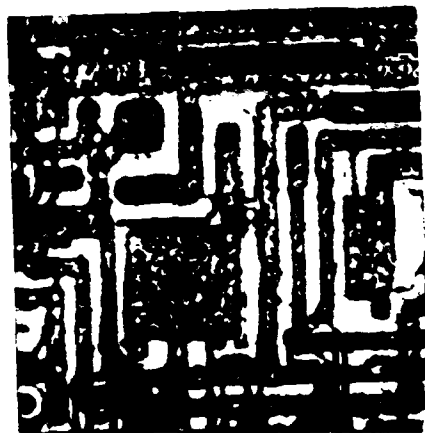
(b)

Figure 3.6 - (a) and (b):   Different parts of a 64 K RAM chip
imaged at 1 GHz, the field of view is
250µm x 250µm.

A number of IMPATT microwave diodes have been examined with the reflection system. In a typical device, a 6μm thick silicon device is bonded to a metallised diamond heatsink. The main theme for acoustic examination of these devices is to provide a non-destructive examination of the Si:heatsink bond. Two typical micrographs, obtained from two devices, are presented in Figures 3.7 (a) and 3.7 (b).

In each case, across the silicon diode, a high degree of non-uniformity is present. Part of this nonuniformity, however, is due to surface features. With 100 ns pulses used, no temporal separation between the surface echo and the bond echo was possible; taking the velocity in silicon to be 8.4μm/ns, pulses shorter than 1.43 ns would be needed to perform time gated imaging on these devices.

For each IMPATT device, the diamond heatsink is embedded and bonded to a copper heatsink, as shown in Figure 3.8. Again, a check on the quality of this bond is of interest. The micrographs present-ed in Figure 3.9 illustrate an air gap between the diamond and the copper. This micrograph has been obtained by imaging the sample from the top. To image the bond, lenses with a larger radius would need to be used.

(a)

(b)

Figure 3.7: Micrographs obtained from IMPATT diode:heatsink bonds: (a) hemispherical diamond heatsink and (b) rectangular heatsink. For each case, the diameter of the diode is 60µm.
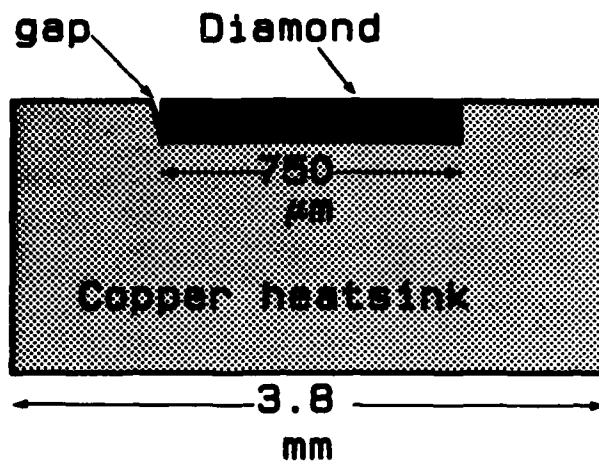
Figure 3.8:   Schematic diagram of diamond:copper heatsink.
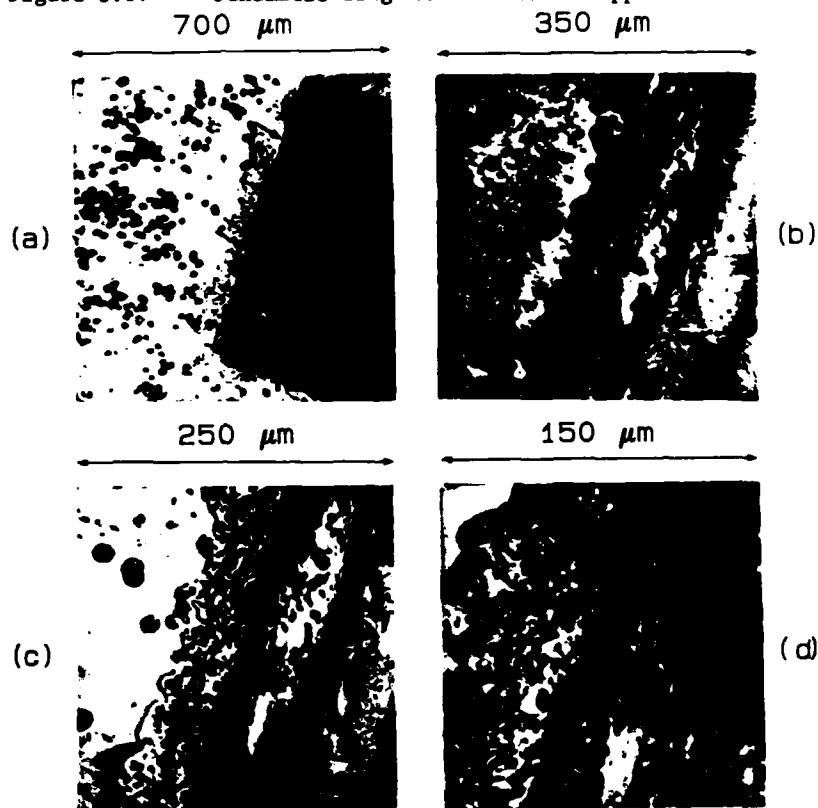
Figure 3.9:   A diamond:copper heatsink imaged at 1 GHz with
                different magnifications: Arrows indicate a gap.

3.7.2.   Metallurgy

The reflection acoustic microscope can be used for purity test
purposes. Figure 3.10 illustrates a micrograph obtained from a two-
metal-matrix. The structure consists of iron particles with an
average size of 50µm, embedded in a copper binder. Owing to high
differences in elastic and attenuation characteristics of iron and
copper, the particles can be imaged and visualised with high contrast.

Figure 3.10:   Polished surface of a two-metal-matrix;   iron
                  particles in a copper binder;   picture taken at
                  950 MHz.

It is known that a wide angle acoustic lens produces leaky surface

(Rayleigh) waves which travel several wavelengths on the surface

and decay in about one wavelength in depth. It has been shown

(Atalar, 1979) that inclusions and voids lying within one Rayleigh

wavelength of the surface,affect the surface wave and hence the

final microscope signal. Further, the Rayleigh wave is strongly

scattered in the presence of a surface breaking crack. The

detection and imaging of surface breaking cracks is a major theme

in the applications of reflection microscopy to NDE. In most cases,

the gap of a microcrack is filled with air - even when the sample

is immersed - because of the surface tension. This implies high

changes in reflectivity as one scans over the crack - both for the

beam and the Rayleigh wave. This effect provides the means for

detection of cracks with widths much less than the resolution of

the system. A body crack (compact tension specimen) in dural,

imaged at 950 MHz, is illustrated in Figure 3.11. The crack can be

viewed with high contrast and the features, which are smaller than

1μm (indicated by an arrow) can clearly be seen.

3.7.3.   Dielectrics and Ceramics

Pores in ceramics can be readily imaged in the acoustic microscope.

A fluid filled porous ceramic has large impedance variation in its

structure, and can give high contrast. A part of an alumina ceramic

has been imaged at 880 MHz, Figure 3.12. The surface porosity can be

clearly seen. Further, defects in the structure can be seen, indicated
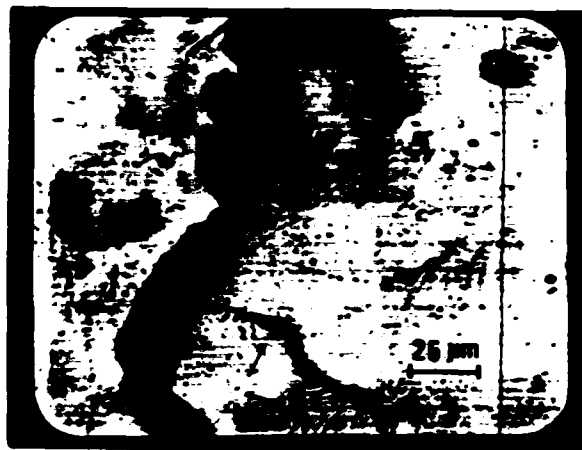
Figure 3.11:   A body crack in a compact tension specimen taken
               at 950 MHz.
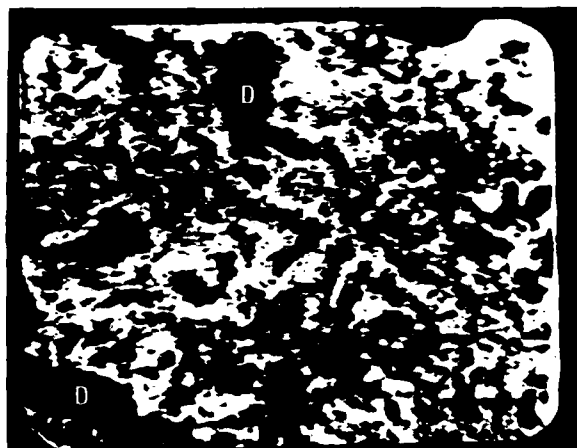
Figure 3.12:   Polished surface of a porous alumina ceramic imaged
               at 880 MHz.

by "D", whose size is larger than the average size of the pores. Along the lines of the arrows, the pores have a consistent trend; this is probably a crack.

Examples of microcracks in a dielectric are shown in Figures 3.13 (a) and 3.13 (b), where the small cracks in a glass slide have been imaged at 1 GHz. In Figure 3.13 (b), a 7μm crack across the field of view, as well as a 1μm crack, indicated by an arrow, can be seen.

Acoustic microscopy provides the means of characterising layered media. For the case of one single layer on a "substrate", the front face reflection and the reflection for the film:substrate interface interfere. This interference phenomenon gives rise to the formation of fringes on the micrograph, with periodicity which is a measure of the local film thickness. The visibility of the fringes indicates the Q of the water-film-substrate "cavity", which, in turn, determines the local impedance. Figures 3.14 (a) and 3.14 (b) show different parts of a moisture resistant paper used for packaging, imaged at 880 MHz.

The retarding layer is a thin film coating the surface of the paper. While Figure 3.14 (a) illustrates the surface roughness on the retarding layer, for some defocussing, the formation of fringes can clearly be visualised in Figure 3.14 (b).

75.
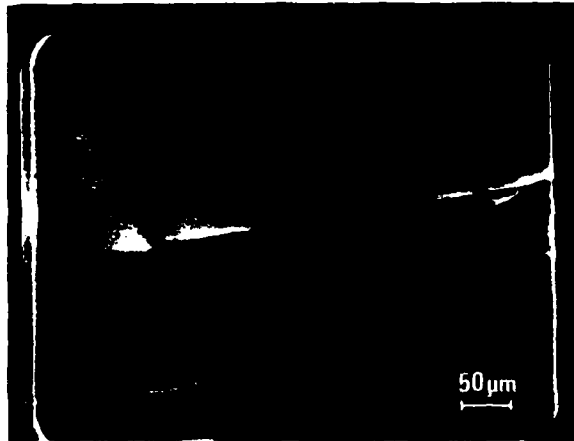
(a)
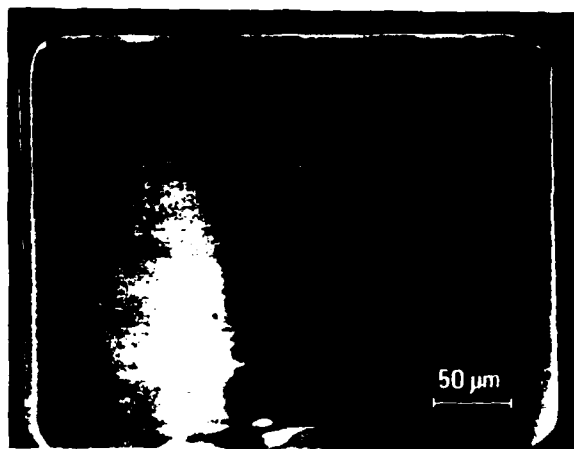
(b)

Figure 3.13 (a) and (b):   Cracks in a glass slide imaged at 1 GHz.
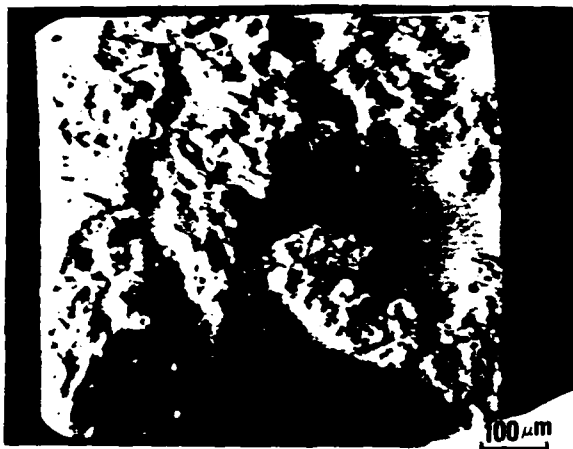
(a)

(b)

Figure 3.14:   Images obtained from a moisture resistant paper.
(a) indicates the roughness on the surface of the
impeding layer and (b) shows the interference in the
coating layer; images taken at 880 MHz.

77.

3.8.   Discussion and Conclusion.

A number of design aspects for a 1 GHz reflection microscope have been described. A reflection microscope has been constructed and its performance explored. This microscope has been applied to a wide range of NDE problems. A number of surface micrographs - some of which are presented - have been obtained. In all the micrographs presented here, the estimated resolution agrees with the theoretical prediction. We believe that high frequency reflection acoustic microscopy provides useful techniques for surface NDE of objects. However, more quantitative measurements are required before the merits of a SAM can be compared to those of an optical microscope for surface NDE.

One observation has been made in the context of imaging layered media. We believe that the fringes provide information on the local film thickness and impedance. To extract this data, again, a quantitative assessment of the contrast is required, as well as mathematical modelling of the layered structure. These in turn are interesting subjects for further investigations.

CHAPTER 4

SUBSURFACE NDE WITH REDUCED APERTURE LENSES

4.1.   Introduction.

Acoustic microscopy allows the examination of subsurface planes
within optically opaque solids, (Tsai et al, 1977). For
applications where the anticipated image contrast depends on the
elastic properties of the object, acoustic microscopy is the only
choice – there is competition neither from X-rays, nor from neutrons.
Imaging subsurface voids and inclusions, as well as characterising
metallic diffusion bonds are some of the promising applications of a
reflection SAM. However, when attempting to focus an ultrasonic beam
below the surface of a high velocity material, one immediately
encounters three basic problems:

(i)   Most solid objects have a high acoustic impedance. This
        results in a high reflection loss at the coupler:object
        interface which, in turn, reduces the final detection
        sensitivity of the image pulse. The problem can be over-
        come, to a certain extent, if one is prepared to resort to
        a liquid metal coupling medium, (Jipson, 1979; Attal, 1980).
        However, in many cases, it is necessary to use water, or
        other non-contaminating liquids, as the coupler. It was
        decided to use water as the coupling medium.

(ii)   The high velocity discontinuity at the interface imposes

a high spherical aberration on the ingoing beam. In

principle, one would need an aspherical lens to compensate

for the interface phase distortion, (Pino et al, 1981).

It has previously been discussed how, by means of reduced

aperture lenses - with a water coupler, the aberration can

be minimised, (Nikoonahad et al, 1982).

(iii)   The pulse coming from the image plane arrives very shortly

after the surface reflection. The "glare" from the front

surface echo can be tolerated if the surface is perfectly

smooth and, hence, devoid of contrast. There is then no

absolute need to separate it from the signal, since it

merely provides a constant additive level. However, it will

use up some, and possibly a large part, of the available

dynamic range. If - and this, in our experience, tends to

be the more usual problem - the surface is not devoid of

contrast, it becomes essential to remove this echo by time

gating. Therefore, narrow pulses need to be used in order

to separate the image pulse by time gating. One relies on the

frequency characteristics of the transducer to convert the

RF pulse to a broadband acoustic pulse. The design of broad-

band transducer systems is, in itself, a major theoretical

and technological problem, (Reeder and Winslow, 1969; Desilets

et al, 1978).

80.

In this Chapter, the design of reduced aperture lenses for sub-surface imaging of a *wide range of solids* is first described. A specific example on a 40 MHz lens design and fabrication is presented. In addition, some specific transducer structures for broadband operation will be examined and a simple bonding technology for transducers working below 100 MHz will be outlined. Acoustic micrographs, obtained from artificially made test samples, are presented and followed by results obtained from NDE imaging of transistor: header bonds.

4.2   Lens Design for Subsurface Imaging.

Figure 4.1 shows the peripheral ray paths for the lens-liquid-solid configuration.
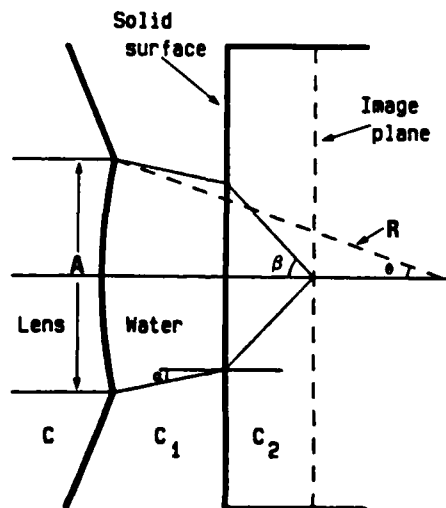
Figure 4.1:   The path of peripheral rays coming to focus below the surface of a solid.

The starting point is to choose β, the angular aperture of the rays at the focus. If one makes this angle somewhat smaller than that for focussing in water, the resolution is slightly degraded, but the spherical aberration is reduced by a much larger factor; spherical aberration depends on the third power of the angle. Thereafter, nothing more than Snell's Law is needed to derive the required lens characteristics:

$$\alpha = \sin^{-1}\left(\frac{1}{r_o}\sin\beta\right) \qquad (4.1)$$

where r_o is the object velocity ratio in the form C_2/C_1. It can easily be shown that:

$$\theta = \tan^{-1}\left(\frac{r_\ell\sin\alpha}{r_\ell\cos\alpha-1}\right) \qquad (4.2)$$

where r_ℓ is the lens velocity ratio in the form C/C_1. Also, we have:

$$A/R = 2\sin\theta \qquad (4.3)$$

where A and R are the aperture diameter and radius of the curvature of the lens, respectively. The choice of β immediately leads to the required value of A/R. This relationship is shown for a number of materials in Figure 4.2.
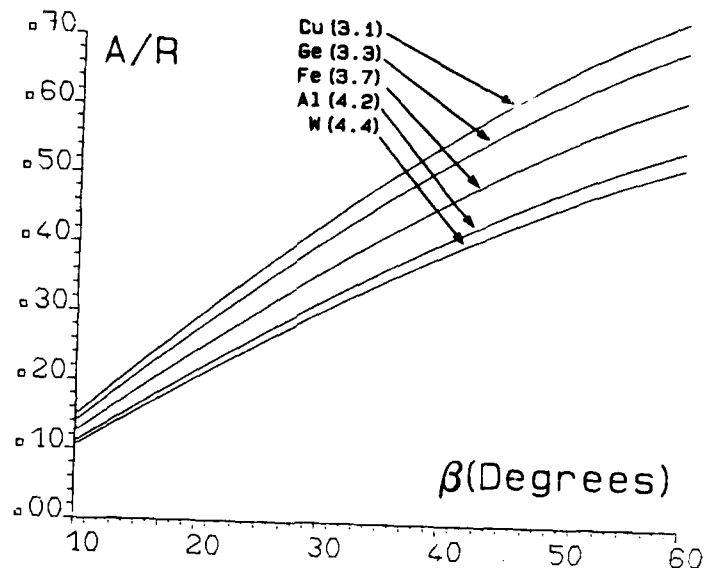
Figure 4.2: Variation of A/R of a reduced aperture lens with the focus angle β, for some typical solids. r_ℓ is 4.0 (i.e. quartz lens and r_o is given for each material).

It is seen that, for typical solids, the variation of r_o is not very great so that one could hope to use the same lens for a number of materials. For β of 40°, an A/R value of 0.4 is acceptable. Finally, the lens aperture, A, needs to be determined. Clearly, the minimum value is given by the diameter of the ray bundle at the surface of the solid; that is, for a lens which just touches the surface. By placing the lens further away, a greater range of focussing can be obtained. At low frequencies, one would opt for a relatively large lens-specimen spacing. At higher frequencies, the losses in the coupling medium dominate, and the lens specimen spacing is reduced to the minimum.

The length of the lens rod is dictated by two factors: a) It should ensure a uniform lens illumination and b), it must be long enough, so that the reverberating pulses in the lens rod and the liquid cell can be separated from each other. - Fulfilment of both these criteria rely on the choice of material for the lens. At low frequencies, in the range 20 - 100 MHz, fused quartz, as opposed to sapphire, is a good choice for a number of reasons:

(i)   A relatively large lens is needed, (typically 1-5 mm radius), and the grinding rate of quartz is faster.

(ii)   The velocity in quartz is almost half of that in sapphire; leading to a reduced reverberation time and thus facilitating time gating.

(iii)   The two way reflection loss at the quartz:water interface is 9 dB (for plane waves at normal incidence). For sapphire, this loss is 18 dB. It should be mentioned that, although at high frequencies, for a sapphire:water interface, sputtered glass can be a good matching layer (Weglein, 1976; Kushibiki et al, 1981), at 40 MHz, one would need a rather thick glass film - about 35μm.

The specification for a particular lens, designed for 40 MHz interior imaging is given in Table 4.1.

Frequency:	40 MHz
Material:	Fused Quartz
Radius:	10 mm
Aperture:	4 mm
Transducer diameter:	4 mm
Rod length:	27 mm (one Fresnel distance from the transducer)

Table 4.1:   Design Specification for the 40 MHz Reduced Aperture
              lens

4.2.1.   The Lens Fabrication

The lens described in Table 4.1 was fabricated taking the following
steps:

(i)   Lapping and polishing the two ends of the quartz rod.

(ii)   Grinding the lens by means of 10 mm radius steel balls,
           mounted as a tool on an ultrasonic drill and using silicon-
           carbide powder.

(iii)   Polishing the lens by means of steel balls and diamond
           pastes, starting from a paste with coarse particle size
           (25µm) and resorting to finer pastes with a final polish
           of better than 1µm.

4.2.2. Performance of the Lens

The focussing obtained within a solid has been studied using a full two-dimensional Fourier optics formulation, (Pino et al, 1981). It confirms that, by using this simple design technique, it is possible closely to approach diffraction limited focussing for a substantial range of depths, for a single lens. A further insight can be gained by tracing the rays coming to and from a focus. Figure 4.3. shows the focussing performance of the lens at three different depths below the surface of copper ($r_o = 3.1$).

Figure 4.4 shows the case when focussing into tungsten ($r_o = 4.4$).

It is seen that the geometrical focussing performance of the lens remains good over a substantial *range* of focus. Therefore, it can be concluded that, by means of a suitably designed reduced aperture lens, one can probe a substantial depth below the surface of most commonly used solids.

4.3. Transducer Bandwidth Considerations

As noted in the Introduction, the attainment of the highest possible bandwidths is essential for the imaging of near-surface objects. The design of transducers bonded via an intermediate layer to a solid is well understood, (Reeder and Winslow, 1969; Desilets et al, 1978). It was decided to use the Krimboltz-Leedom-Mattaei (KLM) transducer equivalent circuit, (Krimholtz et al, 1970) and a number of transducer structures were studied - relevant to acoustic microscopy.

86.

Tics = 2.0mm

Tics = 0.5 mm

Depth = 0.5mm

(a)

Lens   Water   Copper
                             object

Depth=1.5mm

(b)

Depth=2.5mm

(c)
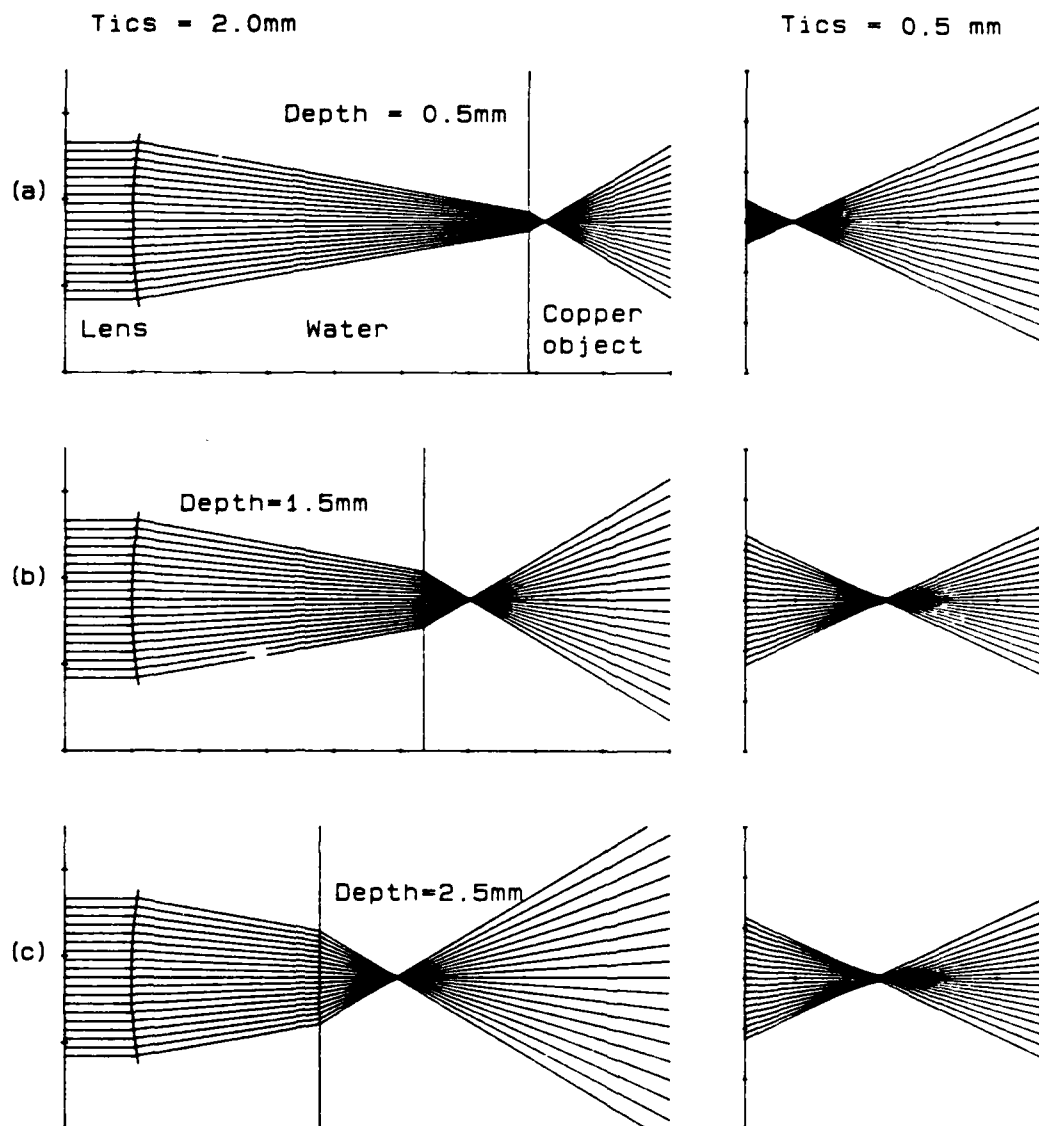
Figure 4.3:   Focussing below the surface of a copper object:
               (a) 0.5; (b) 1.5; (c) 2.5 mm below the surface.
               A/R of the lens is 0.4 and the coupling liquid is
               water.
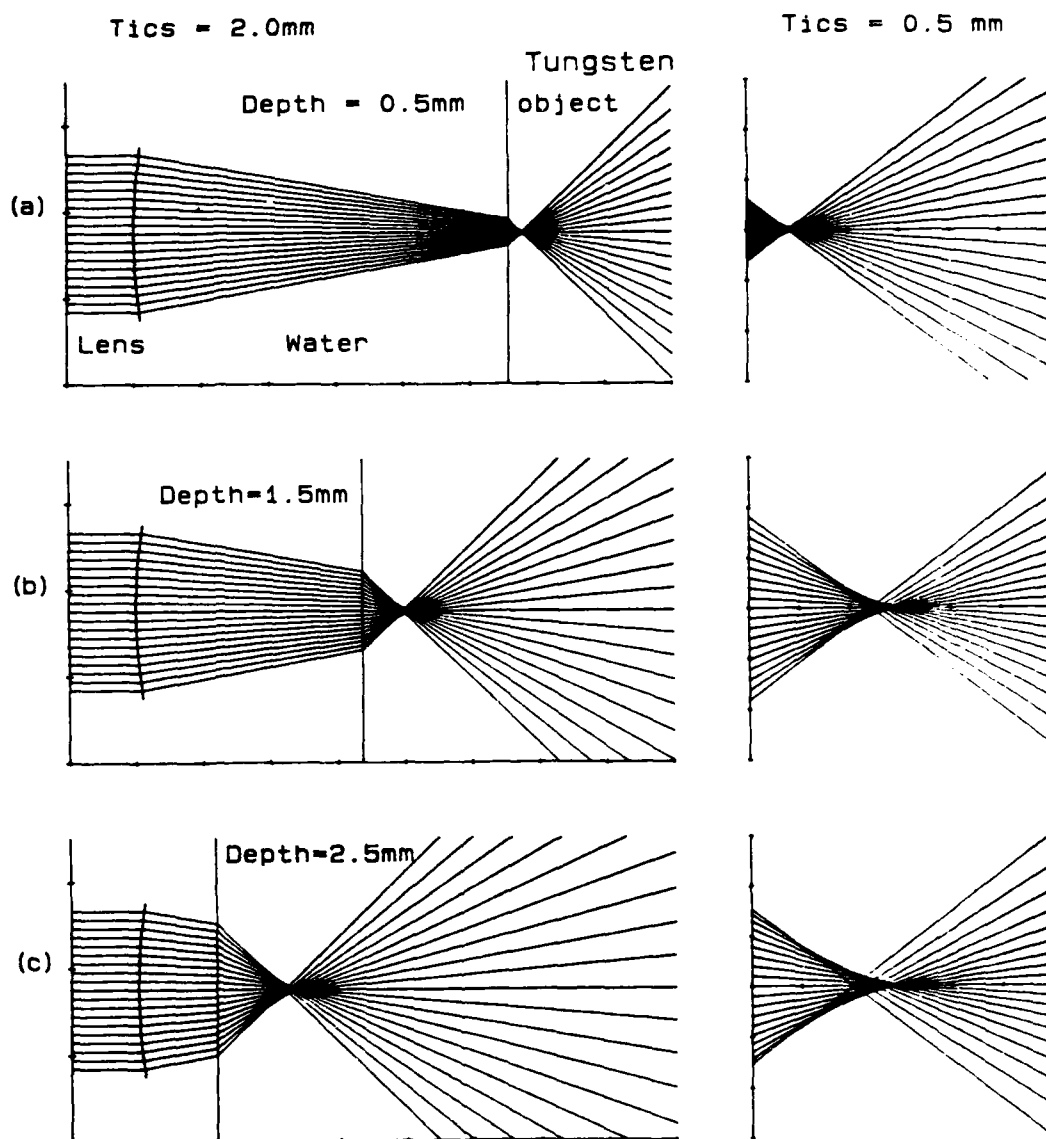
Figure 4.4: Focussing below the surface of a tungsten object:
(a) 0.5; (b) 1.5; (c) 2.5 mm below the surface.
A/R of the lens if 0.4 and the coupling liquid is
water.

4.3.1. The Transducer Model

The KLM equivalent circuit is illustrated in Figure 4.5.
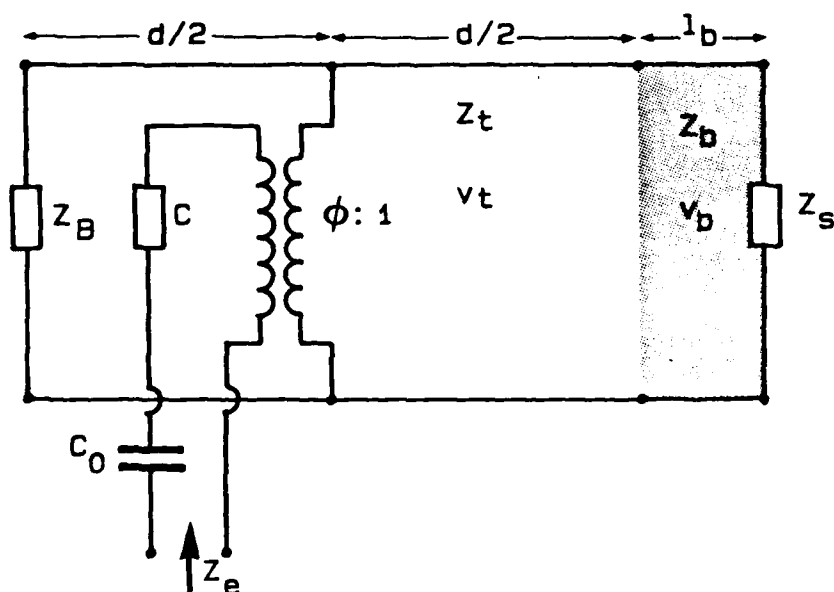
Figure 4.5: Schematic diagram for the KLM transducer model.

The formulation used is due to Desilets et al, 1978. Thus,

$$\phi = \frac{k_t}{r} (\omega_o C_o Z_t)^{-\frac{1}{2}} \text{sinc} \left(\frac{\omega}{2\omega_o}\right) \tag{4.4}$$

$$C = -C_o / k_t^2 \text{sinc} \left(\frac{\omega}{\omega_o}\right) \tag{4.5}$$

where

$$\text{sincX} = \frac{\sin(\pi X)}{(\pi X)} \qquad (4.6)$$

Also,

d : Transducer thickness

r : Transducer radius

ϵ : Transducer clamped dielectric constant

Z_t : Transducer impedance

v_t : Velocity in the transducer material

ℓ_b : Thickness of the bonding layer

Z_b : Impedance of the bonding layer

v_b : Velocity in the bonding layer

Z_s : Substrate impedance

Z_B : Backing impedance

ω_o : $\pi v/d$, half wavelength resonant frequency of transducer

C_o : $\epsilon \pi r^2/d$, clamped capacitance of the transducer

k_t^2 : Electromechanical coupling coefficient

Z_e : Input impedance at the electrical port

The insertion loss is defined as,

$$10 \log \frac{P_s}{P_{av}} \qquad (4.7)$$

which compares the available power into 50Ω, P_{av}, to the power dissipated in Z_s, P_s.

4.3.2. Simulated Results

This discussion is limited to four structures that are of immediate
interest:

(i)	$LiNbO_3$-Varnish-SiO_2	:	Figure 4.6.
(ii)	$LiNbO_3$-Indium-SiO_2	:	Figure 4.7.
(iii)	$LiNbO_3$-Indium-Al_2O_3	:	Figure 4.8.
(iv)	ZnO-AuCr-Al_2O_3	:	Figure 3.9.

The transducers being air backed for all cases. For each case, two
plots are presented:

(a)   The surface of insertion loss is plotted - as a function of
normalised frequency, ω/ω_o, and normalised bond thickness,
$\ell_b \omega_o / 2\pi v_b$.

(b)   The insertion loss as a function of frequency for a *typical*
bond thickness for a particular frequency of operation.

It is seen, for case (i), that the impedance of the bonding layer is
much lower than the impedance of the transducer and the substrate.
The thickness of the bond plays an important role in the frequency
characteristics of the transducer. -For maximum bandwidth, a very
thin bonding layer is required.

X10 Insertion Loss (dB)

Normalised Frequency

Normalised Bond Thickness

X0.1

(a)

Insertion Loss (dB)

Frequency (MHz)

(b)
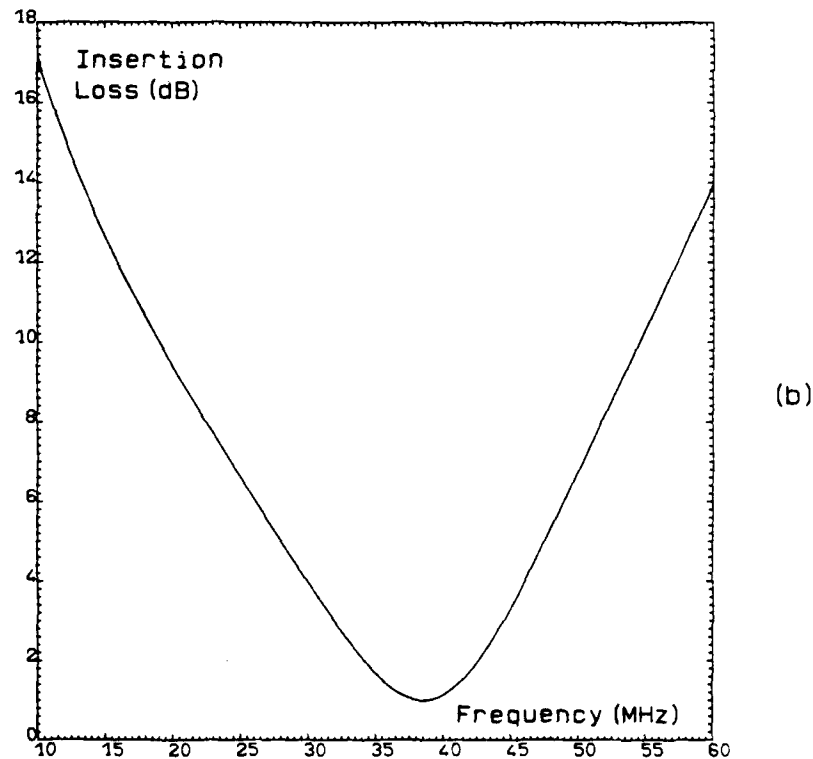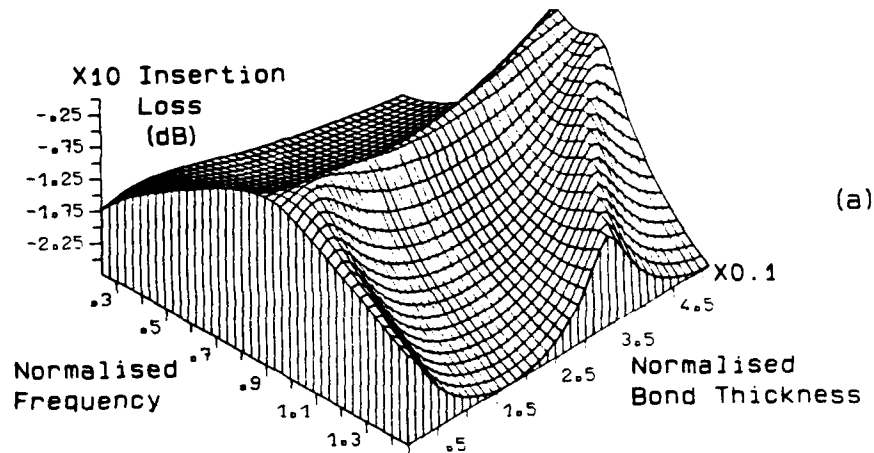
Figure 4.6: Insertion loss for $LiNbO_3$-varnish-SiO_2 transducer structure. d:87.5μm; r:2 mm; t:35.0; Z_t:32.9 Mrayl; v_t:7.0 Kms^{-1}; Z_b:2.64 Mrayl; v_b:2.4 Kms^{-1}; k_t:0.5; Z_s:13.1; Z_B:4.15x10^{-4}, and for (b), l_b:0.5μm.
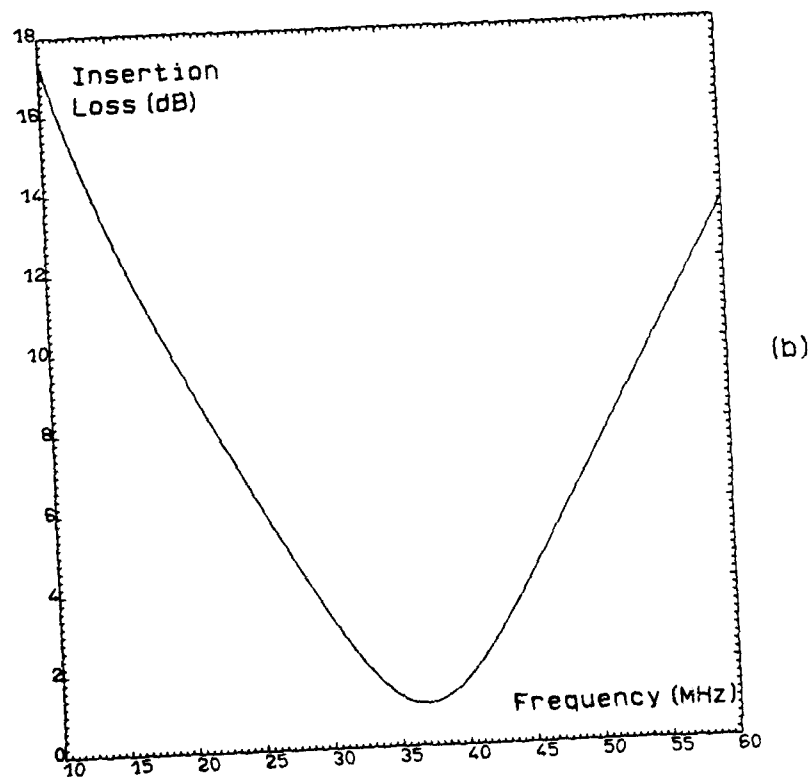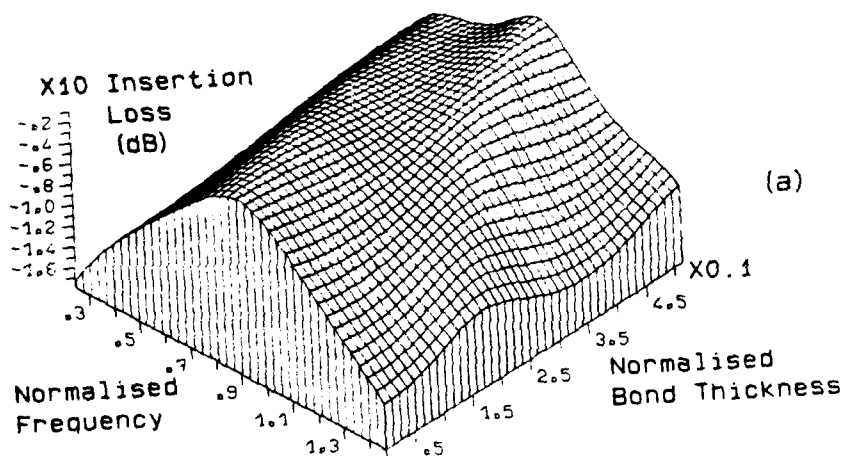
Figure 4.7: Insertion loss for $LiNbO_3$-Indium-SiO_2 transducer structure. d:87.5μm; r:2 mm; t:35.0; Z_{t_1}:32.9 Mrayl; v_t:7.0 Kms^{-1}; Z_b:18.7 Mrayl; v_b:2.56 Kms^{-1}; k_t:0.5; Z_s:13.1; Z_B:4.15x10^{-4}, and for (b) ℓ_b:0.5μm.

(a)

(b)
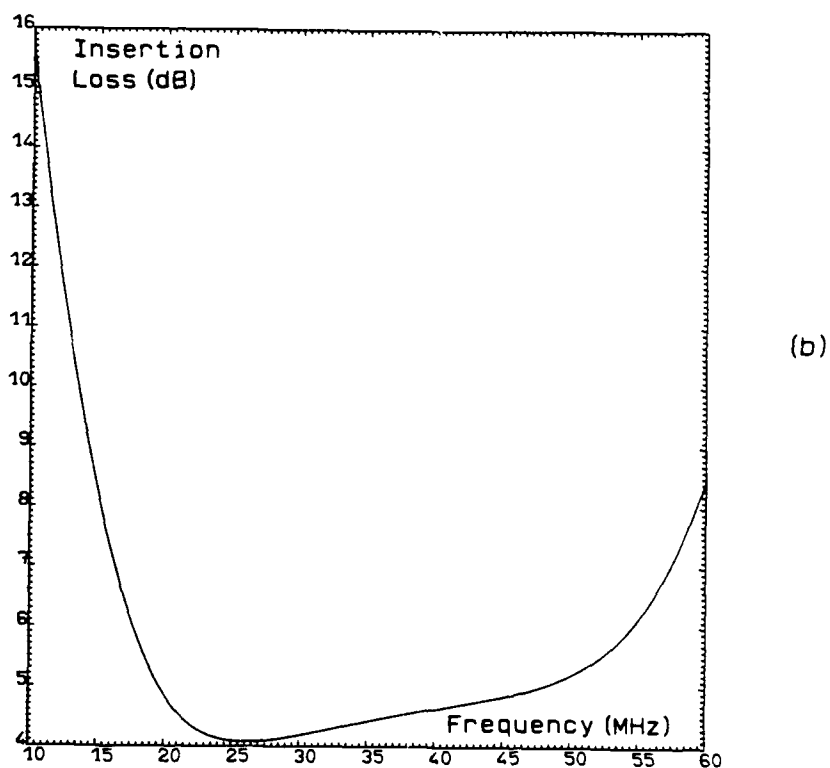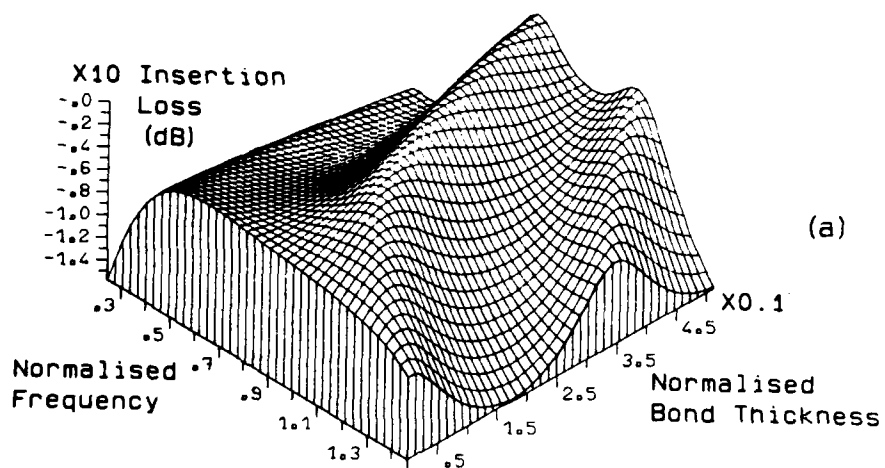
Figure 4.8:   Insertion loss for LiNbO$_3$-Indium-Al$_2$O$_3$ transducer
structure.   d:87.5μm;   r:2 mm;   t:35.0;   Z$_t$:32.9 Mrayl;
v$_t$:7.0 Kms^{-1};   Z$_b$:18.7 Mrayl;   v$_b$:2.56 Kms^{-1};   k$_t$:0.5;
Z$_s$:44.0;   Z$_B$:4.15x10^{-4}, and for (b) ℓ_b:0.5μm.
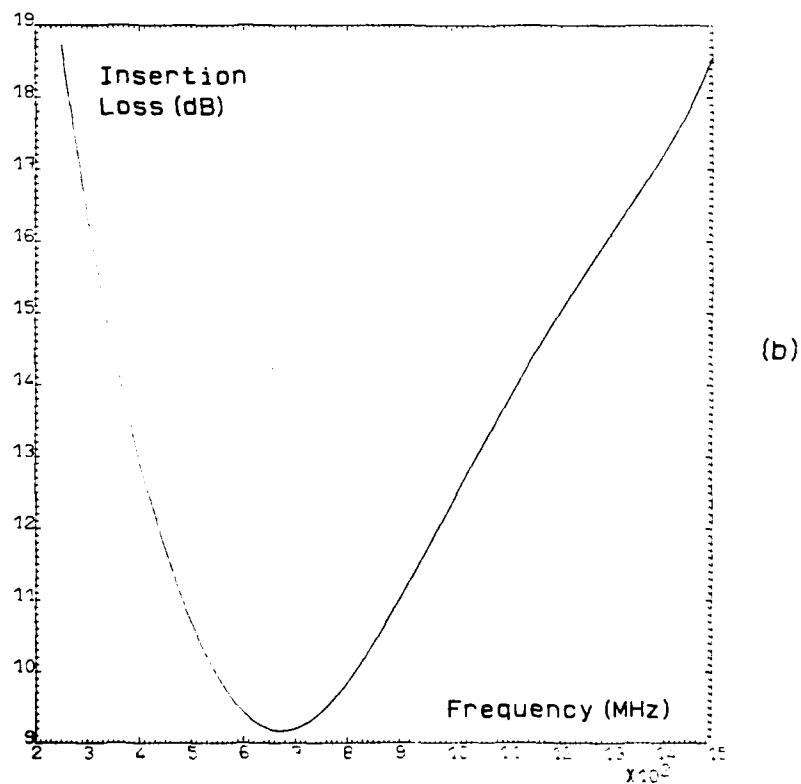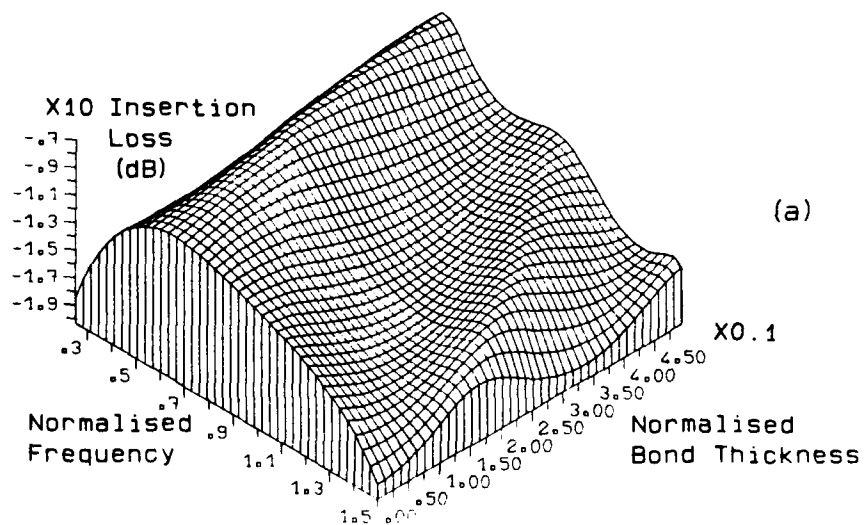
Figure 4.9: Insertion loss for ZnO–AuCr–Al$_2$O$_3$ transducer structure.
d:3.2μm; r:400μm; t:8.0; Z$_t$:36.0 Mrayl; v$_t$:6.4 Kms^{-1}; Z$_b$:62.5 Mrayl; v$_b$:3.24 Kms^{-1}; k$_t$:0.25; Z$_s$:44.0; Z$_B$:4.15x10^{-4} and for (b) ℓ$_b$:0.2μm.

95.

For case (ii), where the impedance of the bonding layer is comparable to those of the transducer and the substrate, the thickness of the bond is not very critical.

For case (iii), it is seen that up to a bonding layer less than $\lambda/4$, there is a broadband response.

Case (iv) is an almost universal transducer structure for frequencies above 250 MHz. In practice, the transducer is sputtered on the substrate which is coated with CrAu (which forms one of the electrodes of the transducer). Therefore, in this case, the thickness of the gold film is taken to be that of the bonding layer.

4.3.3.   Bonding with Low Impedance Varnish

From the computer simulation, it is seen that, in general, for an air backed transducer, with no electrical matching network, the closer the impedanc looking into the substrate to the impedance of the transducer, the broader the bandwidth. Figure 4.6. shows that, for a low impedance bond (i.e. varnish), it is essential to use a very thin bonding layer.

For 40 MHz operation, a GE varnish (#7031), thinned in a 50:50 alc ohol-toluene mixture for bonding the transducers has been used. The achievement of a thin bond (less than 1µm) relies on spinning the substrate and thinned varnish (at about 3000 rpm for less than 5 s), followed by bonding and baking (for about one hour at 110°C). With

END
DATE
FILMED
1 84
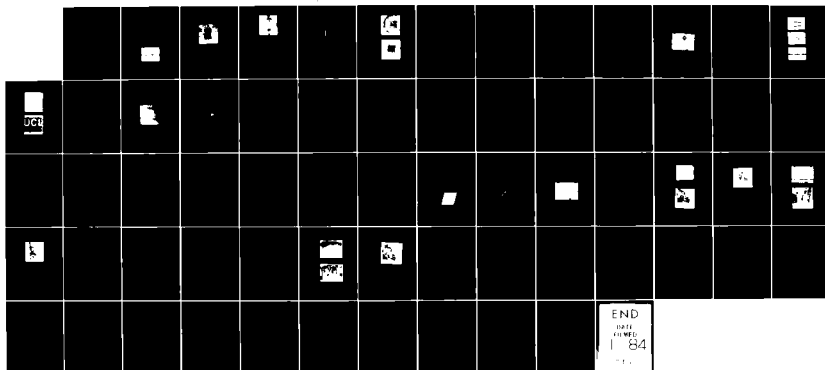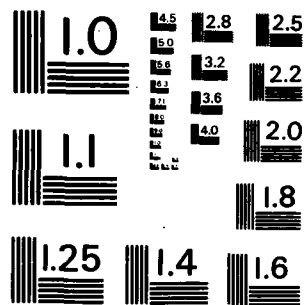
MICROCOPY RESOLUTION TEST CHART

NATIONAL BUREAU OF STANDARDS-1963-A

this rather primitive technology, it has been found possible and repeatable to obtain a 3 dB fractional bandwidth of 40% at 40 MHz which would allow the transmission of a 63 ns pulse - making time gated imaging through a minimum thickness of about 200μm possible, (for a solid with typical velocity in the range 5000 - 6000 m/s).

4.4.   Results on Subsurface Imaging with Narrow RF Pulses.

A test sample was imaged which was fabricated from two 0.8 mm (5λ at 40 MHz) solder-coated steel plates. Some letters were inscribed on one of the plates and they were then put face to face and bonded. Through a hole which was subsequently drilled in the centre of the plate, some more solder was injected between the two plates. Figure 4.10 shows the echoes from the different planes of the object.
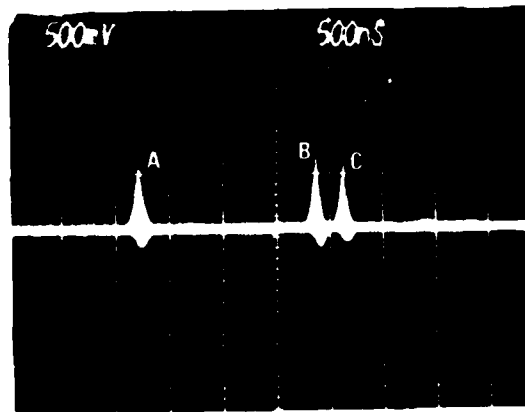
Figure 4.10:   Echoes from different planes of the steel bond.

　　　　　　　(A) is a spurious reflection from the surface of the lens.

　　　　　　　(B) and (C) are reflections from the surface of the sample and the bond respectively.

97.

It is seen that the pulse is sufficiently narrow to eliminate the
surface reflection from the "object" reflection by suitable time
gating. A micrograph of this structure is shown in Figure 4.11.
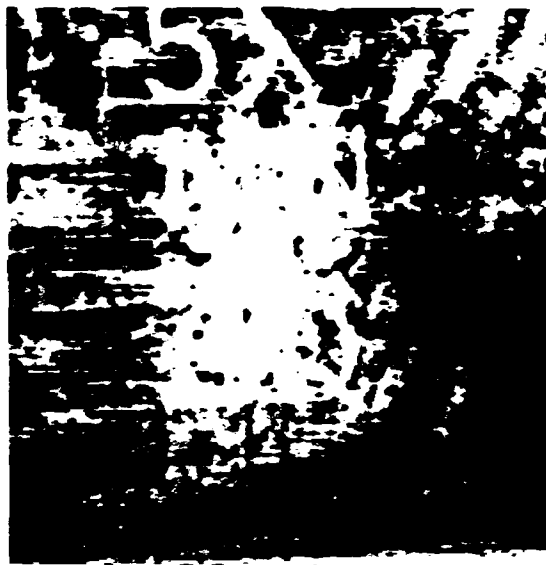
Figure 4.11:   A micrograph of the steel plate solder bond. Field
                of view: 15 mm square.

The letters can clearly be resolved. More importantly, a white patch
in the vicinity of the hole at the centre of the structure can be
seen. This is due to low reflectivity in this region (the contrast
is reversed), indicative of good bonding due to excess solder.

The second test object imaged consisted of a glass microscope slide
with CrAu (thickness of 4000 $\mathring{A}$) - in the shape of an electron micro-
scope finder grid - deposited on it. Figure 4.12 shows a micrograph
of this structure, imaged through the glass slide.
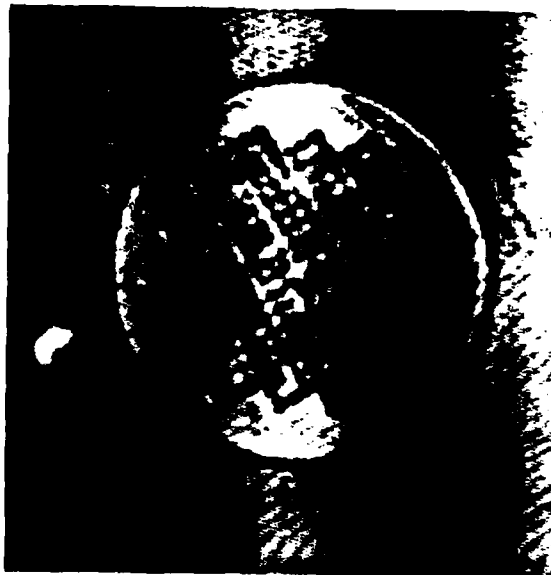
Figure 4.12: CrAu pattern deposited on a glass slide, imaged through the slide. Field of view: 4.5 mm square.

The grid pattern can be clearly visualised. In this structure, the squares are grouped together. Each group consists of six squares, (the length of the group is 367μm and its width is 242μm), separated by an 18 m gold bar. The groups are clearly resolved. Further, some structures – of the squares – within the groups can be seen. The wavelength in glass at 40 MHz is 125μm. It is felt that this experiment is of value, insofar as the subsurface resolution is concerned.

This experiment was followed by the non-destructive examination of transistor:header bonds. The transistors examined (TIP33A) were NPN, audio frequency power transistors. As shown in Figure 4.13, in this structure the silicon chip is bonded to a nickel plated copper header.

TRANSISTOR
CHIP

PLASTIC
PACKAGE

COPPER
HEADER

ACOUSTIC
ENERGY
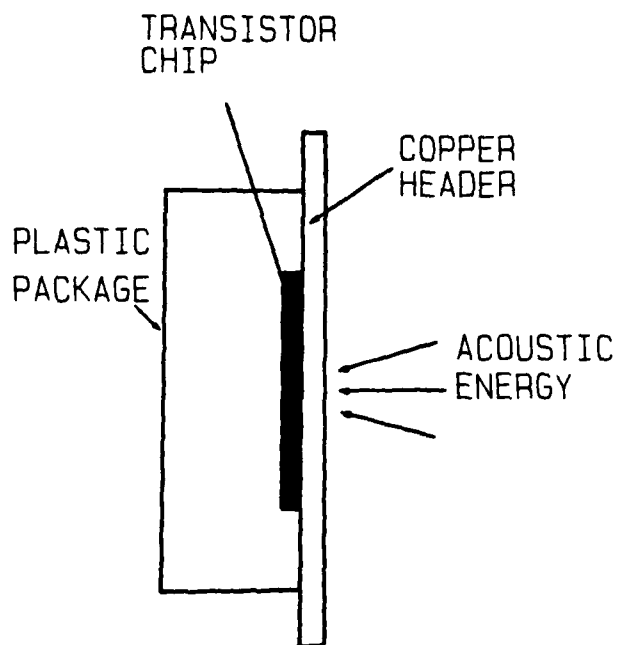
Figure 4.13:   Schematic diagram of TIP33A plastic packaged power

transistor.

The quality of the bond has major effects on the thermal impedance
of the device. The bond was imaged through the copper header, without
any prior preparation. Figures 4.14 (a) and (b) show two micrographs
of two different specimens.

The non-uniformities in the bonding of each transistor can clearly be
seen. The main source of non-uniformity in such a structure is voids
- in particular, hydrogen voids formed during the fabrication of the
transistor, (Hipwood, 1982). It is also clear that the bond of the
transistor in (b) is more uniform.
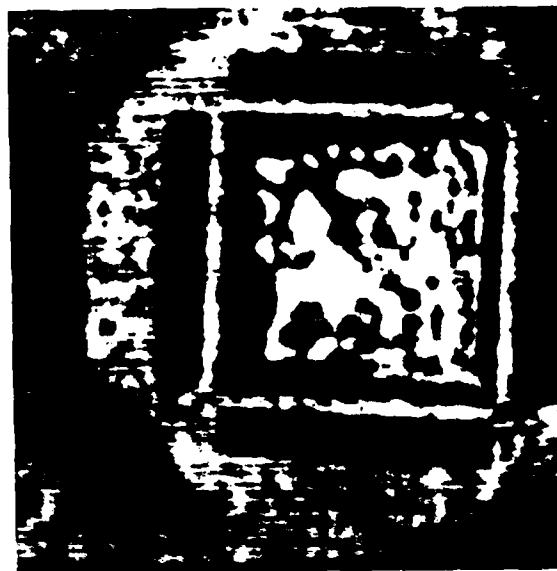
(a)
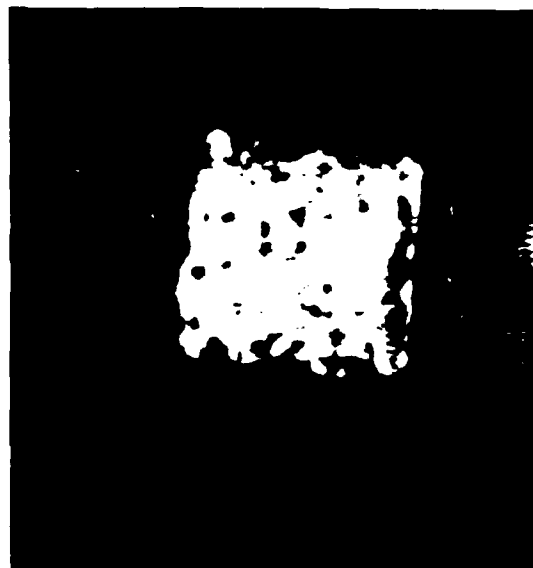
(b)

Figure 4.14:   (a) and (b). Micrographs of two different transistor

bonds taken at 40 MHz. Field of view: 6 mm square.

4.5.   Discussion and Conclusion.

A design procedure for reduced aperture lenses has been presented.
It has been shown that suitably designed spherical lenses can give
essentially diffraction limited focussing in solids, over a substantial
range of focussing, in a wide range of materials with differing
velocities. The key problem frequently encountered is the need to
examine the planes very close to the surface of a solid - leading to
the need for a broadband transducer. A number of computer simulations
have been presented and a method of bonding low frequency transducers
- for maximum bandwidth operation - has been discussed.

The computer simulation shows that a $LiNbO_3$-Indium-Al_2O_3 is particularly
attractive for maximum bandwidth operation. Indium bonding is a known
thermocompression technique for bonding ultrasonic transducers, (Attal,
1981). The computer simulation shows that this structure competes
well with the more universal ZnO-CrAu-Al_2O_3 structure for high freq-
uency operations. It is also evident that, with low impedance varnish
bonding, it is essential to use the thinnest possible bonding layer.

We have shown that it is possible to eliminate the front-face echo
by large bandwidth operation, as clearly demonstrated by the results
obtained from test samples. It is believed that time-gated imaging
with reduced aperture lenses provides the means for subsurface imaging
of a wide range of samples. Imaging transistor:header bonds of power
transistors is amongst the examples.

102.

CHAPTER 5

PULSE COMPRESSION ACOUSTIC MICROSCOPY

5.1.   Introduction

In Chapter 4, it was shown that when imaging the subsurface planes of
a solid, by employing narrow pulses the surface echo and image echo
can be separated. In striving for ever shorter pulses to allow
examination of defects closer to the surface, the dilemma so well
known in radar is encountered: Having achieved the requisite short
pulses, one finds that they contain all too little energy - leading to
a reduced detection sensitivity. The situation can be greatly improved
by resorting to long FM pulses. We have recently shown that a chirped
system, centered on 60 MHz, implemented using SAW filters, can give
significant improvement in the imaging of subsurface objects, (Yue et
al, 1982; Nikoonahad et al, 1982).

A detailed discussion of the applications of SAW devices for signal
processing can be found elsewhere, (Gerard, 1977; Ash, 1978). The
expander converts a baseband pulse to a *long* chirp pulse. At the
receiver side, another SAW dispersive delay line compresses the long
chirps reflected from different planes of the object to *narrow* pulses
centered on a high frequency carrier, Figure 5.1.
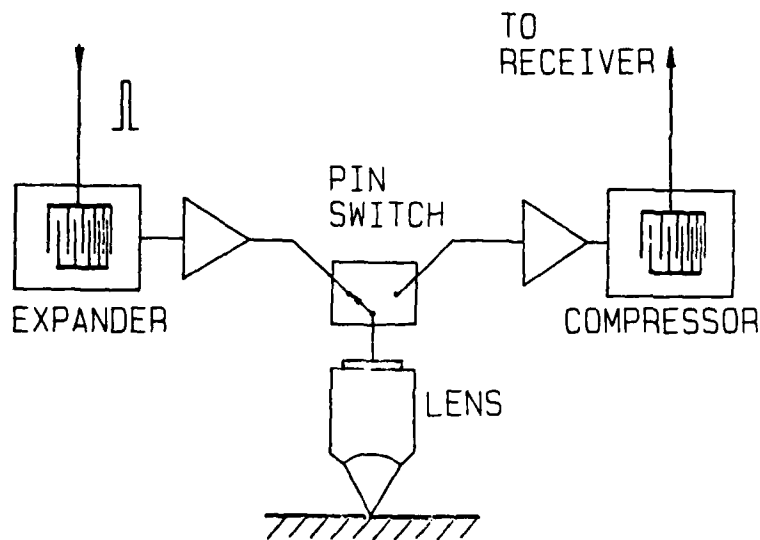
Figure 5.1:   The pulse compression reflection acoustic microscope.

For the simple case of a compressor:expander pair (when the microscope
is absent), the frequency of the carrier is the centre frequency of the
SAW filters. With the microscope present, however, the viscoelastic
losses in water result in a square law dependence of the attenuation
on the frequency, (Kinsler and Frey, 1962). As the expanded pulse
propagates through the water, this f^2 dependence imposes a semi-Gaussian
taper on the amplitude spectrum of the chirp. At low frequencies, the
differential loss in the liquid is small; the pulse compression micro-
scope is then, in many ways, similar to a chirped pulse radar. At high
frequencies, however, the differential loss can amount to many tens of
dBs.

It is important, therefore, to discover whether, despite such high losses, one can still gain an advantage by the use of pulse compression at high frequencies. It is at once clear that, starting with a constant amplitude chirp, the "centre of gravity" of the pulse will shift in a downward direction as a result of the differential loss, which favours the low frequencies. It is essential, therefore, to take the resulting reduction in the resolution into account, when assessing the merits of an overall system.

In this Chapter, a pulse compression reflection acoustic microscope working at 60 MHz is described. Results demonstrating the advantages of such a system over a conventional RF system are presented. A theoretical model of the pulse compression microscope is presented. Computer and analytical results of the effect of the dispersive attenuation on the compressed pulse shape and the processing gain are presented.

5.2.   Experiments at 60 MHz.

The basic 60 MHz pulse compression system is shown in Figure 5.1. The expander is excited with a narrow video pulse (10 V, 13 ns duration). The output of the expander comprises a chirp pulse centered on 60 MHz with 25 MHz bandwidth and a duration of 2.2 µs. The expanded pulse - after suitable amplification and time gating - is applied to the transducer. The receiver consists of a low noise amplifier, followed by the compression filter. The returns from different object reflectors

are compressed, the mainlobe width being 50 ns, and sidelobe levels
at -32 dB. The compressed pulse is detected, amplified and displayed
in the conventional manner. The lens used in this experiment had an
A/R of 0.4, as discussed in Chapter 4.

Full length (i.e. 2.2μs) chirps reflected from the front face of the
lens have been observed, Figure 5.2.
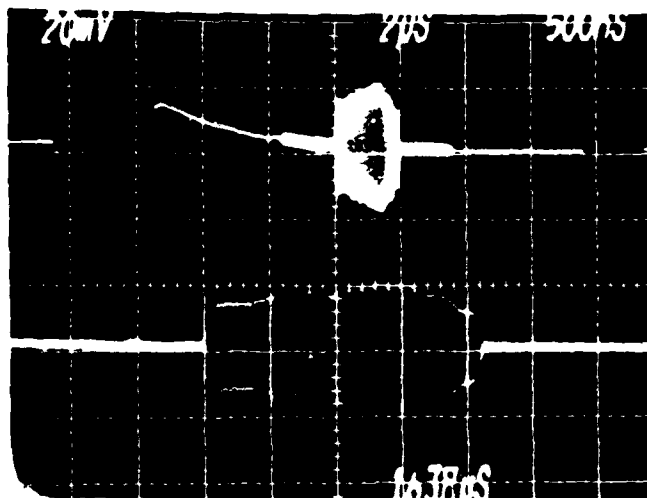
Figure 5.2:   The input chirp and the reflection from the front face
               of the lens. The bottom trace illustrates the front
               face reflection on a faster sweep.

This is a good indication that the transducer had enough bandwidth to
transmit the entire chirp. Also, the measured processing gain, 17 dB,
is in good agreement with the filter specification.

5.2.1. Range Resolution Test

The transducer bandwidth determines the range resolution of the
microscope. It is, therefore, important to appreciate that pulse
compression techniques do not improve the range resolution of the
system. To demonstrate the range resolution capability of the pulse
compression system, a glass microscope slide was used as a test
sample. Figure 5.3 (a) shows the 2.2μs chirp pulse. Figure 5.3 (b)
shows two uncompressed chirps reflected from two sides of the solid;
the time for double transit through the slide is 400 ns, as comp :!
with the length of the chirp which is 2.2μs. There is naturally
interference between the front-surface and the rear-surface ech'
However, once the signal is compressed, the two signals can clea ,
be resolved, Figure 5.3 (c).

5.2.2. Detection Sensitivity Tests

To demonstrate the principle of the technique, a test sample was
devised, consisting of a dural plate of thickness of 0.8 mm, having
three letters inscribed on one face. The width of the letters was
0.3 mm and the depth of inscription 0.2 mm. The letters were then
imaged, from the smooth side - that is, going through the thickness
of the plate - using conventional 50 ns RF pulses. Owing to the
reflection loss at the smooth surface interface to the water, as well
as the material's propagation loss, the imaging signal was only
barely adequate to reveal the letters, Figure 5.4 (a). Using the
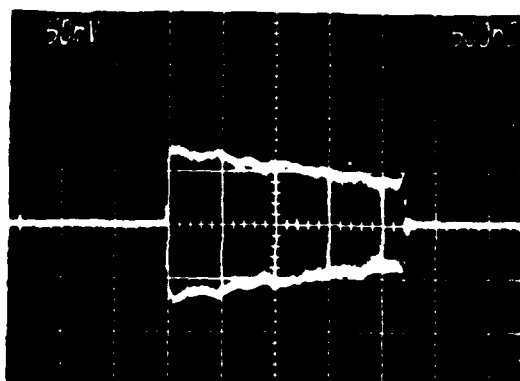
(a)
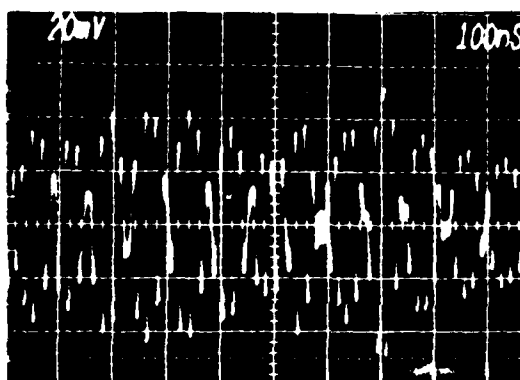
(b)
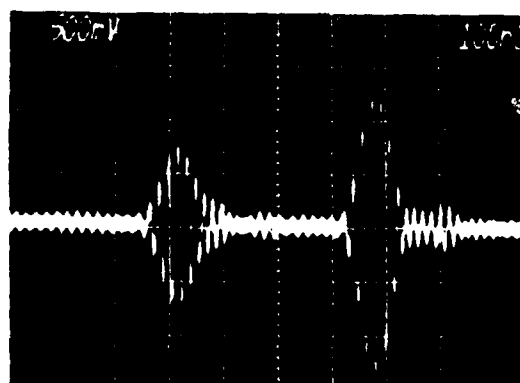
(c)

Figure 5.3: (a) Input chirp pulse to the transducer

(b) Two uncompressed pulses, reflected from two sides of
a microscope slide.

(c) As (b) but compressed.
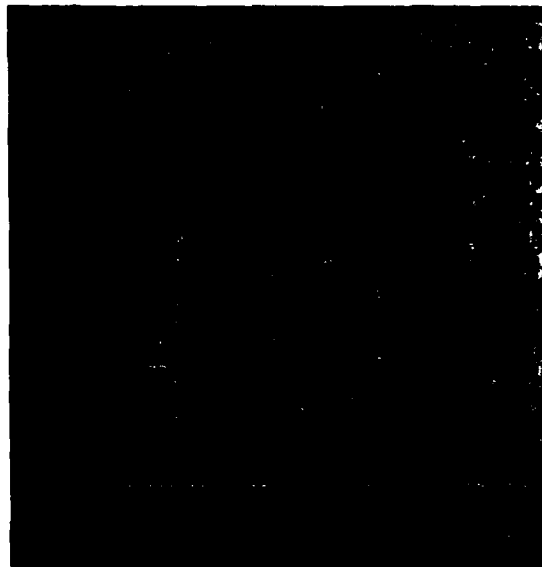
(a)

(b)

Figure 5.4:   Letters imaged through 0.8 mm thick dural plate, (a)
with narrow RF pulses and (b) with long coded pulses,
for the same transducer voltage. Field of view: 7.5x7.5 mm.

pulse compression system described above, *with the same pulse amplitude*, the greatly clarified image, shown in Figure 5.4 (b), was obtained.

The second test sample examined consisted of 2000 $\overset{\circ}{A}$ of CrAu - in the form of triangular fingers - evaporated on a glass microscope slide. The objective was to image the pattern by going through the glass. For plane wave incidence, the reflectivity between glass and water is 81%. With 2000 $\overset{\circ}{A}$ of Au (neglecting the thickness of the Cr, since normally a flash of Cr is used), the reflectivity is increased by 2×10^{-3}. This would require a S/N ratio of better than 26 dB for imaging. With an RF set-up with 16 dB of S/N ratio, (the S/N ratio measured, in a bandwidth of 60 MHz, for the signal focussed at the rear-surface of the slide), the pattern could not be imaged. In this experiment, the maximum available RF power was used. However, with the pulse compression microscope, owing to the extra 17 dB of processing gain, the pattern could be imaged, Figure 5.5.

The maximum pulse amplitude which can be utilised is determined by the transducer breakdown. The two experiments here described demonstrate that the pulse compression technique provides a very real performance advantage.

5.3. Theoretical Analysis

The microscope, together with the expander:compressor pair, can be thought of as a two port network, as shown in Figure 5.6.

Figure 5.5: Pattern consisting of 2000 Å of gold deposited on a glass
             microscope slide, imaged through the slide, with the
             pulse compression microscope. Field of view: 7.5x7.5 mm.
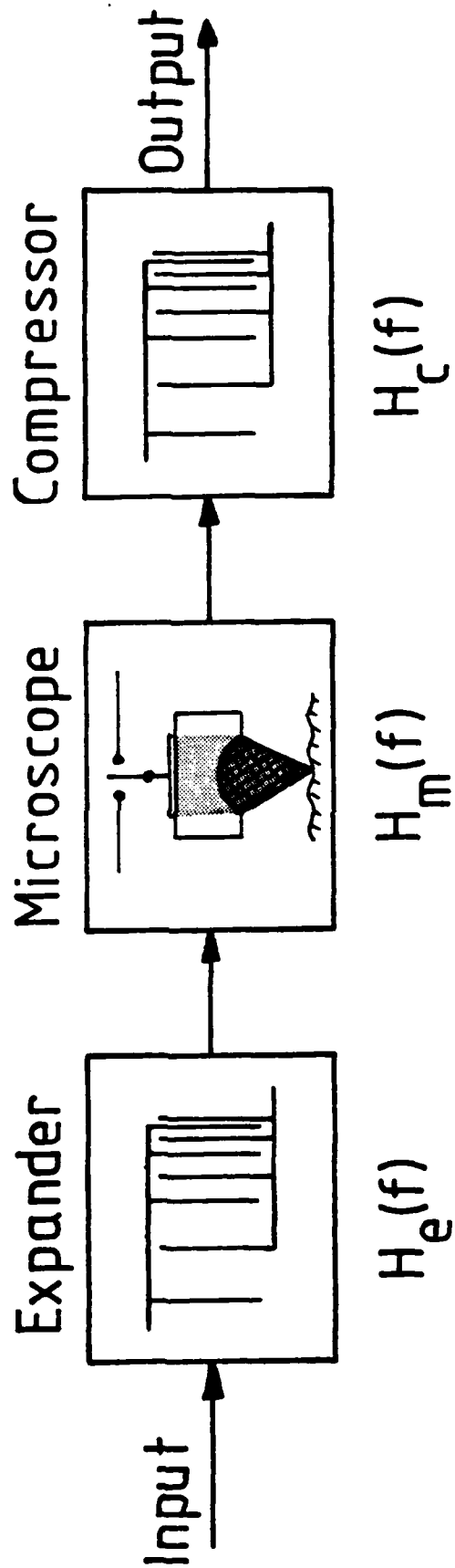
Figure 5.6: The pulse compression microscope as a two port network.

For an impulse excitation, the output of an unweighted expander comprises of a linear FM Rectangular chirp pulse with a bandwidth of B and a duration of T. This function has a quadratic phase variation in time, and can be written in the form:

$$h_e(t) = rect(\frac{t}{T})\cos(2\pi f_o t + \tfrac{1}{2}\mu t^2) \qquad (5.1)$$

where f_o is the centre frequency of the filter and,

$$\mu = B/T \qquad (5.2)$$

The rect function is defined as:

$$rect(t/T) \equiv \begin{cases} 1 \text{ for } |t| \leq \dfrac{T}{2} \\[2mm] 0 \text{ for } |t| > \dfrac{T}{2} \end{cases} \qquad (5.3)$$

If $h_e(t)$ is the impulse response for the filter in time domain, the transfer function of the filter, in frequency domain, $H_e(f)$, is given by the Fourier transform of $h_e(t)$. $H_e(f)$ contains terms with Fresnel integrals, which do not represent a closed form solution, (Cook, 1960). However, for large values of time-bandwidth product, (i.e. TB>50), the amplitude spectrum takes the form of the envelope of the chirp pulse and the phase spectrum takes a quadratic form, (Klauder et al, 1960). This is a good approximation, since in most practical situations, TB is large. Therefore, for the chirp given in Equation (5.1), we have:

113.

$$H_e(f) = \sqrt{\frac{T}{B}} \, e^{+j\pi(f-f_o)^2/\mu} \tag{5.4}$$

$H_m(f)$ is defined as the frequency response of the microscope itself.
It can, in principle, include frequency characteristics and phase
nonlinearity of the transducer, dispersion characteristics of all the
propagating media and, finally, the attenuation characteristics of
the water cell. For the present study, only the effect of the frequency
dependent liquid attenuation has been investigated. For most classical
liquids, the f^2 dependence of the attenuation coefficient is given by:

$$\frac{\alpha}{f^2} = c \tag{5.5}$$

where α is the attenuation coefficient per unit length and c is a
constant, characteristic of the liquid. For water at room temper-
ature, c is 25 $mm^{-1}GHz^{-2}$, (Attal and Quate, 1976). Therefore, for
this simple case, the transfer function of the microscope can be
written as

$$H_m(f) \equiv e^{-cLf^2} \tag{5.6}$$

where L is the total path through the liquid. $H_c(f)$ is the transfer
function of the compressor whose phase function is conjugate of that
of the expander, given by:

$$H_c(f) = e^{-j\pi(f-f_o)^2/\mu} \tag{5.7}$$

114.

Therefore, the output voltage, in time domain, after compression, is given by the real part of g(t), where:

$$g(t) = \int_{-\infty}^{+\infty} H_e(f) H_m(f) H_e(f) e^{-j2\pi ft} df \qquad (5.8)$$

It is known that, neglecting the losses, the processing gain is approximately given by the time-bandwidth product of the filters, (Cook 1960; Klauder, 1960). The semi-Gaussian amplitude taper on the expanded pulse spectrum reduces the bandwidth in frequency domain. One would expect a corresponding reduction in the duration of the chirp in time domain - leading to a reduction in the effective processing gain.

This is indeed what our simulations show. However, the assessment is not entirely straightforward, as a result of the downward shift of the "centre of gravity" of the frequency spectrum of the pulse. An upper limit to the loss of processing gain can be set in a very simple manner. One could - and it is probably desirable so to do - build in an additional weighting into the filters. If both compression and expansion are weighted - on the dB scale - linearly with f, the dispersive attenuation in the coupling liquid can be cancelled. It means, of course, that at the lowest frequency, there is a need to attenuate by an amount equal to the differential loss over the band. If the pair processing gain is G_o, the differential loss over the band is L, and the effective processing gain in the presence of losses is G, then it is seen that as long as:

$$G \equiv G_o - L > 0 \qquad\qquad (5.9)$$

there will be some advantage in the use of a pulse compression scheme. To gain a more quantitative insight, Equation (5.8) needs to be solved – which does not yield a closed form solution.

Let us look for an approximate function for $H_m(f)$ which will make the integral more tractable. A polynomial expansion would probably give the best fit. But, one would need to solve a system of linear equations to find the coefficients. Let us look at an exponential approximation in the form,

$$Ae^{-\gamma f} \qquad\qquad (5.10)$$

With a microscope transfer function of the form given in Equation (5.10), the integral of Equation (5.8) can be carried out analytically. Having accepted this approximation, the next task would be to find A and γ. For this, the semi-Gaussian and the exponential are matched at two points, at the lower point, $(f_o - B/2)$, and at centre frequency, f_o. Therefore, there is simply:

$$\left. \begin{aligned} A &= e^{cLf_o(f_o - B/2)} \\[2em] \gamma &= CL(2f_o - B/2) \end{aligned} \right\} \qquad\qquad (5.11)$$

For the case of large TB, the limits of the integral are simply $f_o - B/2$ to $f_o + B/2$. Also, the phase function of the expander and compressor cancel each other. Thus:

$$g(t) = A\sqrt{\frac{T}{B}} \int_{f_o-B/2}^{f_o+B/2} e^{-\gamma f} e^{-j2\pi ft} df \qquad (5.12)$$

the solution of which is given by:

$$g(t) = \frac{2A\sqrt{T/B}\, e^{-(\gamma f_o + 2\pi j f_o t)}}{(\gamma + 2\pi j t)} \times$$

$$\qquad (5.13)$$

$$\left[\sinh\frac{\gamma B}{2}\cos\pi Bt + j\cosh\frac{\gamma B}{2}\sin\pi Bt\right]$$

The envelope of the power is proportional to $g(t)g^*(t)$, given by:

$$g(t)g^*(t) = \frac{4A^2 T e^{-2\gamma f_o}}{B(\gamma^2 + 4\pi^2 t^2)}\left[\sinh^2\frac{\gamma B}{2} + \sin^2\pi Bt\right] \qquad (5.14)$$

Also, from equation (5.14), a closed form expression for the peak power in the compressed pulse can easily be found, as a function of attenuation:

$$g(0)g^*(0) = TBA^2 e^{-2\gamma f_o}\left[\frac{\sinh(\gamma B/2)}{(\gamma B/2)}\right]^2 \qquad (5.15)$$

where A and γ are given by Equation (5.11). It is clear that g(0)g*(0) embraces two factors: (i) an effective processing gain, resulting from expansion and compression and (ii) an effective attenuation which is the result of events happening in a lossy medium. To assess the performance of the pulse compression, the effective attenuation must be excluded. The question is, "At what frequency should this attenuation be calculated?" Physical intuition suggests that this reference frequency, f_r, would be somewhere between f_o and the lowest frequency, $f_o-B/2$. For the present study, however, the "worst case" approach is adopted: i.e., the lowest frequency is chosen. Therefore, the processing gain, measured in dB, in the presence of losses, can be written as:

$$G(cL) = 10 \log \left[g(0)g^*(0)\right] + 20cL(f_o-B/2)^2 \log_{10} e \qquad (5.16)$$

where g(0)g*(0) is calculated from Equation (5.15).

5.4.   Simulated Results.

The filters here simulated have the following characteristics:

f_o =   750 MHz

B =   500 MHz

T =   500 ns

For this case, the differential loss is 32 dB. Figure 5.7 illustrates

the shape of the compressed pulse, numerically calculated from

Equation (5.8), for different values of cL, measured in $mm^{-1}GHz^{-2}$.
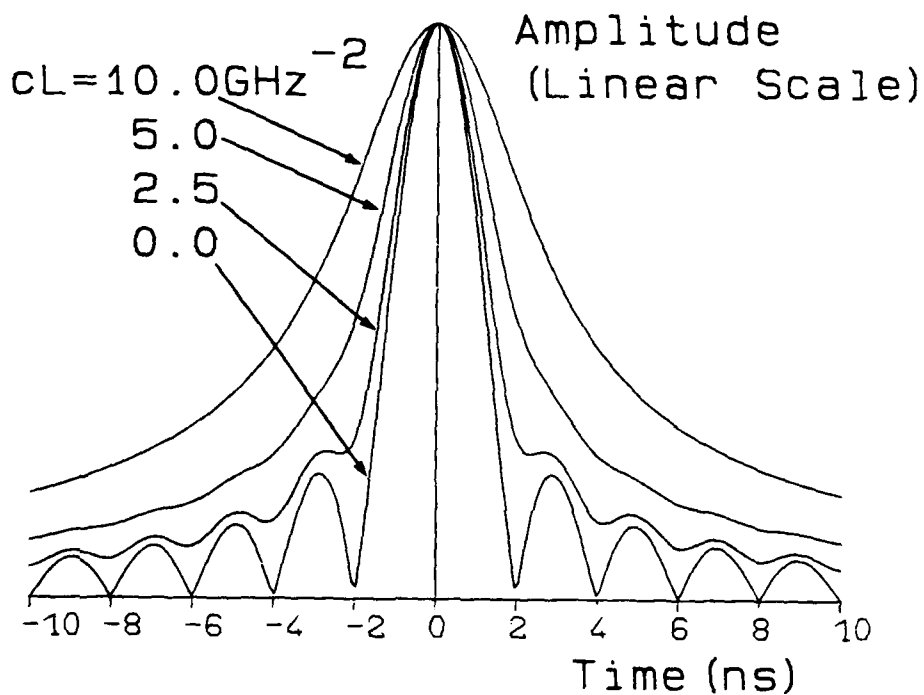
Figure 5.7: The compressed pulse for different degrees of

attenuation.

The exponential approximation of Equation (5.10) can best be

assessed from Figure 5.8.
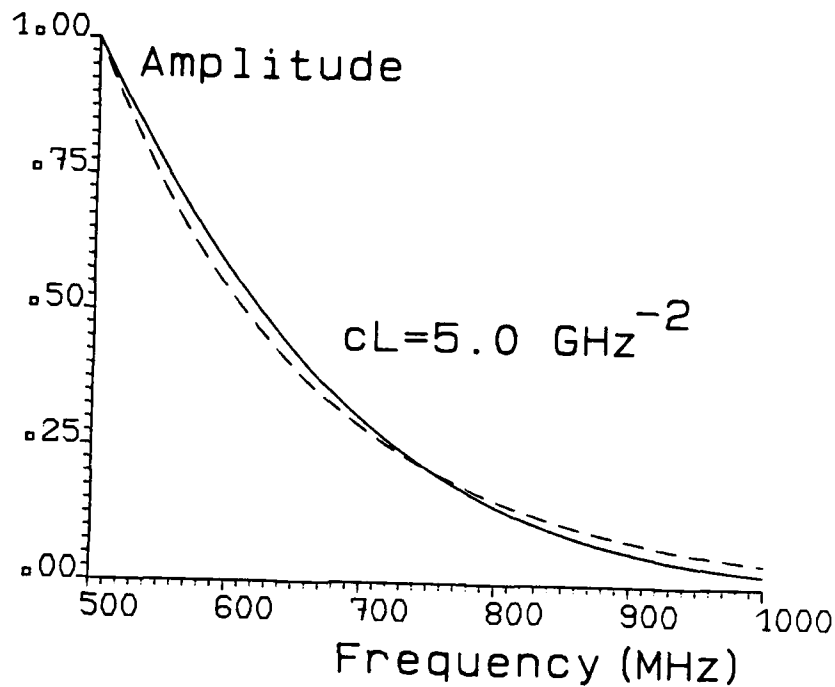
Figure 5.8: The semi-Gaussian (solid line) and approximated exponential (dashed line) taper over 500 MHz passband for a cL of 5.0 GHz^{-2}.

It is seen that, by matching the exponential and the semi-Gaussian at two points, Equation (5.11), the approximation yields a good representation of the transfer function of the microscope over the entire passband. Figures 5.9(a) and (b) illustrate the shape of the compressed pulse, once calculated from Equation (5.8) and once from Equation (5.14), for two values of cL.

120.
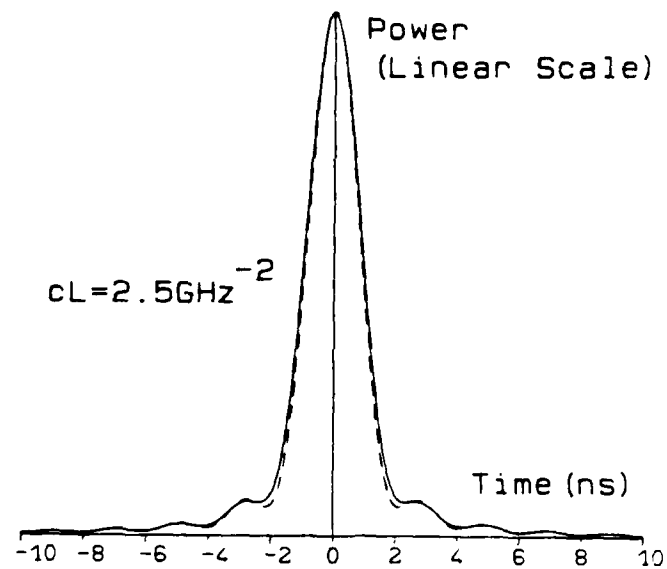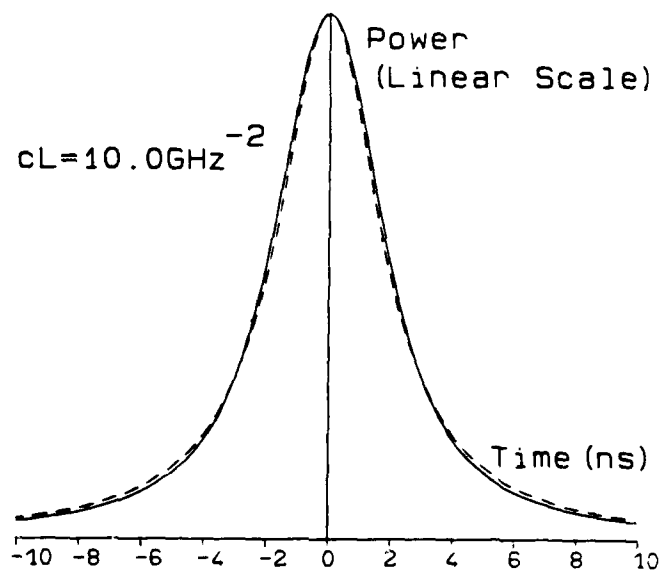
Figure 5.9: The compressed pulse shape. The solid line is obtained from full computer simulation and the dashed line from the exponential approximation for (a) cL=2.5GHz^{-2} and (b) cL=10.0GHz^{-2}

121.

It can be seen that, for the pulse shape, results obtained with the
exponential approximation are in good agreement with the ones
obtained with full numerical calculation.

Figure 5.10 illustrates the variation of the processing gain, G(cL),
with attenuation for two different values of B, 500 MHz and 75 MHz
(corresponding to 10% bandwidth).
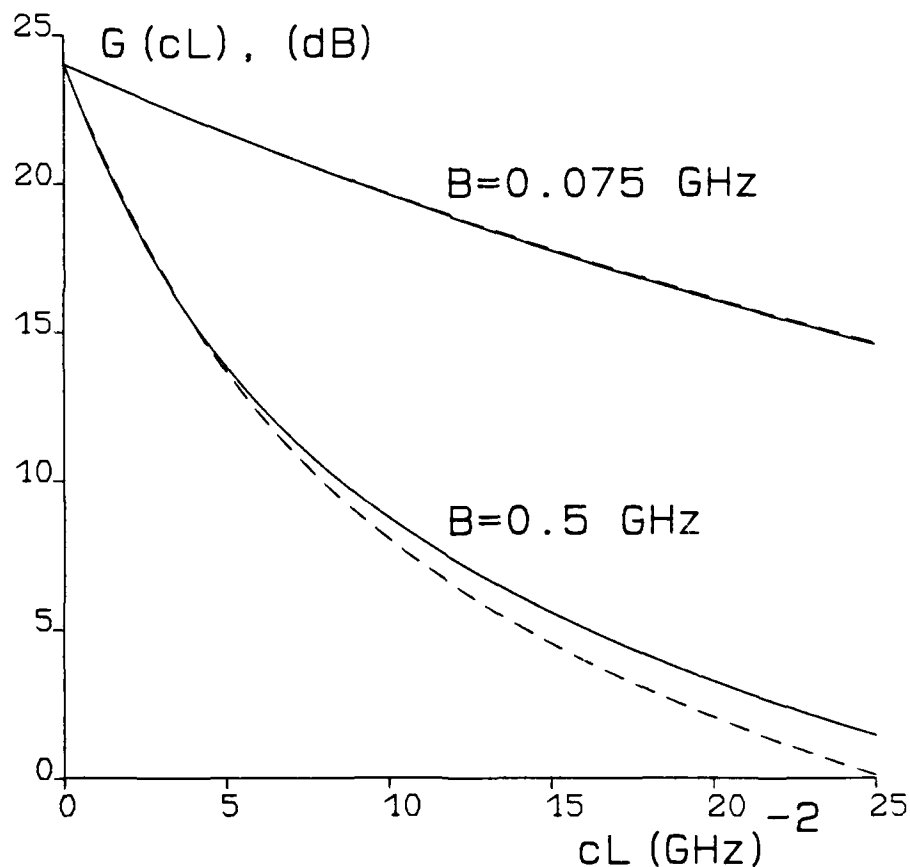
Figure 5.10:   The variation of processing gain, G(cL), with
               attenuation for a filter with f_o=0.75 GHz and
               TB = 250: Exponential approximation (dashed line)
               and full computer simulation (solid line).

122.

Again, it can be seen that the exponential approximation is in good agreement with the full computer simulation. Clearly, for both cases, the processing gain is less than TB. It is also clear that, for the case where B is reduced, the processing gain is higher.

5.5. Discussion and Conclusion

It has been experimentally demonstrated that the pulse compression techniques are directly applicable to acoustic microscopy. It has been shown, in particular, how pulse compression can alleviate a recurring problem - the need to obtain information about weak reflectors situated near the surface of the object, which give rise to strong reflection. The pulse-compression technique, at low frequencies, enables one to obtain an imaging signal which is enhanced by the time-bandwidth of the expanded pulse.

A critical factor in the ability to image with weak signals close to the surface is the need to have very low time-sidelobes in the compressed pulse. In principle, a transducer can be designed to give a certain frequency characteristic, to provide a suitable weighting on the expanded pulse - leading to sidelobe suppression.

The experiments were carried out at a relatively low frequency which is in the range directly applicable to many micro-NDE imaging problems.

An analysis has been presented for the pulse compression microscope. The computer simulation shows that the differential attenuation in the coupling liquid leads to a marked smoothing of the sidelobe structure of the compressed pulse, as well as a wider mainlobe. Further, a simple, though accurate, approximation has been presented which leads to the *analytical* formulation of the expander-microscope-compressor system. The compressed pulse shape results obtained, with the approximation, are in good agreement with the ones obtained with the full computer simulation. We believe that this approximation is of value in gaining an insight into the problem, and primary considerations show that it can be extended to model filters with simple weighting functions.

Also, using the exponential approximation, an analytical expression for the processing gain in the presence of losses has been found. In so doing, the lowest frequency in the spectrum has been used as the reference. From the results presented in Figure 5.10, one can draw a number of conclusions. Pulse compression at high frequencies, in the presence of high differential losses in the coupling fluid, can still be advantageous. The result in Figure 5.10 suggests that, for a filter with f_o = 750 MHz and TB = 250, working over a 500 MHz bandwidth, for a microscope whose water length is 200μm and operating at 25°C, (i.e. cL is 5.0 GHz^{-2}), the effective processing would be 13.6 dB.

It has also been learned that, if - and this in practice demands a less complex transducer technology - one is prepared to work over a smaller bandwidth, where the differential loss is smaller, the reduction in the

124.

processing gain is considerably lower. The result in Figure 5.10

indicates that, for a filter with f_o = 750 MHz, and TB = 250, working

over 10% bandwidth, for a cL of 5.0 GHz^{-2}, the reduction in the

processing gain is only 7.2 dB. It should also be mentioned that

under low bandwidth operation, the reduction in the effective operat-

ing frequency is less. That is, in terms of resolution, the performance

of the microscope would be better as compared with the case of large

bandwidth operation. We conclude, therefore, that, for high frequency

pulse compression microscopy, filters with large T and small B are

particularly attractive. Practical implementation of such systems,

however, remains to be seen.

These results are based on the "worst case" assumption. That is, the

pulse compression microscope has been compared with an RF microscope

working at the frequency of $f_o-B/2$. In practice, f_r will be more than

$f_o-B/2$. Therefore, less reduction in the processing gain is expected.

We could, for example, associate a "centre of gravity" to the atten-

uated spectrum and use this frequency as f_r. This would, probably,

be a good estimation. One could, on the other hand, look at the

carrier frequency of the compressed pulse, and take this as the

frequency reference. Physical intuition suggests that this frequency

would be very close to the frequency of "centre of gravity".

There is no doubt that the point spread function, at the focal plane,

of a pulse compression microscope is different in nature from that of

an RF microscope. It is also clear that, in terms of imaging perform-

ance, there could not exist a single RF signal which could be sub-

stituted for a wide band chirp. Therefore, when comparing a pulse compression microscope with an RF system, the imaging performance requirement should be borne in mind. A consideration of the concept of "centre of gravity" would provide some insight into this issue. For a more thorough understanding, one should seriously consider the imaging performance of the pulse compression system. This would be an interesting topic for theoretical investigation.

CHAPTER 6

CHARACTERISATION OF METALLIC DIFFUSION BONDS

WITH THE PULSE COMPRESSION MICROSCOPE

6.1.   Introduction.

Diffusion bonding is a process for joining two metals, or metal

composites. A bond is effected by heating two smooth surfaces

while they are pressed into intimate contact, (Bartle, 1975).

The resulting metallic interface consists of a relatively good

atomic fit, where the atoms on both sides of the original interface

are in their normal lattice position. A good diffusion bond,

therefore, has little macroscopic deformation at the interface,

(Tylecote, 1967). There are great hopes for this technique to

serve in place of brazing and welding in many applications, (Champion,

1982). Indeed, the diffusion bonding of titanium, in particular,

has been a successful technique for making aircraft parts, (Addison,

1982).

Amongst the many low reflection objects for which pulse compression

reflection acoustic microscopy is suitable, the nondestructive

imaging of metallic diffusion bonds is of considerable interest to

metallurgists. When attempting to image a diffusion bond with a

conventional RF pulsed reflection microscope, in general, it yields

a weak imaging signal, for three reasons:

(i)   The high reflection loss at the interface. The two-
           way reflection loss at water:metal interface can be as
           high as 25 dB.

(ii)   The scattering loss within the metal. It has been
           shown that, for polycrystalline metals, the main source
           of attenuation is the scattering from the grain bound-
           aries, (Auld, 1973). This loss can be large, depending
           on the frequency of operation and the grain size,
           (Tittmann and Ahlberg, 1982).

(iii)   The low reflection coefficient at a good bond. For the
           case of similar metals, the reflection coefficient can
           be very close to zero. Even for dissimilar materials,
           we are concerned with the reflectivity at a metal:
           metal interface which is, in general, low.

For the first time, we have visualised and obtained pulse compression

acoustic micrographs of a number of diffusion bonds, (Yue et al,

1982a; Nikoonahad et al, 1982; Yue et al, 1982b). In this Chapter,

the results obtained are presented. We have carried out a number

of tests, some of which were destructive, to understand the contrast

of the micrographs. We believe that the contrast in the acoustic

micrographs is a good means of evaluating the bond integrity.

6.2.   Micrographs of diffusion bonds.

All the micrographs here presented have been obtained with the
60 MHz pulse compression microscope described in Chapter 5.
We were concerned with diffusion bonds between two hard metal com-
posites, bonded by means of a relatively softer interlayer. The
hard metals were subsequently to be used as cutting tools and, for
this case, diffusion bonding was a means of attaching the hard
metal, (i.e. the cutting tip), to another metallic "substrate"
(Gee, 1982). Results on three structures tested are presented and
the details for each sample are summarised in the following:

Sample (1):   1.2 mm of copper interlayer bonded to a tungsten-
                carbide:cobalt (WCCo) composite, Figure 6.1.

Sample (2):   0.53 mm of copper interlayer bonded to WCCo,
                Figure 6.1.

Sample (3):   Two tungsten-carbide:nickel (WCNi) composites
                bonded with 0.5 mm nickel interlayer, Figure 6.2.

In each case, the side indicated as the smooth surface, was the
entering side for the acoustic radiation. With the presence of
grains in the material, the scattering from the grain boundaries
can form a coherent background noise, the grain noise, (Tittmann and
Ahlberg, 1982), which, in some cases, can be the source of contrast

Tungsten carbide – Cobalt composite

Copper

Smooth surface
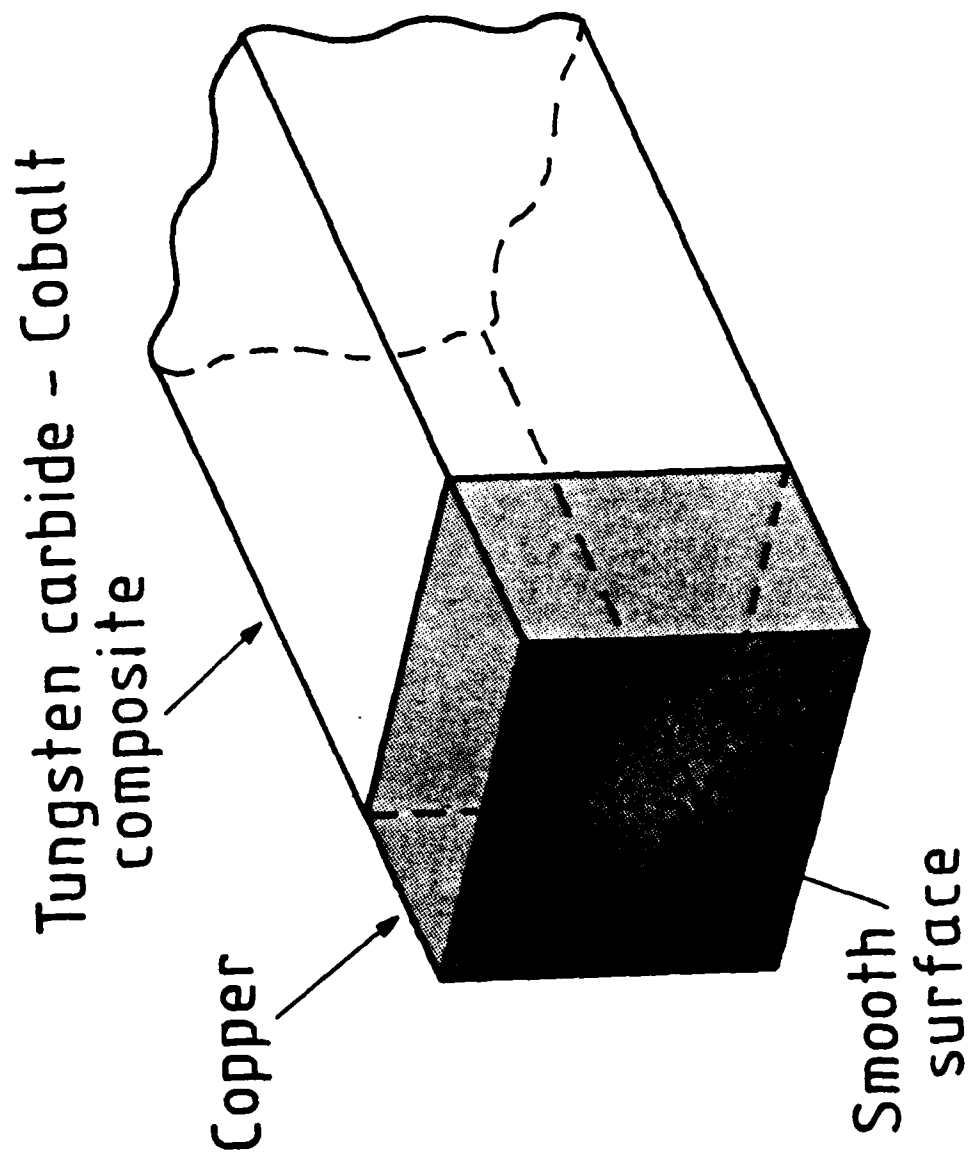
Figure 6.1: The diagramatic representation of the diffusion bond structures of sample (1) and (2); a copper interlayer in WCCo composite.

Ni INTERLAYER

WC–Ni
COMPOSITE

0.8mm

0.5mm

SMOOTH
SURFACE
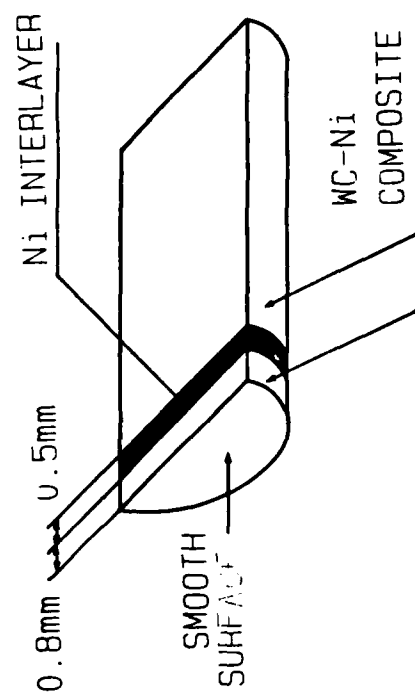
Figure 6.2:   The diagrammatic representation of the structure of sample (3);   two semicylindrical

WCNi composites bonded together by means of an Ni interlayer.

in the acoustic micrograph, (Briggs et al, 1982), when performing

subsurface imaging. With a time gated reflection system, this would

not be a problem however. Figure 6.3 shows the compressed surface

echo and image echo of sample (1), taken directly from the CRO

screen.

Figure 6.3:   Surface and bond echoes from sample (1). The delay

between the echoes corresponds to a double transit

through the 1.2 mm thick copper interlayer.

It is seen that the two echoes can be separated; the delay between

these echoes corresponds to a double transit through 1.2 mm copper

interlayer. Whether the grain noise is present or not, Figure 6.3

is a good indication that the imaging signal is reflected from the bond. Given this, one could, therefore, associate all the image contrast to the bond structure. One could - and this is what we have chosen to do - further substantiate this simple result by time gating and displaying portions of the time signal, other than the bond echo. Three separate regions were gated and displayed and three almost independent micrographs were obtained, Figures 6.4 (a) through 6.4 (c).

Figure 6.4 (a) illustrates an almost uniform cross section of the interlayer; the small dot at the centre of the micrograph is, presumably, a defect within the interlayer. Figure 6.4 (b) has been obtained by detecting and displaying the bond echo and it indicates a high degree of nonuniformity in the bond. Figure 6.4 (c) shows a cross section of the WCCo, 200 ns after the bond echo. It, too, is almost uniform, except indicating a "shadow" of the bond structure. It is clearly demonstrated, therefore, that, by suitable time gating of the compressed pulse, the bond information can be extracted.

Figure 6.5 (a) shows a CRO trace of the compressed echoes obtained from sample (2). Figure 6.5 (b) is a micrograph obtained from this sample. Again, the nonuniformities are clearly evident.
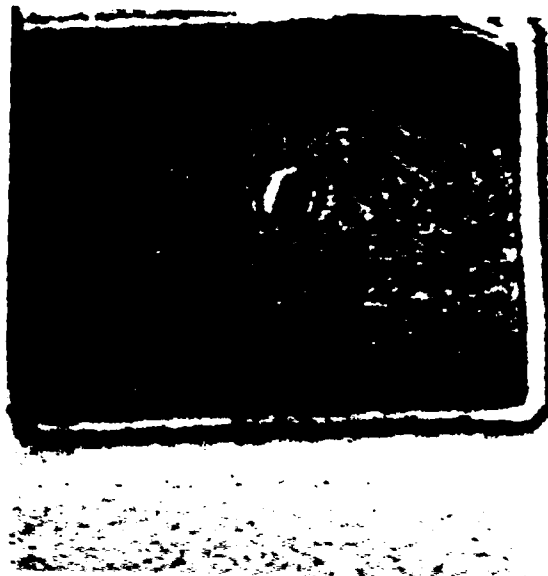
(a)

(b)

Figure 6.4:   Time gated images obtained from sample (1).

    (a)   gating 200 ns before the bond echo

    (b)   gating the bond echo.
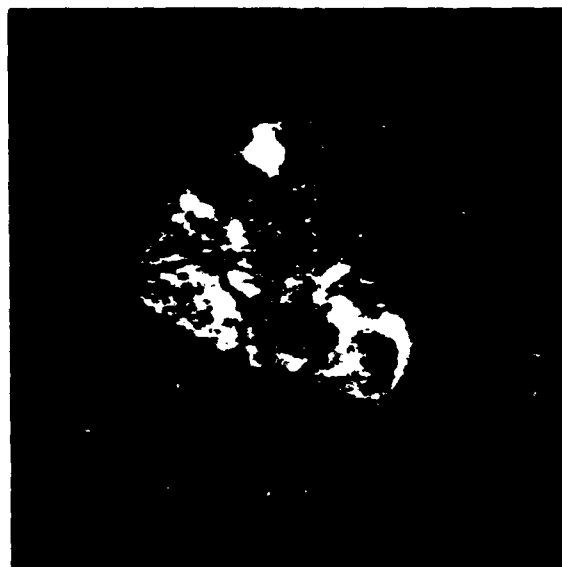
(c)

Figure 6.4:   Time gated image obtained from sample (1).

(c)   gating 200 ns after the bond echo.

Field of view if 6 x 6 mm.
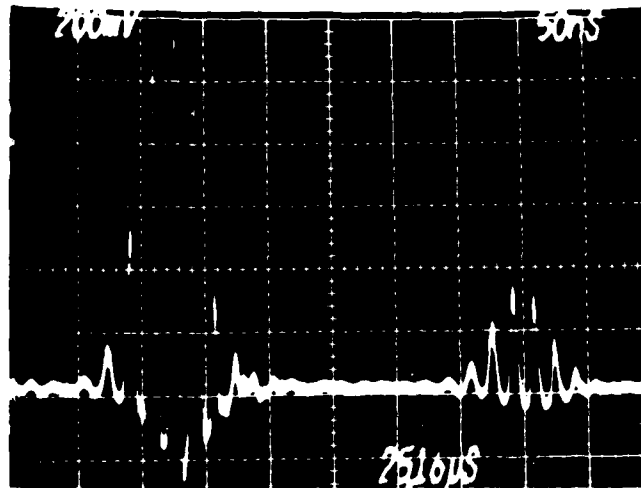
(a)

(b)

Figure 6.5:   Results obtained from sample (2).

        (a) the surface echo and the bond echo

        (b) a micrograph from the bond.

        Field of view is 6 x 6 mm.

Figure 6.6. illustrates a micrograph obtained from sample (3).
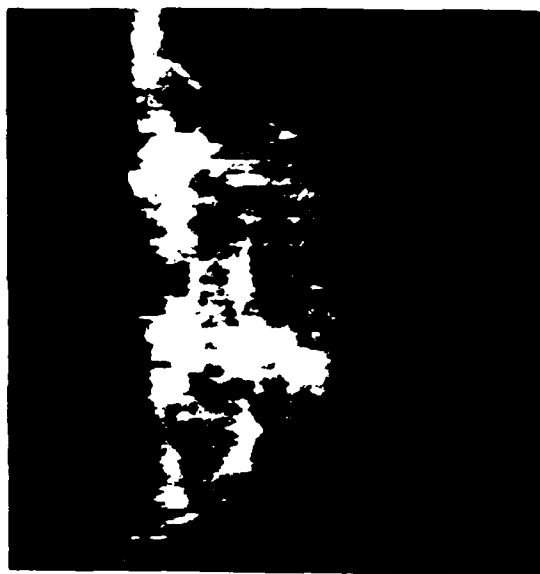
Figure 6.6:   A micrograph obtained from sample (3). Field of
               view is 6 x 6 mm.

6.3.   Interpretation of diffusion bond micrographs.

A number of tests and measurements were carried out to provide an
acceptable interpretation of the diffusion bond micrographs.

6.3.1.   Contrast formation.

When imaging the surface of a solid object, the V(z) effect plays an
important role in determining the contrast of the micrographs, (Atalar
et al, 1977; Weglein, 1978). An interesting observation that we
have made with the pulse compression microscope is that the micro-

graphs are largely devoid of the familiar contrast reversals which take place in varying lens:object distance – the V(z) effect. The reason is that the Rayleigh wave which is largely responsible in the case of surface imaging, (Parmon and Bertoni, 1979), is of course not present. Stonely waves may, or may not, be able to propagate along the interface but are, in any case, less readily excited. Figure 6.7 illustrates the output voltage of the transducer, V, measured and plotted as a function of defocussing distance, z, for both the surface echo and the bond echo, obtained from sample (1).
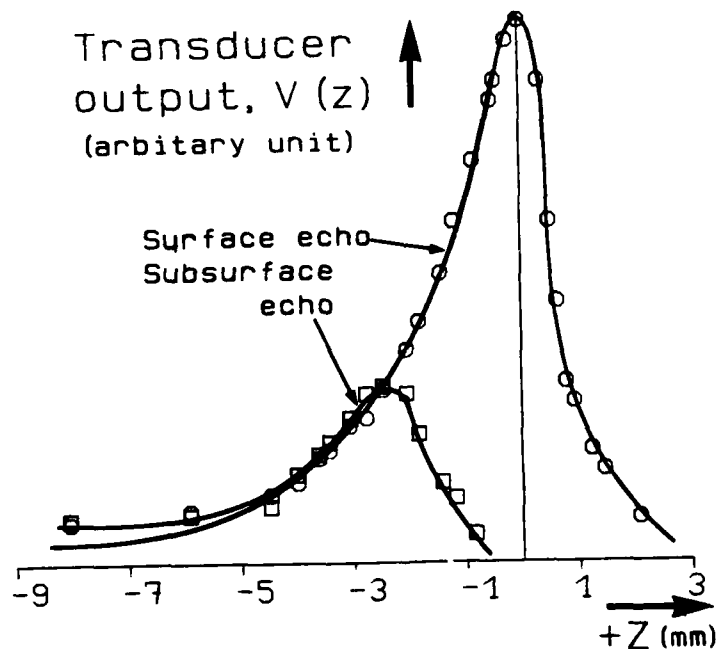
Figure 6.7:   Measured V(z) curves for the surface signal and bond signal.

138.

It is seen that no periodic structure is present for either the surface signal or the bond signal. It is important to note that because a reduced aperture lens is being used, there are no Rayleigh waves excited on the surface of the specimen and, therefore, no $V(z)$ structure is present for the surface signal. As far as the bond signal is concerned, again the variation of the output voltage with z is rather smooth. It would be expected, therefore, that, as a result of preferential defocussing, the image contrast would reduce continuously rather than any contrast reversals to occur.

Figure 6.8 illustrates a subsurface line scan taken across sample (1).

It is clear that no contrast reversals occur - even when the lens is defocussed by a distance as high as $25\lambda_{Cu}$, where λ_{Cu} is the wavelength in copper at 60 MHz.

The slight change in the shape of the line scan is probably due to the fact that the "object" is no longer at focus. At this stage, we conclude that contrast is due purely to change of reflectivity at the bond, rather than any $V(z)$ effect. Therefore, regions of good bonding would correspond to low reflection - leading to dark regions on the micrograph (with no contrast inversion) - and vice versa. This, we believe is of some value for determining the local quality of the bond, nondestructively.
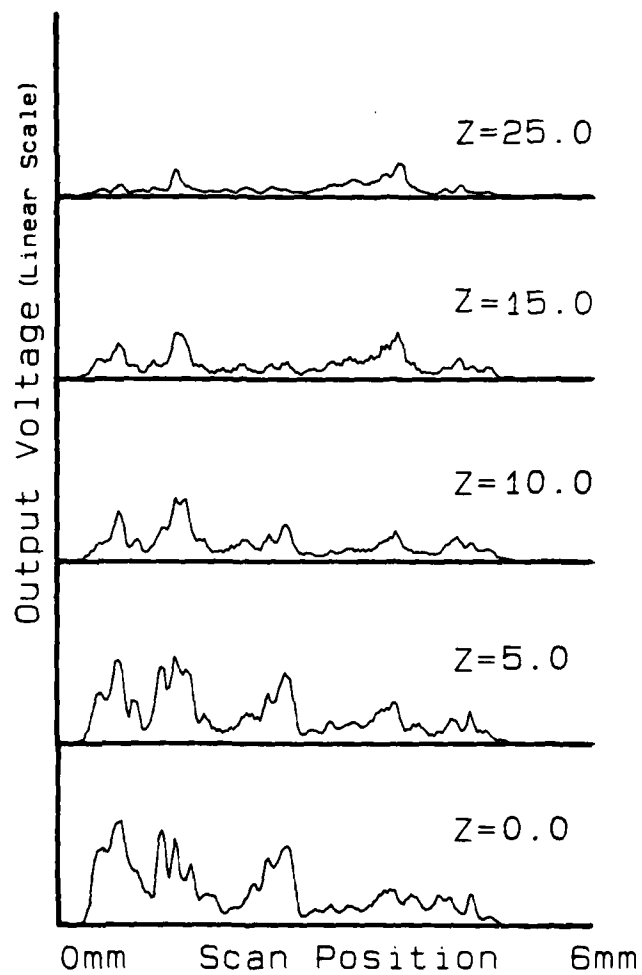
Figure 6.8:   Line scans obtained across sample (1) for different

values of z measured in λ_{Cu}.

6.3.2. Electron microscope results.

A key problem in any nondestructive imaging is to be sure that the key images are indeed relevant - that, in this case, the images can be interpreted as indicative of the local strength of the bond. We have been able to demonstrate this by a subsequent destructive technique - pulling the bond apart, followed by SEM inspection. Figures 6.9 (a) and 6.9 (b) illustrate two SEM micrographs taken from the two sides of the sample once pulled apart.

The comparison between these micrographs and Figure 6.4 (b) is encouraging. The central non-uniform regions correspond to the strong macroscopic deformations that had taken place in the bonding process - this could be observed with the naked eye.

6.3.3. Results obtained with an X-ray microprobe.

It was seen that the dark regions on the acoustic micrographs corresponded to areas of good bonding. Therefore, one would have expected more diffusion to have occurred in the dark regions. Further, it is known that, when diffusion bonding two dissimilar metals, the species with small atoms find it easier to diffuse into the lattice of the other material, (Tylecote, 1967). This was checked with an X-ray microprobe for sample (1). The local concentration of copper in the WCCo surface was measured. The result of this analysis is presented in Figure 6.10.

(a)

(b)

Figure 6.9:   Two SEM micrographs obtained from sample (1),
               once the bond was pulled apart. (a) = the WCCo
               side and (b) = the Cu side.

142.
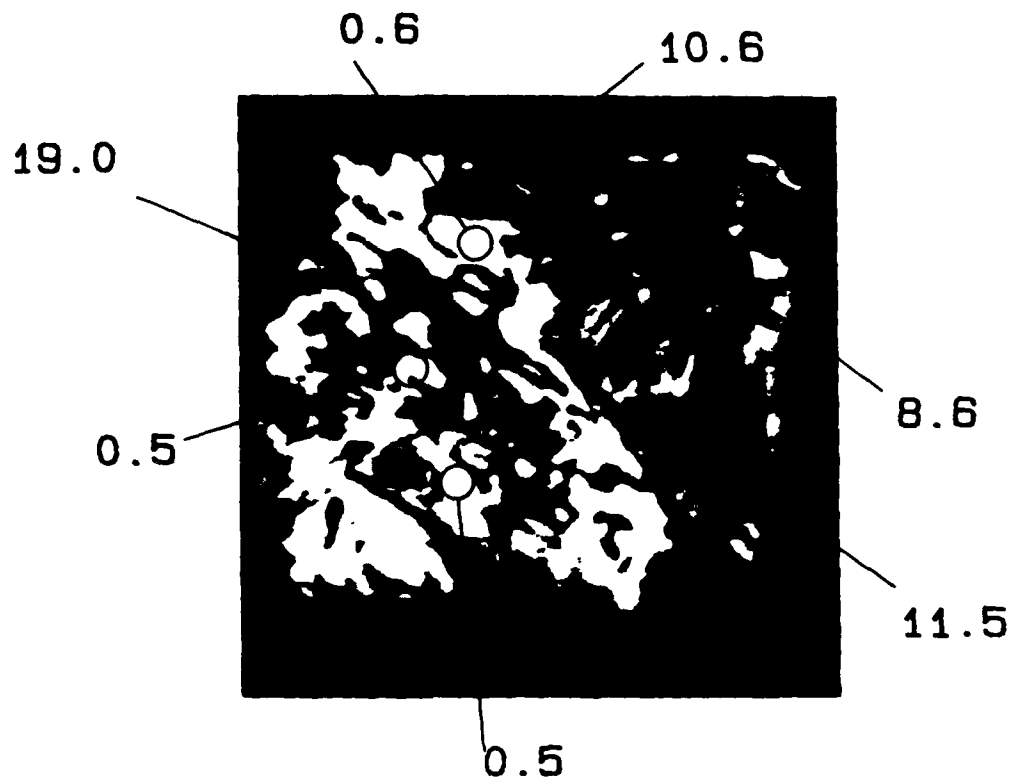
Figure 6.10:   The X-ray microprobe results obtained from sample (1).
                The numbers show the measured percentage of copper
                concentration in the WCCo side on different points of
                the acoustic micrograph.

Owing to technological difficulties (mainly the limited scan size

available on the microprobe system, i.e. 200μm x 200μm), a "micro-

graph" could not be obtained whereby the contrast would represent the

Cu concentration on the entire surface. The surface was, therefore,

probed at some chosen points; the area of circles represents the

uncertainty in the position of the points probed. It is seen that,

by primary considerations, the concentration of the copper is

substantially higher in the dark regions - indicating more diffusion and better bonding in these regions. Thus, the conclusion that dark areas correspond to the areas of good bonding is substantiated by this result.

6.4.   Discussion and conclusions.

It has been shown that acoustic microscopy - the pulse compression technique in particular - is directly applicable to the NDE of metallic diffusion bonds. We have demonstrated that time gated reflection imaging of metal:metal diffusion bonds is possible. Three examples were presented and, in each case, the nonuniformities in the structure of the bonds were clearly revealed.

To the first order, any nonuniformity in the bond can serve as a measure of bond integrity. One could, for example, define a "figure of merit" for a bond, by comparing the average value of contrast, over the bond area, with some kind of standard. Having measured the "figure of merit", one could then define a "threshold", above which the bond would be acceptable. Although this would probably provide a fast technique for assessing the quality of the bond, with possible industrial applications, it would not exploit the *full* potential of the microscope - the ability to characterise with high resolution.

We have studied the nature of the contrast on a microscopic basis. The V(z) results obtained clearly indicate that, for the samples tested, no contrast reversal was present. It suggests, therefore, that the amplitude of the received signal is a good measure of the acoustic reflectivity at the bond. Since, in general, the reflection coefficient at a good bond is low, it is concluded that dark patches on the acoustic micrographs correspond to areas of good bonding. For one of the samples, we have confirmed this conclusion by destructive separation of the bond and SEM inspection. For the same sample, the results obtained from the X-ray microprobe clearly demonstrate that the dark areas on the micrograph correspond to regions where more diffusion has taken place.

The results presented in this Chapter suggest that pulse compression reflection acoustic microscopy provides a unique and nondestructive means of viewing and characterising metallic diffusion bonds, with high lateral resolution.

CHAPTER 7

CONCLUSIONS AND SUGGESTIONS FOR FURTHER INVESTIGATION

7.1.   Conclusions

(i)   A new formulation for diffraction and focussing in lossy

        media has been developed. The nature of elementary waves

        has been studied and the resolution performance under

        high losses investigated.

(ii)   The major instrumental design aspects for a reflection

        1 GHz instrument have been outlined. A reflection

        microscope has been constructed and surface micrographs

        obtained from a wide range of samples.

(iii)   A design procedure for reduced aperture lenses has been

        developed. It was shown that, with a single reduced

        aperture lens, the interior of a wide range of objects

        can be examined. Time gated imaging of subsurface planes

        was demonstrated and a number of subsurface micrographs

        presented – including transistor:header bonds.

(iv)   Pulse compression acoustic microscopy at 60 MHz was
         demonstrated. The performance of such a system in the
         context of subsurface imaging was explored and it was
         shown that major advantages can be gained with this
         system.

(v)   A theoretical model for the pulse compression microscope
         has been developed and the behaviour of such a system
         in the presence of frequency dependent losses was
         investigated.

(vi)   Micrographs from metal:metal diffusion bonds have been
         obtained with the pulse compression microscope and the
         NDE of diffusion bonds demonstrated. Preliminary studies
         for the contrast as a measure of bond integrity have
         been pursued.

7.2.   Suggestions for Further Investigation.

Towards the end of any research programme, a number of truths are
revealed and also, as a byproduct, a number of new questions arise.
The major conclusions were presented in the last section but there
remain a number of questions which would merit further investigation.
These questions would probably provide some guidelines for the
continuation of the work presented in this thesis.

(i)   Theory of focussing in a lossy medium to be extended to

        three dimensions for circularly symmetric systems, by

        means of Hankel transforming the cylindrical wave equation.

(ii)   A multilayer reflectance function computer programme to

        be developed and the nature of the fringes, in the context

        of layered media, to be studied.

(iii)   A number of micrographs from different transistor packages

        have to be obtained. The transistors to be electrically

        tested and a correlation between the acoustic contrast and

        the performance of the device would probably prove

        fruitful.

(iv)   Pulse compression techniques have to be extended to higher

        frequencies and the class of objects for which the

        technique might prove advantageous to be identified.

        Doped semiconductors, integrated optical films and opti-

        cal fibres can be potential candidates.

(v)   The point spread function and the contrast formation for

        a chirped pulse microscope to be studied. Also, the

        effective frequency of operation, in the presence of

        frequency dependent attenuations needs further consider-

        ation.

(vi)   Further investigation into the contrast of diffusion bond micrographs would require a mathematical model for the metal:metal interface and more quantitative measurements.

REFERENCES

Addison, R.C., (1982), Rockwell International Science Center, private communication.

Alais, P., and Hennion, P.Y., (1979), "Étude par une Method de Fourier de l'Interaction Non lineaire de Deux Rayonnements Acoustiques dans un Fluide Absorbant. Cas Particulier de l'emission Parametrique", Acoustica 43 (1).

Alais, P., Hennion, P.Y., and Lagreve, M., (1979), "Theorie Fourier de la Propagation Lineaire et Non-lineaire dans un Fluide Absorbant, Application à la Transduction Parametique", Journal de Physique, 40 (1).

Ash, E.A., (1978), "Fundamentals of Signal Processing Devices", in "Acoustic Surface Waves", (ed. A.A. Oliner), Vol. 24, pp. 97-185, Springer-Verlag, New York.

Ash, E.A., (1980), "Scanned Image Microscopy", Academic Press, London.

Atalar, A., (1978), "An Angular Spectrum Approach to Contrast in Reflection Acoustic Microscopy", J. Appl. Phys., 49 (10), pp. 5130-5139.

Atalar, A., (1979), "A Physical Model for Acoustic Signatures", J.Appl. Phys., 50 (12), pp. 8237-8239.

Atalar, A., Quate, C.F., and Wickramasinghe, H.K., (1977), "Phase Imaging in Reflection with the Acoustic Microscope", Appl. Phys. Lett., 31 (12), pp. 791-793.

Attal, J., (1979), "The Acoustic Microscope - a Tool for Non-destructive Testing", in "Non-destructive Evaluation of Semiconductor Materials and Devices", (Ed. J.N. Zemel), pp. 631-676, Plenum, New York.

Attal, J., (1980), "Acoustic Microscopy: Imaging Microelectronic Circuits with Liquid Metals", in "Scanned Image Microscopy", (Ed. E.A. Ash), pp. 100-118, Academic Press, London.

Attal, J., (1981), Université des Sciences et Technique du Languedoc, Montpellier, private communication.

Attal, J., and Quate, C.F., (1976), "Investigations of Some Low Absorption Liquids", J. Acoust. Soc. Am., 59 (1), pp. 69-73.

Auld, B.A., (1973), "Acoustic Fields and Waves in Solids", Vol. 1., Wiley-Interscience, New York.

Bartle, P.M., (1975), "Diffusion Bonding - a Look at the Future", Welding Journal, November 1975, pp. 799-804.

Bennett, S.D., (1982), "IC Applications for Acoustic Microscopy",
Proc. of the Int. Conf. on the Quality of Electronic Devices:
Strategy for Next Years, Bordeaux, France.

Bennett, S.D., and Ash, E.A., (1981), "Differential Imaging with
the Acoustic Microscope", IEEE Trans. SU 28 (2), pp. 59-62.

Bennett, S.D., Sinclair, D.A., and Smith, I.R., (1982), "Measurement
of Elastic Properties of Tissue using Scanning Acoustic Microscopy",
Submitted to Physics in Medicine and Biology, December 1982.

Bray, R.C., Galhoun, J., Koch, R., and Quate C.F., (1980), "Film
Adhesion Studies with the Acoustic Microscope", Vol. 74, pp. 295-302.

Briggs, G.A.D., Ilett, C., and Somekh, M.G., (1982), "Acoustic
Microscopy for Material Studies", in "Acoustic Imaging", Vol. 12,
(ed. E.A.Ash and C.R. Hill), pp. 89-99, Plenum, New York.

Burton, N.J., and Pino, F., (1982), "Digital Image Storage and
Processing for Scanning Microscopy", to be published.

Champion, J.A., (1982), National Physical Laboratory, private
communication.

Cook, C.E., (1960), "Pulse Compression - Key to More Efficient Radar
Transmission", Proc. IRE., Vol. 48, pp. 310-315.

Desilets, C.S., Fraser, J.D., and Kino, G.S., (1978), "The Design of Efficient Broadband Piezoelectric Transducers", IEEE Trans., SU 25 (3), pp. 115-125.

Faridian, F., (1982), University College London, private communication.

Gee, M.G., (1982), National Physical Laboratory, private communication.

Gerard, H.M., (1977), "Surface Wave Interdigital Electrode Chirp Filters" in "Surface Wave Filters", (ed. H. Matthews), John Wiley, New York.

Hipwood, B., (1982), Texas Instruments Limited, Bedford, England, private communication.

Hollis, R.L., and Hammer, R., (1980), "Defect Detection for Microelectronics by Acoustic Microscopy", in "Scanned Image Microscopy", (ed. E.A. Ash), pp. 155-164, Academic Press, London.

Islam, M., Nikoonahad, M. and Ash, E.A., "Large Aperture Lens Focussing of Acoustic Waves in Highly Absorptive Media, using Fresnel Kirchoff Approach", to be published.

Jipson, V.B., (1979a), "Acoustic Microscopy at Optical Wavelengths", Ph.D. Thesis, Stanford University, Stanford, California.

Jipson, V.B., (1979b), "Acoustic Microscopy of Interior Planes",
App. Phys. Lttrs., 35 (5), pp. 385-387.

Jipson, V.B., and Quate, C.F., (1978), "Acoustic Microscopy at
Optical Wavelengths", App. Phys. Lttrs., 32 (12), pp. 789-791.

Johnson, N., (1982), University College London, private communication.

Kessler, L.W., and Yuhas, D.E., (1978), "Structural Perspective",
Industrial Research, January 1978, pp. 52-56.

Kinsler, L.E., and Frey, A.R., (1962), "Fundamentals of Acoustics",
John Wiley and Sons Inc., New York.

Klauder, J.R., Price, A.C., Darlington, S., and Albersheim, W.J.,
(1960), "Theory and Design of Chirp Radars", Bell Systems Tech.
Jour., Vol, 39, pp. 745-808.

Kushibiki, J., Maehara, H. and Chubachi, N., (1981), "Acoustic
Properties of Evaporated Chalcogenide Glass Films", Elect. Lttrs.,
17 (9), pp. 322-323.

Kushibiki, J., Ohkubo, A., and Chubachi, N., (1981a), "Linearly
Focussed Acoustic Beams for Acosutic Microscopy", Elect. Lttrs.,
17 (15), pp. 520-522.

Kushibiki, J., Ohkubo, A., and Chubachi, N., (1981b)., "Acoustic Anisotropy Detection of Materials by Acoustic Microscopy using Line-Focus Beam", Proc. of IEEE Ultrasonics Symposium, pp. 552-556.

Kupperman, D.S., Pahis, L., Yuhas, D.E., and McGraw, T.E., (1980), "Acoustic Microscopy Techniques for Structural Ceramics", Am. Ceramic Soc. Bulletin, 59 (8), pp. 814-816, pp. 839-840.

Lemons, R.A., and Quate, C.F., (1974a), "Acoustic Microscope - Scanning Version", Appl. Phys. Lttrs., 24 (4), pp. 163-165.

Lemons, R.A. and Quate C.F., (1974b), "Integrated Circuits as Viewed with the Acoustic Microscope", Appl. Phys. Lttrs., 25 (5), pp. 251-253.

Madeyski, A., and Kessler, L., (1976), "Initial Experiments in the Application of Acoustic Microscopy to the Characterisation of Steel and to the Study of Fracture Phenomena", IEEE Trans. SU 23 (5), pp. 363-369.

Miller, A.J., (1982), "Applications of Acoustic Microscopy in the Semiconductor Industry", in "Acoustical Imaging", Vol. 12., (ed. E.A. Ash and C.R. Hill), pp. 67-87, Plenum, New York.

Nikoonahad, M., (1983), "Reflection Acoustic Microscopy for Industrial NDE", in "Research Techniques for Nondestructive Testing", (ed. R.S. Sharpe), Vol. 7, to appear.

Nikoonahad, M., and Ash, E.A., (1982), "Ultrasonic Focussing in Absorptive Fluids", in "Acoustical Imaging", Vol. 12, (ed. E.A. Ash and C.R. Hill), pp. 47-60, Plenum, New York.

Nikoonahad, M., Yue, G.Q., and Ash, E.A., (1982), "Subsurface Broadband Acoustic Microscopy of Solids using Reduced Aperture Lenses", Proc. of DARPA/AFML Review of Progress in Quantitative NDE, La Jolla, California, U.S.A.

Parmon, W., and Bertoni, H.L., (1979), "Ray Interpretation of the Material Signature in the Acoustic Microscope", Elect. Lttrs., 15 (21), pp. 684-686.

Pino, F., Sinclair D.A., and Ash, E.A., (1981), "Scanning Acoustic Microscopy of Solid Objects using Aspheric Lenses", Proc. of 11th Int. Conference on Acoustical Imaging, Monterey.

Ouate, C.F., (1980), "Microwaves, Acoustics and Scanning Microscopy", in "Scanned Image Microscopy", (ed. E.A. Ash), pp. 23-55, Academic Press, London.

Reeder, T.M., and Winslow, D.K., (1969), "Characteristics of Micro-wave Acoustic Transducers for Volume Wave Excitation", IEEE Trans., MTT 17 (11), pp. 927-941.

Rosencwaig, A., (1980), "Thermal-wave Imaging and Microscopy", _in_ "Scanned Image Microscopy", (ed. E.A. Ash), Academic Press, London.

Rugar, D., (1981), "Cryogenic Acoustic Microscopy", Ph.D. Thesis, Stanford University, Stanford, California, U.S.A.

Sinclair, D.A., and Ash, E.A., (1980), "Bond Integrity Evaluation using Transmission Scanning Acoustic Microscopy", Elect. Lttrs., 16 (23), pp. 880-882.

Sinclair, D.A., and Smith, I.R., (1982), "Tissue Characterisation using Scanning Acoustic Microscopy", _in_ "Acoustical Imaging", Vol. 12, (ed. E.A. Ash and C.R. Hill), pp. 505-516, Plenum, New York.

Smith, I.R., and Wickramasinghe, H.K., (1982), "SAW Attenuation Measurement in the Acoustic Microscope", Elect. Lttrs., 18 (22), pp. 955-956.

Smith, I.R., Sinclair, D.A., and Wickramasinghe, H.K., (1980), "Acoustic Microscopy of Elastic Constants", Proc. of IEEE Ultra-sonics Symposium, pp. 667-682.

Smith, I.R., Sinclair, D.A., and Wickramasinghe, H.K., (1981),
"Acoustic Microscopy of Slowness Surfaces", Proc. of IEEE
Ultrasonics Symposium, pp. 591-596.

Tsai, C.S., Lee, C.C., and Wang, J.K., (1979), "Diagnosis of Hybrid
Microelectronics using Transmission Acoustic Microscopy", Proc.
of Int. Reliability Physics, IEEE CH1425-8PHY, pp. 178-182.

Tsai, C.S., Wang, S.K., and Lee C.C., (1977), "Visualisation of
Solid Material Joints using a Transmission Type Scanning Acoustic
Microscope", Appl. Phys. Lttrs., 31 (9), pp. 317-320.

Tittmann, B.R., and Ahlberg, L.A., (1982), "Attenuation and
Grain Noise Parameters", Proc. of DARPA/AFML Review of Progress in
Quantitative NDE, La Jolla, California, U.S.A.

Tylecote, R.F., (1967), "Diffusion Bonding", Welding and Metal
Fabrication, December 1967, pp. 483-489.

Weglein, R.D., (1976), "Acoustic Properties of Sputtered Glass at
Microwave Frequencies", Appl. Phys. Lttrs., 29 (5), pp. 277-279.

Weglein, R.D., (1980a), "Metrology and Imaging in the Acoustic
Microscope", in "Scanned Image Microscopy", (ed. E.A. Ash), pp. 127-
136, Academic Press, London.

Weglein, R.D., (1980b), "Acoustic Microscopy of SAW Dispersion and Film Thickness Measurement", IEEE Trans. SU 27 (2), pp. 82-86.

Weglein, R.D., (1982a), "Rayleigh Wave Absorption via Acoustic Microscopy", Elect. Lttrs., 18 (1), pp. 20-21.

Weglein, R.D., (1982b), "Nondestructive Film Thickness Measurement on Industrial Diamonds", Elect. Lttrs., 18 (23), pp. 1003-1004.

Weglein, R.D., and Wilson, R.G., (1978), "Characteristic Material Signatures by Acoustic Microscopy", Elect. Lttrs., 14 (12), pp. 352-353.

Wickramasinghe, H.K., (1976), Mechanical Design at Stanford University, Stanford, California, unpublished.

Wickramasinghe, H.K., (1978), "Contrast in Reflection Acoustic Microscopy", Elect. Lttrs., 14 (10), pp. 305-306.

Wickramasinghe, H.K., (1979), "Contrast and Imaging in the Scanning Acoustic Microscope", Jour. App. Phys., 50 (2), pp. 664-672.

Wilson, R.G., and Tucker, P.A., (1979), "Acoustic Microscopy of Polymer Materials", Appl. Phys. Lttrs., 35 (10), pp. 755-756.

Wilson, R.G., Weglein, R.D., and Bonnell, D.M., (1977), "Scanning
Acoustic Microscopy for Integrated Circuit Diagnostics", in
"Semiconductor Silicon", Proc. of Electrochemical Society, (ed.
H.R. Huff and E. Sirtl), Vol. 77 (2), Princeton, U.S.A.

Yamanaka, K., (1982), "Analysis of SAW Attenuation Measurement using
Acoustic Microscopy", Elect. Lttrs., 18 (14), pp. 587-589.

Yue, G.Q., Nikoonahad, M., and Ash, E.A., (1982a), "Pulse Compression
Subsurface Acoustic Microscopy", Elect. Lttrs., 18 (18), pp. 767-769.

Yue, G.Q., Nikoonahad, M., and Ash, E.A., (1982b), "Subsurface
Acoustic Microscopy using Pulse Compression Techniques", Proc. of
IEEE Ultrasonics Symposium, San Diego, U.S.A.

DATE
ILMED
8